

**Rock Glacier Kinematics: A Proxy for Assessing
Periglacial Dynamics and Ground Ice Content on the
Tibetan Plateau**

HU, Yan

A Thesis Submitted in Partial Fulfillment
of the Requirements for the Degree of
Doctor of Philosophy
in
Earth and Atmospheric Sciences

The Chinese University of Hong Kong
August 2021

Thesis Assessment Committee

Professor CHAN Man Nin (Chair)

Professor LIU Lin (Thesis Supervisor)

Professor YANG Hongfeng (Committee Member)

Professor DELALOYE Reynald (External Examiner)

Abstract of thesis entitled:

Rock Glacier Kinematics: A Proxy for Assessing Periglacial Dynamics and Ground Ice Content on the Tibetan Plateau

Submitted by HU, Yan
for the degree of Doctor of Philosophy
at The Chinese University of Hong Kong in (August 2021)

Rock glaciers are ice-debris landforms widely distributed in the mountainous periglacial realm worldwide. They serve as important indicators for permafrost which is defined by its underground temperature and invisible in most other cases, especially for regions such as the Tibetan Plateau where in-situ observations are limited in spatial coverage due to the harsh and remote environment. Surface kinematics of rock glaciers, which manifests the characteristic permafrost creep process occurring at depth, has become an accessible and quantifiable feature with the application of remote sensing methods.

In a case study focusing on a puzzling periglacial landform near the Kunlun Pass, we addressed a long-standing issue concerning its geomorphological classification from a kinematic perspective. We employed the Interferometric Synthetic Aperture Radar (InSAR) technique to quantify the temporal and spatial variations of the downslope creeping velocities. By critically analyzing the influences that the mechanical processes imposed on the landform and piecing our observations together, we identified the landform as a debris-mantled-slope-connected rock glacier, with gelifluction processes occurring on the surface as small-scale and discrete events.

To fill in the knowledge gap about rock glaciers on the plateau, we compiled a rock glacier inventory over the West Kunlun Mountains of China by manually interpreting the Google Earth imagery and the displacement maps generated by InSAR. This kinematic approach can only produce conservative mapping results due to the limitations of InSAR measurements. Therefore, we adopted semantic image segmentation powered by a deep learning model, i.e., DeepLabv3+, to infer rock glaciers that had been missed in the manual delineation. Finally, within the 124,000 km² study area, we identified 413 rock glaciers: 290 of them were outlined by manual detection and 123 of them were mapped by deep learning. Their mean and maximum downslope velocities are 24 cm yr⁻¹ and 127 cm yr⁻¹, respectively.

We investigated the potential water storage of the rock glaciers situated in Khumbu Valley, Nepal, by developing a velocity-constrained model to infer their ice contents. We adopted a rheological model based on adaptations of Glen's flow law and assumed a homogeneous two-layer structure for rock glaciers that consists of an ice-free active layer and an ice-rich

permafrost core. The velocity constraints applied to the model were derived from InSAR measurements. The inferred ice fraction of the rock glaciers in Khumbu Valley ranges from 71.0% to 75.3%. Extrapolating from our findings in Khumbu Valley, the total amount of water stored in rock glaciers could be \sim 10 billion m³ over the Nepalese Himalayas.

In summary, this thesis advanced the understanding of surface dynamics and classification of periglacial landforms from the perspectives of geomorphology and kinematics. We produced a rock glacier inventory using remote sensing and deep learning in a mountain range where previous investigations are scarce. We presented results of estimating rock glacier ice contents from a rheological model and surface velocity measurements. Products from this thesis and extended work will improve the knowledge of rock glaciers and the permafrost environment in the Tibetan Plateau where climatic conditions are various and fast changing.

摘要

石冰川是廣泛分佈於全球山地冰緣範圍內的冰-岩混合地貌。它們是多年凍土的重要指標：多年凍土由地下溫度定義，在大多數情況下是不可見的；特別是對於青藏高原等地區，由於環境惡劣和偏遠，現場觀測的空間覆蓋範圍有限。隨著遙感方法的應用，石冰川的表面運動學特徵表現出發生在深處的多年凍土蠕變過程，並已成為可獲取和可量化的研究變量。

在一個關注崑崙山埡口附近的冰緣地貌的案例研究中，我們從運動學的角度解決了一個長期存在的關於其地貌分類的問題。我們採用干涉合成孔徑雷達 (InSAR) 技術來量化沿坡向運動速度的時間和空間變化。通過綜合分析形變過程對地貌的影響並與我們的觀察結果相結合，我們將該地貌判定為岩屑-披覆-斜坡連接的石冰川，地表上發生的融凍泥流過程是小規模的離散事件。

為了填補青藏高原地區石冰川的知識空缺，本文通過人工解譯谷歌地球圖像和 InSAR 生成的位移圖，繪製了中國西崑崙山石冰川編目。由於 InSAR 測量的局限性，這種運動學方法只能產生保守的製圖結果。因此，我們採用了由深度學習模型（即 DeepLabv3+）驅動的語義圖像分割來推斷人工描繪中遺漏的石冰川。最終，在 124,000 平方公里的研究區域內，我們識別了 413 條石冰川：其中 290 條通過人工檢測勾勒出輪廓，123 條通過深度學習自動繪製。它們的平均和最大沿坡向運動速度分別為 24 cm yr^{-1} 和 127 cm yr^{-1} 。

我們開發了通過速度約束的流變模型來推斷石冰川含冰量，並進一步研究了位於尼泊爾昆布山谷的石冰川潛在蓄水量。我們採用了基於格倫流動定律改編的流變模型，並假設岩石冰川具有均勻的雙層結構，由無冰活動層和富含冰的多年凍土核心組成。我們採用 InSAR 測量的石冰川表面速度作為模型約束。模型推斷昆布山谷石冰川的含冰量範圍為 71.0% 至 75.3%。根據我們在昆布山谷的發現進行推斷，尼泊爾喜馬拉雅山脈石冰川中儲存的總水量可能約為 100 億立方米。

綜上所述，本文從地貌學和地表動力學的角度促進了對冰緣地貌的地表過程和分類的理解。我們使用遙感和深度學習在先前對石冰川的調查很少的山脈中製作了石冰川編目。我們展示了從流變模型和表面速度測量值估算石冰川含冰量的結果。青藏高原氣候條件多樣且變化迅速，本論文和擴展工作的成果將增進對青藏高原的石冰川和多年凍土環境的理解。

Acknowledgements

This thesis is the fruit of four years of laboratory work, considerable efforts in the field on the Tibetan Plateau, countless hours of reading, and many insightful discussions at our department and at the University of Exeter. In numerous ways, I've benefited greatly from the Ph.D. training and dissertation writing, as well as plentiful help and guidance from many kind and brilliant people to whom I am enormously grateful:

My supervisor, Prof. Lin Liu, in the first place for re-initiating research on rock glaciers in western China, a topic that had been ignored for decades, and for taking me to work on this exciting project when I had disadvantaged background in the relevant fields at the beginning. Your trust, patience, and generosity have made all the difference. You have granted me all the resources and opportunities for me to explore and develop my Ph.D. research at every stage. You've also been full of curiosity, encouragement, and modesty, by which I am deeply inspired. Many constructive feedbacks from you have made this thesis better. I am so fortunate and grateful being a member of our group.

Prof. Stephan Harrison, my host supervisor at the University of Exeter, who kindly supported me for a new collaborative project during the difficult time of the pandemic outbreak, has broaden my research horizon. I've found inspiration from your way of thinking as an excellent geomorphologist. I am also grateful to the Hong Kong RGC and CUHK Global Scholarship Programme for sponsoring my visit at Exeter.

I am grateful to the committee members of my dissertation: Prof. Reynald Delaloye chairs the IPA Rock Glacier Action Group, from where I get to know many intelligent and energetic colleagues sharing research interests in rock glaciers. Much of my thesis research is fueled by the lively discussions and insightful field excursions held by the Action Group Workshops. Prof. Man Nin Chan has been full of good cheer and generously offering help and sharing his approach to science and teaching to students. Prof. Hongfeng Yang has brought his keen intellect and sound judgement to my research since my qualifying examination and made my thesis more comprehensive than it otherwise would be. I am thankful to all the invaluable guidance throughout, and the time dedicated to reviewing this dissertation and serving as examiners in my oral defense.

I am well aware of and deeply humbled by the substantial assistance offered by many collaborators during our fieldwork on the plateau. My gratitude begins with Prof. Lin Zhao, who actively supported our project from the beginning and offered expertise guidance to our work. Prof. Tonghua Wu has been providing logistic support to us in the field whenever needed.

Dr. Xiaofan Zhu was the true team leader ably steering us through the challenges of all sorts during our field work at Kunlun Pass, whose efforts and contributions were remarkable. Prof. Xiaowen Wang has been the steadfast partner working at the front by my side, I could always trust you. Thanks as well to Jialun Cai, Junming Hao, Huayun Zhou, and Yongping Qiao, all of whom offered considerable help.

Great thanks to my group mates: Zhuoxuan Xia, Ho Ming Tsang, Xingyu Xu, Jiahua Zhang, Enze Zhang, Xiyu Chen, and Lingcao Huang. So much I have learnt from every one of you. Also, I owe a special debt of gratitude to Lingcao, who has been always willing to share your original perspectives and knowledge with me, my research was backed up by your extraordinary talents. More importantly, thanks for your friendship. Thanks as well to all the EASC members and teaching staffs for all the support and help. Special thanks to Miss Rui Zhao, my roommate, for selflessly helping me at my difficult times, and for all the joyful memories we shared.

Finally, among those who are most pleased to see the completion of this thesis, are my lifelong friends and loving family – they are very unlikely to be interested in rock glaciers – but because it is almost time for us to reunite. Thank you for supporting me throughout my journey. I am forever indebted to your unconditional love that makes everything sweeter and brighter.

Table of Contents

Abstract	i
摘要	iii
Acknowledgements	iv
Chapter 1 Introduction	1
1.1 Motivation, challenges, and objectives	1
1.2 Research questions and roadmap of thesis	4
Chapter 2 A review on rock glacier kinematics	6
2.1 Monitoring techniques	6
2.1.1 Methods for detecting surface kinematics	7
2.1.2 Methods for detecting internal kinematics	8
2.2 Kinematic characteristics	8
2.2.1 Magnitude and spatial distribution	9
2.2.2 Centennial to millennial variations	9
2.2.3 Decadal variations	10
2.2.4 Seasonal and sub-seasonal variations	11
2.3 Dynamic mechanisms	11
2.3.1 Major controlling variables	12
2.3.2 Principal mathematical formulations	12
2.4 Responses to climatic forcing	14
2.4.1 Centennial to millennial timescales	14
2.4.2 Decadal timescale	15
2.4.3 Interannual timescale	16
2.4.4 Seasonal timescale	16
2.4.5 Destabilization	17
2.5 Research milestones	18
2.6 Summary	19
Chapter 3 Quantification of permafrost creep provides kinematic evidence for classifying a puzzling periglacial landform	21
3.1 Introduction	21
3.2 Rock glaciers versus gelifluction deposits	23

3.3 Study area	25
3.4 Methods	27
3.4.1 Field observations and soil sampling	27
3.4.2 Unmanned aerial vehicle (UAV) survey	28
3.4.3 Surface velocities derived from InSAR	28
3.5 Results	30
3.5.1 Morphological and material features	30
3.5.2 Kinematic characteristics	33
3.6 Discussion	37
3.6.1 Geomorphological approach	37
3.6.2 Kinematic approach	37
3.6.3 Geomorphological classification of the landforms	40
3.7 Conclusions	40
Chapter 4 Inventorying rock glaciers in the arid West Kunlun of China using SAR interferometry and deep learning	42
4.1 Introduction	42
4.2 Study area	44
4.3 Methodology	46
4.3.1 Inventorying active rock glaciers from interferograms and Google Earth images	46
4.3.2 Automated mapping of rock glaciers using deep learning	51
4.4 Results	54
4.4.1 Performance of the automated mapping approach	54
4.4.2 Geomorphic characteristics of the inventoried rock glaciers	56
4.4.3 Surface kinematics of the inventoried active rock glaciers	59
4.5 Discussion	61
4.5.1 Potential and limitations of the InSAR-Deep learning combined method for mapping rock glaciers	61
4.5.2 Genetic and evolutional implications from the geomorphic characteristics of rock glaciers	62
4.6 Conclusions	64
Chapter 5 Modelling rock glacier velocity and ice content, Khumbu and Lhotse Valleys, Nepal	67
5.1 Introduction	67

5.2 Study area	69
5.3 Methods	70
5.3.1 Deriving surface kinematics with InSAR	70
5.3.2 Estimating ice content from a surface-velocity-constrained model	72
5.3.3 Model design and assumptions	72
5.3.3.1 Model calibration	75
5.3.3.2 Model validation	77
5.3.3.3 Sensitivity analysis	79
5.3.3.4 Model application	79
5.4 Results	80
5.4.1 InSAR-derived surface kinematics of rock glaciers	80
5.4.2 Model validation	82
5.4.3 Model sensitivity	86
5.4.4 Modelled ice contents	86
5.5 Discussion	88
5.5.1 Potential water storage in rock glaciers in the Nepalese Himalaya	88
5.5.2 Validity of general assumptions and model design	89
5.5.2.1 Steady-state creep of rock glaciers	89
5.5.2.2 Homogeneous warm permafrost	89
5.5.2.3 Neglect of shear horizon	90
5.5.2.4 Accuracy of rock glacier thickness derivation	91
5.5.2.5 Identification of the coherently moving part of rock glaciers	91
5.5.2.6 Generalization of statistical relationships derived from Las Liebres rock glacier	92
5.5.3 Application of the model and outlook	92
5.6 Conclusions	92
Chapter 6 Conclusion and outlook	94
6.1 Conclusion	94
6.2 Innovative merits and potential impacts	95
6.3 Future research	96
Abbreviations	98
Bibliography	99

Chapter 1 Introduction

“Ignorance is bold, and knowledge reserved.”
—Thucydides

Rock glaciers manifest the creep of alpine permafrost occurring at depth in the past and/or at present. Their presence and dynamics serve as an increasingly important reference to studying permafrost environment with the emergence of remote sensing imagery and data processing techniques. Mapping and investigating dynamics of rock glaciers shed light on the study fields such as periglacial geomorphology, permafrost distribution and changes, and mountain hydrology. This chapter first introduces the motivation, challenges, and objectives of studying permafrost on the Tibetan Plateau from the perspective of rock glacier kinematics, followed by raising key research questions and presenting a roadmap towards addressing these questions in the thesis.

1.1 Motivation, challenges, and objectives

Rock glaciers are debris–ice landforms first identified in Alaska at the beginning of the 20th century and have drawn research interest due to their distinctive morphology and intriguing genesis (Figure 1.1) (Capps, 1910). They are soon found to be widely distributed in many mountain ranges around the globe (e.g., Barsch, 1971; Lliboutry, 1953; Outcalt and Benedict, 1965; Wahrhaftig and Cox, 1959), and later are discovered on other celestial bodies in the solar system, e.g., Mars (Carr, 1987; Carr and Schaber, 1977; Colaprete and Jakosky, 1998; Degenhardt, 2003; Hauber et al., 2011; Mahaney et al., 2007; Mellon et al., 2008; Whalley and Azizi, 2003). Numerous efforts have been put into studying rock glaciers because their presence and activity reveal the existence of ground ice which is essential for identifying permafrost – the frozen ground where temperature is below 0 °C perennially – and for exploring the likely occurrence of extra-terrestrial water.

This thesis is motivated by establishing the rock glacier kinematics as a proxy for addressing scientific questions associated with permafrost on the Tibetan Plateau, which has been undergoing degradation in the current warming climate (Ni et al., 2020; Yang et al., 2019; Yao et al., 2019). Previous observations have revealed that the kinematic variations of rock glaciers are responsive to climatic forcing such as the rising air and ground temperature, and intensified water input from snow-melting and precipitation (Delaloye et al., 2010; Eriksen et al., 2018; Haeberli et al., 2006; Ikeda et al., 2008; Kenner et al., 2019; Roer et al., 2005). Meanwhile the mechanism of rock glacier creep process and its controlling factors such as the landform geometry, composition, and environmental conditions, etc., have been investigated by means of numerical modelling and laboratory experiments (Arenson and Springman, 2005a; Azizi

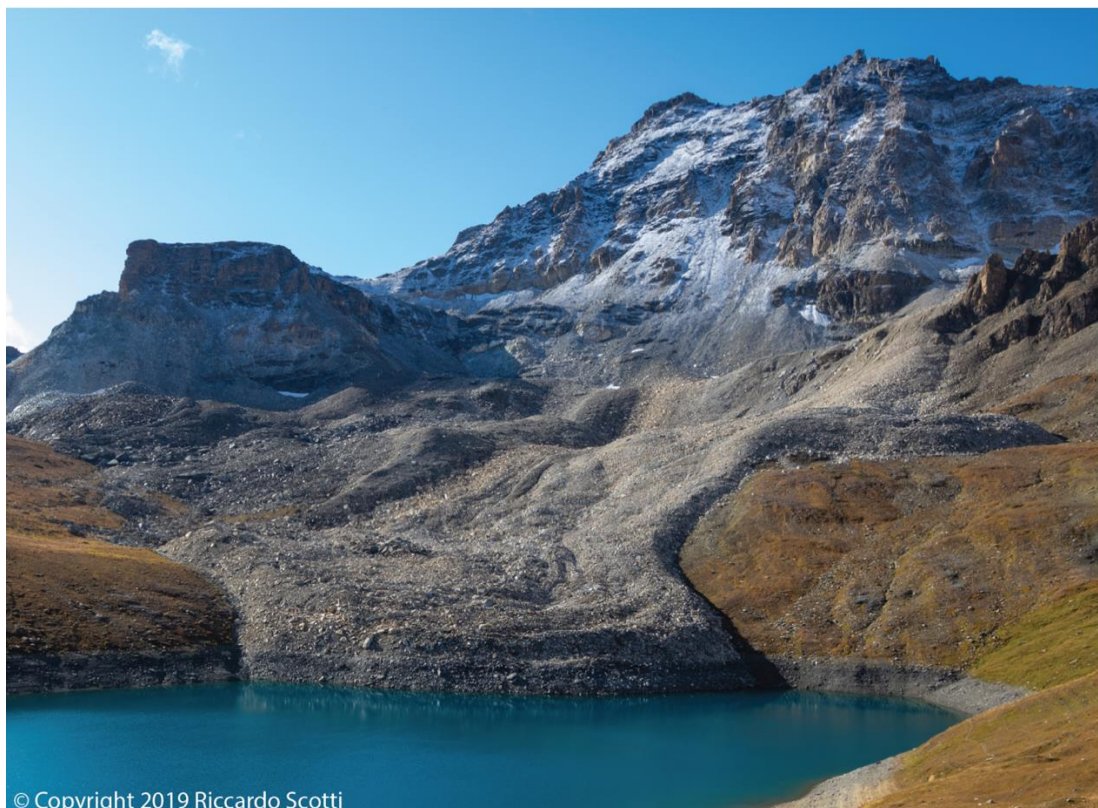
and Whalley, 1996; Cicoira et al., 2019a; Cicoira et al., 2019b; Monnier and Kinnard, 2016; Müller et al., 2016). Based upon the above knowledge accumulated, the International Permafrost Association (IPA) recently proposed rock glacier kinematics as a new Essential Climate Variable (ECV) product for permafrost to the Global Climate Observing System (GCOS) (<https://gcos.wmo.int/en/essential-climate-variables>).

This proposed parameter is especially valuable in monitoring and studying permafrost on the Tibetan Plateau. Climate change on the plateau is more intense than the global average: warming rate of the plateau ($0.031\text{ }^{\circ}\text{C yr}^{-1}$) has been more than twice of the global rate ($0.014\text{ }^{\circ}\text{C yr}^{-1}$) since 1960s (Zhang et al., 2020), whereas the region underlain by permafrost has been warming at an even higher rate ($0.05\text{ }^{\circ}\text{C yr}^{-1}$) since 2004 (Zhao and Sheng, 2019). Consequent permafrost degradation profoundly affects the ecosystem and hydrological system on the plateau as known as the Asian Water Tower (Cheng et al., 2019; Immerzeel et al., 2010; Yang et al., 2019; Yao et al., 2019). However, the meteorological observatories and in-situ measurements of permafrost parameters, such as the ground temperature and active layer thickness, are limited in amount and coverage due to the vast extent and harsh environment of the plateau. Ubiquitous as rock glaciers are in alpine permafrost areas, their kinematics can be quantified utilizing remote sensing methods, which supplements the limited observational data and offers additional reference database for understanding permafrost degradation and its impacts coupled to climate change.

However, challenges are multiple. First, controversial opinions on the basic concepts of rock glaciers, such as their definition and classification, exist in the early research focusing on geomorphology of these landforms on the Tibetan Plateau (Cui, 1985; Harris et al., 1998). Second, since these pioneering studies carried out more than two decades ago (e.g., Li and Yao, 1987; Liu et al., 1995; Zhu, 1989; Zhu et al., 1992), there had been a research gap on rock glaciers on the plateau until recent years when a few inventories of rock glaciers have been published (Baral et al., 2020; Bläthe et al., 2019; Jones et al., 2018b; Jones et al., 2021; Pandey, 2019; Ran and Liu, 2018; Reinosch et al., 2021; Robson et al., 2020; Schmid et al., 2015). Nevertheless, some of these studies focus on relatively small spatial scales (Robson et al., 2020), some delineate rock glaciers from a small portion (5–20%) of randomly sampled subregions (Jones et al., 2018b; Jones et al., 2021; Schmid et al., 2015). Moreover, most of these inventories present no quantitative kinematic data except for Reinosch et al. (2021). Therefore, knowledge of rock glaciers on the plateau, including their distribution and kinematics, are still largely lacking (Figure 1.2). Third, rock glacier kinematics, as a proposed ECV that can be measured remotely and continuously, has the potential to depict properties and changes of the underlying permafrost quantitatively over large spatial scales, which requires further research devoted (Cicoira et al., 2020).

This thesis aims to navigate through the above challenges and therefore promote the implementation of rock glacier kinematics as a proxy for understanding permafrost on the Tibetan Plateau. Specifically, objectives of the thesis are:

- (1) To address the long-standing issue regarding basic concepts of rock glaciers on the plateau
- (2) To inventory rock glaciers and provide essential attributes such as landform location, geometry, and surface kinematics
- (3) To develop new methods for inferring permafrost properties quantitatively from remotely sensed data of rock glaciers



© Copyright 2019 Riccardo Scotti

Figure 1.1 Field photo of Lona rock glacier situated in Evolène, Swiss Alps. The landform is in lobate shape. Surface furrow and ridge features resulting from creep process are discernable from the photo.

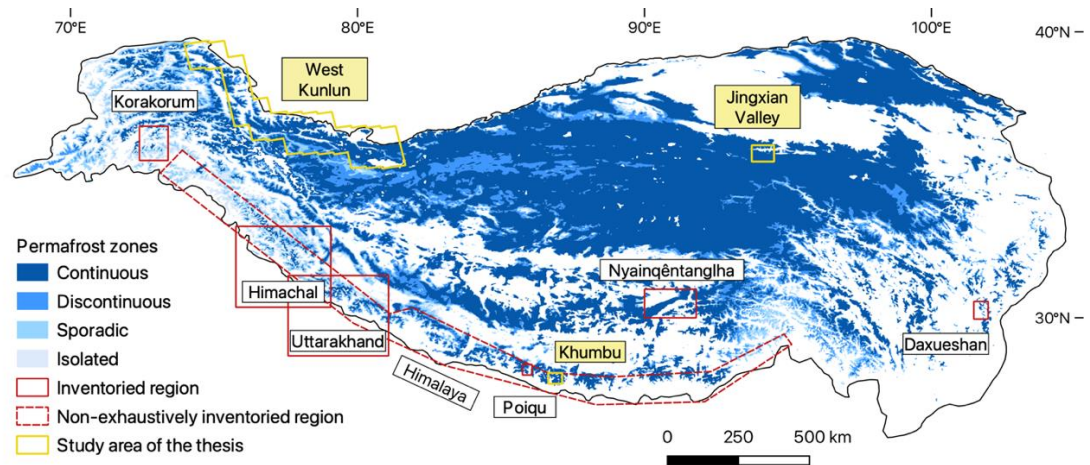


Figure 1.2 Permafrost distribution (Obu et al., 2019) and the locations of published rock glacier inventories on the Tibetan Plateau. Solid red boxes illustrate the regions where exhaustive inventories of rock glaciers have been compiled (Baral et al., 2020; Blöthe et al., 2019; Pandey, 2019; Ran and Liu, 2018; Reinosch et al., 2021; Robson et al., 2020). The dash red polygon outlines the Himalaya region where rock glaciers have been mapped from randomly selected image patches (Jones et al., 2021). The study areas investigated by this thesis are marked in yellow polygons and labelled with yellow background.

1.2 Research questions and roadmap of thesis

This thesis seeks to achieve the primary objectives by addressing three research questions, all of which originate from rock glacier study on the Tibetan Plateau but also have wider relevance to the rock glacier and permafrost research communities. Various methods have been employed to approach these questions as summarized in Table 1.1. Figure 1.3 illustrates the roadmap towards answering the questions in the thesis.

Research Question I: What type of landform is a puzzling periglacial lobe at the Kunlun Pass?

A periglacial landform displaying unique morphologic features was discovered and identified as the Kunlun-type rock glacier in the 1980s (Cui, 1985), and later classified into the gelifluction lobe (Harris et al., 1998). We test this hypothesis by investigating the dynamic processes and providing kinematic evidence for geomorphologic classification.

Research Question II: What is the distribution and kinematic status of rock glaciers in West Kunlun Mountains?

Knowledge of rock glaciers is completely lacking in the West Kunlun, one of the driest mountain ranges in Asia, where widespread permafrost is rapidly warming (Cheng et al., 2019; Li, 1986). We develop an automated approach for compiling regional-scale rock glacier inventory by combining remote sensing and deep learning methods.

Research Question III: How much ground ice is stored in rock glaciers?

Rock glaciers contain significant amount of ground ice and serve as important freshwater resources as mountain glaciers melt in response to climate warming (Jones et al., 2018a; Jones et al., 2019b). We present the first modelling method to infer the ice content of rock glaciers quantitatively from remotely sensed input data including surface kinematics and landform geometry.

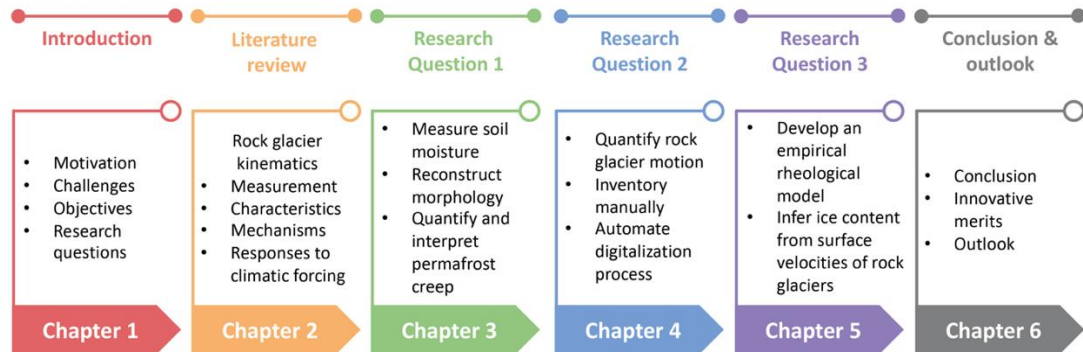


Figure 1.3 Roadmap towards answering the research questions raised in the thesis.

Table 1.1 Research methods employed in the thesis for addressing the three scientific questions.

	Research Question 1	Research Question 2	Research Question 3
Research methods	Soil moisture analysis	InSAR	InSAR
	SfM-MVS photogrammetry	Deep learning	Rheological modelling
	InSAR		

InSAR: Interferometric Synthetic Aperture Radar.

SfM-MVS photogrammetry: Structure from Motion-Multiview Stereo photogrammetry.

Chapter 2 A review on rock glacier kinematics

“If I have seen further, it is by standing on the shoulders of giants.”
—Isaac Newton

This chapter reviews the knowledge on rock glacier kinematics to address the following four questions: (1) How to measure rock glacier kinematics? (2) What are the kinematic characteristics? (3) What are the dynamic mechanisms controlling the movement? (4) How do rock glacier kinematics respond to climatic factors? We summarize the current understanding in the four aspects and conclude the review with a chronicle of milestones in the research field.

2.1 Monitoring techniques

It was in the year of 1900 when “a peculiar form of talus” situated in the San Juan Mountains of Colorado was first reported in the scientific literature (Spencer, 1900). Ten years later, it was known as the rock glacier – a term coined by Capps (1910) to name the landforms of the same type discovered in Alaska. In addition to the detailed depiction of rock glacier morphological characteristics, Capps (1910) deduced solely based on geomorphological evidence that “the forward movement has been continuous and uniform” and “in some such as a glacier”. This hypothesis was confirmed by the first comprehensive study focusing on rock glaciers in the Alaska Range conducted by Wahrhaftig and Cox (1959): they measured the surface and frontal motion of Clear Creek rock glacier by revisiting the positions of painted lines of boulders during an eight-year survey and revealed that the annual displacements at different points were nearly constant. Moreover, based on geomorphological evidence, Wahrhaftig and Cox (1959) suggested the presence of internal deformation that “most or all of the thickness of each rock glacier is involved in the motion, not merely a thin layer on the surface”.

As demonstrated by these early studies, kinematics has always been one of the critical aspects for studying rock glaciers because it reveals their dynamic nature and distinguishes them from other periglacial landforms. Monitoring rock glacier kinematics was conducted *in situ* at first and later combined with remote sensing methods, which have become widely used with the emergence of technological advancements in recent years. Remote sensing-based methods are generally more efficient and less costly for measuring surface kinematics of rock glaciers located in remote areas, whereas *in situ* monitoring can provide surface measurements with better temporal and spatial resolution. In addition, some *in situ* methods can detect internal motion of rock glaciers, which offers insights into the dynamic mechanisms yet cannot be achieved by remote sensing methods so far (Arenson et al., 2016). In the following sub-

sections, we summarize the monitoring methods for measuring internal and surface motion of rock glaciers, respectively.

2.1.1 Methods for detecting surface kinematics

Pioneering research investigated rock glacier movement using simple approaches such as revisiting and measuring the distance between the landform front and a nearby reference point (Chaix, 1919). The measurement accuracy soon improved by applying conventional geodetic methods such as retrieving the positions of profile lines of marked boulders by theodolite (Wahrhaftig and Cox, 1959; White, 1971, 1976). As a modern terrestrial geodetic tool, the Differential Global Positioning System (DGPS) has long been adopted and provides accurate three-dimensional (3D) point measurement of surface displacement with high temporal resolution (Berthling et al., 1998; Krainer and Mostler, 2006; Lambiel and Delaloye, 2004; Wirz et al., 2014).

Terrestrial photogrammetric method was applied to measure rock glacier surface kinematics as early as 1936 (Pillewizer, 1938). Later the manual point-to-point and grid analysis of aerial photography was introduced to reconstruct rock glacier movement in the European Alps and Northern Tien Shan (Barsch and Hell, 1975; Gorbunov et al., 1992; Haeberli et al., 1979; Messerli and Zurbuchen, 1968). Spatial resolution and accuracy of photogrammetric analysis were soon improved with the development of computer-based algorithms (Haeberli and Schmid, 1988; Janke, 2005; Käib et al., 1997), and monitoring rock glacier activity on a regional scale became possible (Roer and Nyenhuis, 2007). Historical aerial photographs, such as the declassified Corona satellite images acquired during the 1970s, have also been analyzed to obtain long-term kinematic time series in inaccessible regions (Sorg et al., 2015). In recent years, with the rapidly developing technology of Remotely Piloted Aircraft System (RPAS, also referred to as Unmanned Aerial Vehicle or UAV), acquisition of high-resolution optical images has become more convenient. New photogrammetric processing methods, especially the Structure-from-Motion (SfM) technique, are able to generate 3D Digital Surface Models (DSM) and have been employed to compute surface displacements with higher precision and sampling density (Marcer et al., 2021; Vivero and Lambiel, 2019).

Airborne and Terrestrial Laser Scanning (ALS and TLS, also referred to as Light Detection and Ranging, LiDAR) can be used to produce repeat Digital Terrain Models (DTMs) with similar accuracy as the SfM method. In the European Alps, TLS campaigns were carried out to quantify mass movement including rock glacier creep (Avian et al., 2009; Bauer et al., 2003; Bodin and Schoeneich, 2008). Then a combined use of ALS and TLS was implemented to measure surface movement of a few rock glaciers in the Swiss Alps (Buchli et al., 2018;

Kenner et al., 2014; Kenner et al., 2017). Bollmann et al. (2015) derived a rock glacier activity index based on displacement rate calculated by ALS.

Interferometric Synthetic Aperture Radar (InSAR) has been widely used for monitoring Earth's surface deformation since the 1990s (Massonnet and Feigl, 1998). Due to its advantage of global access and ability to map the complete displacement field across the landform, InSAR began to be adopted for detecting rock glacier surface movement in remote permafrost areas (Kenyi and Kaufmann, 2003; Nagler et al., 2002; Rignot et al., 2002; Rott and Siegel, 1999). One limitation of InSAR is that the measurement is one-dimensional and along the satellite line-of-sight (LOS) direction (Barboux et al., 2014; Lilleøren et al., 2013; Necsoiu et al., 2016; Strozzi et al., 2020). Some studies reprojected the 1D LOS displacement to surface-parallel or downslope direction to represent the motion of rock glaciers (Liu et al., 2013; Rignot et al., 2002; Wang et al., 2017). Recently, the increasingly available satellite SAR images permitted the application of the Small Baseline Subset (SBAS) algorithm to construct time series of rock glacier surface kinematics (Necsoiu et al., 2016; Reinosch et al., 2021). In addition, terrestrial radar interferometry has been used in combination with space-borne InSAR (Strozzi et al., 2015).

2.1.2 Methods for detecting internal kinematics

Monitoring internal motion of rock glaciers is costly and limited to a few study sites so far. The most frequently used tool is the slope inclinometer installed along the profile of a borehole. Such surveys have been conducted in a few rock glaciers in the European Alps since the 1980s (Arenson et al., 2002; Buchli et al., 2018; Hoelzle et al., 1998; Ikeda et al., 2008; Krainer et al., 2015; Wagner, 1992). Shape Accel Array (SAA) is an advanced instrument which allows continuous monitoring of internal deformation in boreholes and accommodates larger displacement than conventional slope inclinometers. It has recently been adopted for monitoring rock glacier internal kinematics in the Swiss Alps (Buchli et al., 2013). Additional method includes placing steel rods on the frontal talus of a rock glacier and recording their 3D position change over time (Käb and Reichmuth, 2005).

2.2 Kinematic characteristics

Knowledge of rock glacier kinematics is widely variable and dependent on the techniques adopted for monitoring the movement. However, common knowledge gradually emerges with the increasing number of observations by various monitoring methods. In this section, we summarize the magnitude of rock glacier kinematics, its surface and internal distribution, and the different patterns of surface kinematics at different temporal scales.

2.2.1 Magnitude and spatial distribution

Not all rock glaciers are in motion. For the active ones, typical surface movement rate is usually in the magnitude of decimeters per year and less than 3 m yr^{-1} (Barboux et al., 2020). In recent years, drastic collapse events occurred in several rock glaciers in the European Alps (Bodin et al., 2017; Roer et al., 2008): their surface velocities can be as high as 10 m yr^{-1} ; an extreme value equivalent to 100 m yr^{-1} has been observed on the Graben Gufer rock glacier located in the Swiss Alps during 2009–2010 (Delaloye et al., 2010). This abnormal kinematic behavior is referred to as “rock glacier destabilization”, which often initiates with cracks developing on the surface and involves a large part of or even the entire landform when it finally happens (Marcer et al., 2021; Marcer et al., 2019; Scotti et al., 2017). Destabilized rock glaciers (or rock glaciers displaying comparable motion rates) have also been identified in other mountain ranges worldwide (Eriksen et al., 2018; Iribarren Anacona and Bodin, 2010).

Surface kinematics of rock glaciers generally displays a relatively uniform spatial pattern in their central part and slows down towards their lateral and frontal margins (Barboux et al., 2020). It can also show a certain degree of spatial heterogeneity, as controlled by the complex internal structure and topographical features (Avian et al., 2005; Buchli et al., 2018). Vertical distribution of rock glacier kinematics has been revealed by a few borehole investigations. The most significant feature observed is that the majority of displacement (60%–90%) concentrates in a layer located at depth (16–30 m from the surface), which is named as the “shear horizon” (Arenson et al., 2002; Haeberli et al., 2006; Haeberli et al., 1998). Similar vertical distribution pattern was found in later investigations on rock glacier internal deformation as well (Buchli et al., 2018; Krainer et al., 2015).

2.2.2 Centennial to millennial variations

Records of rock glacier surface kinematics measured by the monitoring techniques summarized in Section 2.1 can be traced as far back as the beginning of the 20th century. Beyond this time frame, rock glacier kinematics is only discussed in a few cases based on indirect evidence derived from geochronological methods such as the surface exposure-age dating techniques or dendrogeomorphological analysis (Böhlert et al., 2011; Scapozza et al., 2014; Shroder, 1978; Sorg et al., 2015). By analyzing the dating results, different rock glacier activity phases can be recognized: Böhlert et al. (2011) derived two active phases from five rock glaciers in the Swiss Alps: one occurred shortly after the Younger Dryas (11.6 ka) and lasted until the Holocene Climatic Optimum (HCO, 9–5 ka); the other started between 10–6 ka and continues until today. Scapozza et al. (2014) detected possible accelerations of Stabbio di Largario rock glacier (also situated in the Swiss Alps) during the Medieval Warm Period (MWP, AD 950–1250).

2.2.3 Decadal variations

Direct observations conducted by a combined use of different monitoring methods provide decadal to multi-decadal record of surface kinematics of rock glaciers situated in the European Alps (e.g., Avian et al., 2005; Barsch and Hell, 1975; Bodin et al., 2009; Bodin et al., 2018; Francou and Reynaud, 1992; Hartl et al., 2016; Käab et al., 2007; Kaufmann and Ladstätter, 2006a; Kellerer-Pirklbauer and Kaufmann, 2012; Krainer and Mostler, 2006; Lugon and Stoffel, 2010; Roer et al., 2005), in the Rocky Mountains of Colorado and Wyoming (Janke, 2005; Potter et al., 1998), in the Chilean Andes (Monnier and Kinnard, 2017), in northern Norway (Eriksen et al., 2018), and in the northern Tien Shan (Käab et al., 2021; Sorg et al., 2015).

Contrasting patterns of kinematic changes in terms of trend and timing have been observed in different regions and among different rock glaciers in the same mountain range as well. In the European Alps where most long-term kinematic surveys have been conducted, an accelerating trend starting from the 1990s was reported consistently by several studies (e.g., Avian et al., 2005; Delaloye et al., 2008; Kellerer-Pirklbauer et al., 2018; Roer et al., 2005). Continuous monitoring of rock glacier kinematics in the Swiss Alps has been initiated since 2000. In general, the mean velocity of all study sites has been increasing during the last two decades, with the maxima occurring in 2015 and a continuing acceleration trend after a temporary decrease in 2016/2017 (PERMOS, 2021). In the Rocky Mountains, however, a 21-year (1978–1999) kinematic survey did not observe any significant changes (Janke, 2005), which is consistent with the findings from a 32-year (1963–1995) measurements on Galena Creek rock glacier in the same mountain range conducted by Potter et al. (1998).

Without any data available in the 1990s, a rock glacier complex in northern Norway has experienced an acceleration from 0.5 m yr^{-1} during 1954–1977 to 3.6 m yr^{-1} during 2006–2014, and the movement rate has further increased from 4.9 m yr^{-1} to 9.8 m yr^{-1} during 2009–2016 (Eriksen et al., 2018). Similar accelerating trend during the last more than one decade compared with the 1950s has been observed on five rock glaciers in the northern Tien Shan, whereas among three out of the five rock glaciers, a highly active phase also occurred in the 1960s (Käab et al., 2021; Sorg et al., 2015). The high-velocity period during the 1960s has also been reported in a few other cases in the Austrian and Swiss Alps (Kaufmann and Ladstätter, 2006b; Lugon and Stoffel, 2010).

In contrast, three glacier-rock glacier transitional landforms in the Chilean Andes displayed an overall decreasing motion trend during 1955–2014, meanwhile the terminus of one rock glacier (Las Tetas) had been accelerating or even destabilizing recently from 2000 to 2012 (Monnier and Kinnard, 2017).

2.2.4 Seasonal and sub-seasonal variations

Seasonal and sub-seasonal kinematic characteristics have been mainly derived from observations on rock glaciers in the European Alps. Many rock glaciers display a pronounced seasonal rhythm: rock glaciers accelerate in early summer and reach their maxima between late summer to early winter and minima in late spring; the magnitude of seasonal variations can be as high as 150% of the annual mean velocity (e.g., Delaloye et al., 2010; Ikeda et al., 2008; Kenner et al., 2017; Wirz et al., 2016a). This seasonal pattern does not occur on all rock glaciers though, a few rock glaciers have been reported to move at constant rates all year round, such as the Murt à-Corvatsch and Reichenkar rock glaciers (Haeberli et al., 1998; Krainer and Mostler, 2006).

Velocity peaks at shorter time scales, such as days to weeks, have also been observed, but the motion is usually limited to the surficial active layer associated to the tilting of boulders (Buchli et al., 2018; Wirz et al., 2014; Wirz et al., 2016b).

2.3 Dynamic mechanisms

From the mechanical perspective, rock glaciers are downslope creeping masses of debris-ice mixture driven by their weight. Although several geophysical surveys have revealed a highly heterogeneous internal structure in rock glaciers (e.g., Arenson et al., 2010; Buchli et al., 2018), the active parts of rock glaciers can be vertically divided into three distinct units from the surface to the bottom, namely the active layer, the ice-rich core, and the shear horizon, the deformation of which all contribute to the detected surface displacements. Cicoira et al. (2020) has summarized the structural, compositional, thermal, and kinematic characteristics of the three vertical units in detail. The motion taking place in the topmost active layer is usually caused by boulder tilting or sliding as random and discrete dynamic events. Difficult to monitor as the active layer deformation is, it generally contributes little to the total observed kinematics and thus can be ignored in the first approximation for most rock glaciers (Cicoira et al., 2019b; Wirz et al., 2016b). Therefore, rock glacier kinematics essentially represents the permafrost creep process occurring at depth, i.e., the sum of the steady-state creep strain rate of ice-rich core and shear horizon. As both units are in the permafrost domain, the dynamic mechanisms of rock glaciers have been systematically investigated in the field of debris-ice (or frozen soils, ice-rock system) rheology, which studies the deformation and flow of materials consisting of debris and ice with unfrozen water involved under terrestrial surface and near-surface conditions (Arenson et al., 2007; Ladanyi, 2003, 2006; Moore, 2014).

2.3.1 Major controlling variables

Rheological behavior of debris-ice mixture is primarily controlled by the debris concentration: pioneering research on frozen soil mechanics has discovered that the pore ice governs the deformation when volumetric debris content is less than ~42%. As the debris fraction increases (>42%), it causes strengthening of the mixture by introducing the interparticle friction that impedes the creep deformation of ice (Ting et al., 1983). However, contradictory observations have been reported: several studies have found that the addition of debris decreases the shear strength and makes the mixture deform more rapidly than pure ice under similar conditions (Bucki and Echelmeyer, 2004; Ikeda et al., 2008). This phenomenon is partly attributed to the lubricating and stress-modulating effects exerted by the unfrozen water concentrating at the debris-ice interfaces (Arenson et al., 2007; Cuffey and Paterson, 2010). This pair of competing effects produced by the presence of debris have been reviewed comprehensively by Moore (2014), which also highlights the other first-order variables that govern the debris-ice deformation, including debris particle size, temperature, salinity, and stress. To facilitate the discussion on the above controlling processes and factors, principal mathematical formulations of the rock glacier dynamics are introduced as follows.

2.3.2 Principal mathematical formulations

Most rheological studies on rock glacier creep start with the constitutive relationship depicting ice flow known as the Glen's flow law, which relates strain rate ($\dot{\varepsilon}$) with shear stress (τ) (Glen, 1955):

$$\dot{\varepsilon} = A\tau^n , \quad (2.1)$$

where the fluidity parameter A and the exponent n are creep parameters primarily affected by the preceding first-order variables. The gravity-induced driving stress (τ) at a given depth (z) can be formulated as:

$$\tau = \rho g z \sin\alpha , \quad (2.2)$$

where ρ is the density of the creeping mixture, g is the gravitational acceleration, α is the surface slope angle.

The key problem for mathematically expressing the flow law of debris-ice mixture is to determine A and n appropriately. Three methods are available for solving this issue, depending on the individual research purposes. First, the expressions or values of creep parameters (A and n) derived experimentally from glaciological studies can be used for reference (e.g., Amschwand et al., 2021; Haeberli et al., 2006; Hausmann et al., 2007; Käib et al., 2007; Whalley and Azizi, 1994), because debris-poor mixture (<42%) shows rheological

behaviour similar to clean ice and many rock glaciers have the ice contents reaching the threshold, especially in the ice-rich core unit. Second, the creep parameters can be calibrated using numerical modelling method with rock glacier in situ measurement including deformation rate, material composition, and landform geometry (e.g., Monnier and Kinnard, 2016). Finally, A and n can be obtained from laboratory deformation experiments on frozen soils (Andersland and Ladanyi, 2003; Arenson and Springman, 2005b). So far, Arenson and Springman (2005a) present the optimal parameterization scheme based on rheological experimental behaviour of rock glacier borehole samples. The expression of fluidity parameter A is derived from the Arrhenius relation (Mellor and Testa, 1969), and dependent on temperature (T) and volumetric ice content (w_i):

$$\log A = \frac{2}{1+T} + \log(5 \times 10^{-11} e^{-10.2w_i}), \quad (2.3)$$

The creep exponent n is linearly dependent on the ice content w_i :

$$n = 3.0w_i, \quad (2.4)$$

Equations 3 and 4 are applicable to parameterize the Glen-type relationship (Equation 1) describing the rheological behavior of ice-rich frozen soils at temperatures close to 0 °C (> -4 °C) (Arenson and Springman, 2005a), such as the ice-rich core of many rock glaciers (Cicoira et al., 2019a). The shear horizon where most deformation takes place, usually develops with a higher debris fraction than the internal friction ensues. For research on rock glacier kinematics at a regional scale, the distinct rheological behavior of shear horizon can be ignored as the detailed information of rock glacier internal structure is generally lacking (Cicoira et al., 2020). However, for studying the mechanisms of rock glacier dynamics, shear horizon is critical because it concentrates most deformation observed from the surface. One way to consider the enhanced deformation is by adding a multiplication factor to the creep exponent (n) in the above expressions (Cicoira et al., 2019a; Frehner et al., 2015). This is an approximation that can numerically simulate the observed deformation rate but cannot take the rheological factors into account. To investigate the governing mechanisms, the constitutive relationships proposed by Ladanyi (2003), which considers the internal friction exerted with the increasing amount of debris, has been applied in recent studies (Cicoira et al., 2019b; Cicoira et al., 2020):

$$\dot{\gamma} = \dot{\gamma}_c \left(\frac{\tau}{\tau_r}\right)^n, \quad (2.5)$$

where $\dot{\gamma}$ is the shear strain rate, $\dot{\gamma}_c$ is the critical shear rate. τ_r is the shear resistance induced by the internal friction of the debris-ice mixture, which follows the Mohr-Coulomb criterion:

$$\tau_r = \tau_{c\theta} + \sigma \tan \phi_c, \quad (2.6)$$

where $\tau_{c\theta}$ is the cohesion and ϕ_c is the friction angle of the material, both of which can be determined based on previous experimental findings with certain theoretical assumptions (Arenson and Springman, 2005b; Ladanyi, 2003). σ is the effective normal stress, which is equivalent to the total normal stress (Equation 2) minus pore fluid pressure (P):

$$\sigma = \rho g z \sin \alpha - P , \quad (2.7)$$

Combining Equations 2.4–2.7, a creep model can be established by which the unfrozen water impact manifests itself as a factor adjusting effective normal stress, whereas temperature is ignored. Such formulation is suitable to characterize the shear horizon rheology because borehole observations have revealed the occurrence of pressurized unfrozen water in the shear horizon, while the temperature remains mostly constant and undisturbed at the seasonal scale (Arenson et al., 2002; Cicoira et al., 2020).

The recent work of Cicoira et al. (2019b) represents the most up-to-date study aiming to investigate rock glacier dynamics, which adopts the two representative frameworks for rheological modelling: the relationships proposed by Arenson and Springman (2005a) for the ice-rich core and the formulations established by Ladanyi (2003) for the shear horizon. In this modelling setup, three controlling factors have been highlighted, namely, temperature (T), water (P), and volumetric ice/debris content (w_i).

2.4 Responses to climatic forcing

As illustrated in the rheological analysis (Section 2.3), the observed rock glacier motion is the consequence of permafrost creep controlled by landform geometry, material constituents, and environmental factors including ground temperature and the amount of unfrozen water in the pore spaces. Therefore, the climatic forcing, such as air temperature and precipitation, contributes to shaping the kinematic characteristics of rock glaciers. Current knowledge of rock glacier kinematic responses to the climatic factors at a range of temporal scales is reviewed in this section.

2.4.1 Centennial to millennial timescales

At centennial to millennial timescales, the recognized active phases of rock glaciers display a synchronous pattern with the warm period in history. A relict rock glacier situated in the Swiss Alps used to show active behaviors shortly after the cold period during the Younger Dryas, and the main activity occurred during the warming period from early Holocene until the Holocene Climatic Optimum (Böhlert et al., 2011). Similar pattern has been observed on an active rock glacier in the southern Swiss Alps, which started its formation after the Mid-

Holocene Climatic Optimum and accelerated during the Medieval Warm Period (Scapozza et al., 2014).

2.4.2 Decadal timescale

The overall accelerating trend of rock glaciers in the European Alps starts from 1990s and continues today, which is concurrent with the general rise in mean annual air temperature (MAAT) since the 1990s (e.g., Käab et al., 2007; Roer et al., 2005). The observed speed-up of Ritigraben and Doesen rock glaciers during the 1950s and 1960s followed by deceleration in the 1970s was also in concert with changes in air temperatures in the European Alps (Lugon and Stoffel, 2010). In northern Norway, acceleration of a rock glacier during 1954–2016 was aligned with the increase in modelled air temperature and precipitation during the 62 years (Eriksen et al., 2018).

Rock glaciers in the Northern Tien Shan in general exhibit steady accelerations since the 1950s, with enhanced speed-up over the last one to two decades, which is consistent with the kinematic response of rock glaciers in the European Alps and northern Norway to atmospheric warming (Käab et al., 2021; Sorg et al., 2015). However, local variability has been discovered in the Northern Tien Shan: three rock glaciers showed high movement rate during 1966–1971 when the temperatures were rather cold. Active behaviors of rock glaciers during these cold years are probably attributed to the early snow cover of above-average heights as recorded by nearby meteorological stations (Bolch et al., 2009), which increased the ground temperature and hence the rock glacier creep (Käab et al., 2021).

In the Rocky Mountains, the insignificant variation in rock glacier kinematics is associated with the unclear climate changing pattern across the mountain range: a slight cooling trend had been observed at above-timberline meteorological sites (Janke, 2005; Pepin, 2000).

In the central Andes, multi-decadal deceleration (1955–2014) has been observed on glacier-rock glacier transitional landforms, the deformation of which are strongly affected by the interactions between rock glaciers and their upslope debris-covered glaciers: the transition from debris-covered glaciers to rock glaciers in the current warming climate may exert a buttressing effect on the upslope part of the landform and lead to a general deceleration (Monnier and Kinnard, 2017). At one of these transitional landforms, Las Tetas rock glacier has been accelerating recently (2000–2012) at the terminus part where the periglacial processes dominate, which is related to the lasting atmospheric warming trend of $0.19\text{ }^{\circ}\text{C}$ decade $^{-1}$ during 1958–2007 in the nearby area as reported by Rabatel et al. (2011).

2.4.3 Interannual timescale

At interannual timescale, the variations of rock glacier kinematics have been reported in the European Alps and compared with the mean annual ground surface temperature (MAGST) influenced by air temperature and the snow conditions (thickness and onset timing), as the snow cover serves as an insulating layer that modulates the ground thermal state (e.g., Bodin et al., 2009; Delaloye et al., 2010; Delaloye et al., 2008). In general, the observed interannual kinematic fluctuations are well correlated with the shifts of MAGST: rock glaciers move at high annual horizontal surface velocities in the years with high MAGST, and vice versa (Delaloye et al., 2008). For instance, strong increase of rock glacier kinematics in the Swiss Alps occurred in 2020 in comparison to the velocity in 2019, in alignment with the ever warming MAGST since 2017 (PERMOS, 2021). By analyzing the time series of rock glacier velocity and snow accumulation, Bodin et al. (2009) highlights the importance of snow cover conditions in controlling rock glacier kinematics: early and thick snow cover insulates the ground from winter cooling and increase the MAGST. Additionally, melt of the large snow accumulation provides external water into the frozen body, which results in significant summer acceleration and hence a high annual mean velocity value. The speed-up impact of water input on the interannual and seasonal kinematic variations will be discussed in detail as follows.

2.4.4 Seasonal timescale

Seasonal kinematic variations of rock glaciers were originally compared with the changes in temperature forcing, i.e., time series of ground surface temperature (GST), by which a time lag of a few months between the extreme values of velocity and GST has been observed (e.g., Delaloye et al., 2010; Kääb et al., 2007). Such delay has been attributed to the time required for the external temperature forcing to propagate into the landform and adjust the ground temperature by heat conductivity (e.g., Haeberli et al., 2006). However, it has been quantitatively demonstrated that the thermal conduction process solely cannot explain the observed kinematic variations in terms of both the amplitude and phase lags (Cicoira et al., 2019a).

Early observations have also revealed a synchronous relationship between the abrupt seasonal acceleration and the onset of snow melting (e.g., Ikeda et al., 2008; Kenner et al., 2017; Perruchoud and Delaloye, 2007), occasionally the increase of velocity is progressive and delayed by about two months compared with the melt of snow as on the Muragl rock glacier (Kääb et al., 2007). Therefore, researchers have long speculated that water plays an important role in controlling the seasonal rhythm of rock glacier kinematics (e.g., Buchli et al., 2018; Delaloye et al., 2010; Hartl et al., 2016; Ikeda et al., 2008; Kenner et al., 2017; Wirz et al.,

2016b). This hypothesis has recently been confirmed using numerical modelling approach: water from precipitation and snow melt, instead of air temperature, is the principal factor controlling the seasonal rhythm of rock glacier creep by changing the pore pressure in the debris-rich shear horizon (Cicoira et al., 2019b).

2.4.5 Destabilization

In the past two decades, destabilized rock glaciers, i.e., rock glaciers with displacement rates increased by as high as two orders of magnitude, have gradually emerged since the first documented destabilization event occurred in the French Alps in 2006 (e.g., Bodin et al., 2017; Marcer et al., 2021). This phenomenon is not triggered solely by climatic forcing but by a combination of factors such as the warming permafrost, the excess water infiltration, the landform lithology, the local overloading of debris, and the geometric settings (Bodin et al., 2017; Delaloye et al., 2013; Ikeda et al., 2008; Marcer et al., 2021; Roer et al., 2008).

Based on observations and empirical modelling, Cicoira et al. (2020) have formulated a theoretical variable, namely the Bulk Creep Factor (BCF), which is able to represent the rock glacier kinematics component contributed by the material rheological properties alone, eliminating the effects exerted by geometric factors. The first order variables controlling the BCF include temperature and water content. Assuming the standard material parameters, a simplified expression of BCF is:

$$BCF = 7.6c_{obs} \sin \alpha \left(\frac{0.5}{\tan \alpha} + 0.1 \right)^{2.1} \quad (8)$$

The BCF can be calculated conveniently with simple input parameters including observed creep velocity (c_{obs}) and surface slope angle (α).

One application of the BCF is to identify the destabilized rock glacier in a quantitative way: in a destabilizing area, the BCF can abruptly jump to high values close to 20 and show a discontinuous profile in connection to the upslope steady-creep areas where BCF values are usually smaller than 5. The BCF can be served as a reference value for monitoring the accelerating to destabilizing responses to the climate warming (and in some cases wetting as well) in the long run.

2.5 Research milestones

Year	Research milestone	Reference
1900	First article on “a peculiar form of talus” (rock glacier) was published on <i>Science</i> journal	Spencer (1900)
1910	The term “rock glacier” was coined with detailed geomorphic description	Capps (1910)
1919	Simple field measurements of rock glacier motion were carried out	Chaix (1919)
1936	Terrestrial photogrammetry was applied to measure rock glacier kinematics	Pillewizer (1938)
1959	First comprehensive kinematic study on rock glaciers by theodolite	Wahrhaftig and Cox (1959)
1968	Aerial photogrammetry was used for measuring rock glacier movement	Messerli and Zurbuchen (1968)
1976	The hydrological value of rock glaciers was proposed	Corte (1976)
1977	Rock glaciers were recognized (as possible features) on Mars	Carr and Schaber (1977)
1987	First borehole was drilled on Murtal-Corvatsch rock glacier	Haeberli et al. (1998)
1996	The first monograph on rock glaciers was published	Barsch (1996)
1997	DGPS was used for rock glacier kinematics survey	Berthling et al. (1998)
1998	“Shear horizon” was observed and coined	Haeberli et al. (1998)
1999	InSAR was introduced to measure rock glacier movement	Rott and Siegel (1999)
2003	Laser scanning was adopted in rock glacier kinematics monitoring	Bauer et al. (2003)
2005	Triaxial tests were conducted on rock glacier borehole samples	Arenson and Springman (2005b)
2006	First documented rock glacier destabilization event occurred	Bodin et al. (2017)
2010	Seasonal rhythm of rock glacier movement was characterized	Delaloye et al. (2010)
2018	IPA Action Group on rock glacier inventories and kinematics was established	Delaloye et al. (2018)
2019	Water was found to be the controlling factor on the seasonal rhythm of rock glacier kinematics by numerical modelling approach	Cicoira et al. (2019b)

2.6 Summary

In this chapter, we synthesize the current literature to present an overview of rock glacier kinematics, which serves as the background knowledge for this thesis. We highlight the key points of this review by addressing the four primary questions raised at the beginning:

Question 1: How to measure rock glacier kinematics?

- (1) For measuring surface kinematics, major monitoring methods include conventional geodetic survey, DGPS, optical photogrammetry, laser scanning, and InSAR.
- (2) For measuring internal deformation rates, the frequently adopted instruments are slope inclinometers and SAAs.

Question 2: What are the kinematic characteristics of rock glaciers?

- (1) Active rock glaciers typically move at a rate less than 3 m yr^{-1} , which could increase by one to two orders of magnitude if destabilization occurs.
- (2) Surface kinematics of rock glaciers distributes in a relatively uniform spatial pattern in the central parts, and the vertical distribution is characterized by a shear horizon at depth, where most deformation concentrates.
- (3) At centennial to millennial timescales, case studies in the Swiss Alps have recognized active phases between the Younger Dryas and the Holocene Climatic Optimum, and during the Medieval Warm Period.
- (4) Investigations of decadal to multi-decadal kinematic changes have been conducted globally and revealed various patterns. Many rock glaciers in the European Alps have been accelerating since the 1990s. Similar speed-up trend has occurred in northern Norway and northern Tien Shan during the past one to two decades. Another common active period is the 1960s, which has been identified on several rock glaciers in the northern Tien Shan and the European Alps. Rock glaciers in the Rocky Mountains, however, moved at a nearly constant rate during the second half of the 20th century. A few glacier–rock glacier transitional landforms in the Chilean Andes showed a decelerating trend during the past 50 years, whereas possible destabilization occurred on one rock glacier in recent years.
- (5) Short-term variations usually manifest as a consistent seasonal rhythm: rock glaciers accelerate in early summer and reach their maxima between late summer to early winter and minima in late spring.

Question 3: What are the dynamic mechanisms controlling rock glacier movement?

- (1) The observed surface kinematics of rock glaciers essentially represents the permafrost creep process occurring at depth, i.e., the sum of the steady-state creep strain rate of ice-rich core and shear horizon.
- (2) Research on debris-ice rheology has revealed that the debris concentration is the primary controlling factor. Other first-order variables include debris particle size, temperature, salinity, and stress.

Question 4: How do rock glacier kinematics respond to climatic factors?

- (1) Air temperature contributes to the long-term rock glacier kinematic evolution by changing the ground temperature via heat conduction. Supportive field evidence includes: the synchronization between rock glacier active phases and historical warm periods and the positive correlation between MAAT and rock glacier velocities at decadal scale.
- (2) Liquid and solid precipitation primarily controls the short-term seasonal kinematic variations by changing the pore pressure in shear horizon. Field observations have reported the concurrence between snow melt and rock glacier seasonal acceleration. Recent numerical modelling work also supports this mechanism.
- (3) Snow cover conditions influence the short-term variations in two ways: adjusting the ground temperature as an insulation layer and providing external water input during the melting season. Observations of interannual and seasonal kinematic variations have confirmed this controlling factor.
- (4) Rock glacier destabilization is a consequence of multiple factors including long-term warming, excess water, and geometric characteristics as well. The recently proposed BCF can be used for monitoring the possible long-term kinematic evolution from acceleration to destabilization in the current warming climate.

Chapter 3 Quantification of permafrost creep provides kinematic evidence for classifying a puzzling periglacial landform

"I knew who I was this morning, but I've changed a few times since then."
—Lewis Carroll, *Alice's Adventures in Wonderland*

Mechanical processes operating on the slope surface or at depth control the dynamics of alpine landforms and hold critical information of their geomorphological characteristics, yet they often lack systematic quantification and in-depth interpretation. This study aims to address a long-standing issue concerning geomorphological classification from a kinematic perspective. A group of periglacial landforms consisting of several lobes were discovered in the East Kunlun Mountains of China 30 years ago but were ambiguously classified as rock glaciers and later as gelifluction deposits. Here, we use satellite Interferometric Synthetic Aperture Radar to quantitatively characterize the spatial and temporal changes of the surface movement of these landforms. We observe that: (1) its 17 lobes show a pattern of landform-scale and uniform surface movement, especially during May to October; (2) the lobes move at a spatial mean downslope velocity of $10\text{--}60 \text{ cm yr}^{-1}$ and a maximum velocity as high as 100 cm yr^{-1} in summer; (3) the landforms are nearly inactive from winter to late spring. Based on these observations, we postulate that the movement of the lobes are driven by deep-seated permafrost creep which typically occurs in rock glaciers. The debris of Lobe No.4 is composed of both boulders and pebbles supported by fine-grained matrix generated from the in-situ weathering process. It develops a talus-like over-steepened front around 40° and a convex transverse profile perpendicular to the creep direction, which are also characteristic features of a rock glacier. Piecing these observations together, we identify Lobe No.4 as a debris-mantled-slope-connected rock glacier, with the gelifluction process occurring on the surface as small-scale and discrete events.

3.1 Introduction

Various mass-movement processes operating in cold mountain regions in response to the environmental forcing transport the materials, modify the surface features, and contribute to the development of diverse periglacial landscapes (Ballantyne, 2018). Periglacial landforms such as rock glaciers and solifluction lobes are commonly recognized by their geomorphological characteristics, which are distinct from one another and indicate the dynamic processes contributing to shape them, whilst occasionally it is problematic to identify the nature of the landforms with the geomorphological approach alone. In that case, the extensive discussion of the definition of rock glaciers best illustrates the underlying ambiguity (Barsch, 1996; Berthling, 2011; Delaloye and Echelard, 2020; Haeberli, 2000; Humlum, 1988;

Wahrhaftig and Cox, 1959). Ubiquitous and impressive as rock glaciers are, their identification based on geomorphological features remains contentious and subjective to some degree (Brardinoni et al., 2019), which further hinders the understanding of the mechanism of the prevailing processes and the significance of the consequent landform evolution.

Such ambiguity can be principally attributed to the highly complex relationships between the geomorphological processes and the morphological features displaying in the landforms (Anderson et al., 2018; Berthling, 2011; Knight et al., 2019). Nevertheless, with the development of observational methods, research focusing directly on the processes, especially by measuring the kinematics, provides insight into the nature of the evolving landforms (Barboux et al., 2014; Dini et al., 2019). The observed kinematics serves as an insightful and complementary perspective to understand a landform, although the kinematics alone cannot eradicate the existing ambiguity and subjectivity in classifying a landform, which essentially relies on its geomorphological characteristics.

Here we investigate the kinematic characteristics and discuss the geomorphological classification of a group of active periglacial landforms in the East Kunlun Mountains on the Qinghai-Tibet Plateau (QTP). These landforms were first discovered and explored three decades ago but were ambiguously classified as “Kunlun-type” rock glaciers due to the unique “ice-cap-shaped” deposit covering the upslope parts of all the tongue-shaped features and slow creeping rates (Cui, 1981, 1985). However, the nature of the lobes has remained contentious and later been interpreted as gelifluction deposits because small-scale and low-velocity gelifluction on the surface of the landform had been observed in the fieldwork whereas evidence for the movement as a continuous sheet was lacking (Harris et al., 1998).

This study primarily aims to approach the previous research question centering on the classification of the periglacial landforms near Jingxian Valley, in a way that integrates the kinematic and geomorphologic features of the landforms. We employed the Interferometric Synthetic Aperture Radar (InSAR) technique to quantify the temporal and spatial variations of the downslope creeping velocities. We conducted geodetic measurements and in-situ field surveys to provide detailed geomorphological information. Our quantitative description of this group of landforms extends the relatively limited knowledge of the periglacial landforms especially rock glaciers in western China (Ran and Liu, 2018; Wang et al., 2017), and demonstrates the diversity and complexity of rock glaciers and related landforms and processes.

3.2 Rock glaciers versus gelifluction deposits

Rock glaciers and gelifluction deposits primarily distinguish from each other in the dominant processes operating on them, thus the interpretation of the annual or interannual landform evolution diverges from each other. Rock glaciers are characterized by the permafrost creep process occurring at depth, which consists of plastic deformation of ice-rich permafrost and deformation in the shear horizon (Arenson et al., 2002; Berthling, 2011; Ciccoira et al., 2019b; Haeberli, 2000; Kenner et al., 2019). In contrast, gelifluction deposits are formed by deformation process which operates on the surface or in the shallow layer of the ground due to high pore water pressure generated by annual soil thawing or occasionally inflow of external water (Ballantyne, 2018; Matsuoka, 2001). In addition to gelifluction process, annual frost creep triggers downslope movement resulting from the volumetric oscillation induced by annual freeze–thaw cycle in alpine permafrost environment. During the annual freezing process, a frost heave perpendicular to the slope occurs, then the thawing process causes the soil to subside vertically, which generates a displacement in the downslope direction. In practice, however, it is difficult to distinguish between gelifluction and annual frost creep process, as both of them are associated with cyclic freezing and thawing of the active layer, and operate in combination on the slopes in permafrost area (Ballantyne, 2018; Matsuoka, 2001). Therefore, from a geomorphological perspective, the term gelifluction deposit as referred to by Harris et al. (1998) is in the form of a solifluction lobe which is shaped by both gelifluction and annual frost creep processes.

Such divergent processes shape the contrasting morphometric and kinematic features of the rock glaciers and solifluction lobes (Table 3.). A major difference between the morphology of the two types of landforms lies in their typical dimension, especially in the frontal height of the lobe, which indicates the maximum depths of the motion (Matsuoka et al., 2005). Shear horizon, along which the permafrost creep process operates, is commonly located more than ten meters deep in a rock glacier (Arenson et al., 2002; Buchli et al., 2018). In comparison, the gelifluction and annual frost creep process involve only the surface or a shallow layer of materials (less than 60 cm) (Matsumoto et al., 2010; Matsuoka, 2001). Therefore, rock glaciers usually develop lobate or tongue-shaped bodies with a front as high as tens of meters, whereas solifluction lobes have much smaller sizes with frontal heights rarely exceeding 3 m (Matsuoka et al., 2005). Furthermore, rock glaciers are recognizable by their characteristic frontal and lateral marginal morphology, and distinct ridge-furrow topography on the surface (Wahrhaftig and Cox, 1959; Barsch, 1996; Ballantyne, 2018; Delaloye and Echelard, 2020). Solifluction lobes, however, lack descriptions in terms of their detailed structural or textural features due to their small overall dimensions which are on average less than 10 m in length and width (Matsuoka et al., 2005). Additionally, several solifluction lobes aggregate and create

a larger landform, the extent of which may be comparable to rock glaciers, yet the structural features of rock glaciers are unlikely to develop on the aggregated landforms.

Kinematic behaviors of the two types of landforms are directly controlled by the mechanisms of the different dynamical processes. Note that an absolutely unambiguous differentiation between their kinematic features should be based on measurements of deformation at depth, yet the characteristics of surface deformation, which tend to be more readily accessible to researchers, also hold implications of the controlling processes. The surface of a rock glacier tends to creep as a whole, resulting from the deformation taking place in the shear horizon at depth (Haeberli, 2000; Arenson et al., 2002). The typical annual creep rate of rock glaciers is in the order of several decimeters per year and usually no more than 2 m yr^{-1} (Barsch, 1996), though much larger velocities have been observed and reported as several meters per year (Delaloye and Echelard, 2020; Delaloye et al., 2013; Eriksen et al., 2018). Seasonal kinematic variations are common among rock glaciers and have been observed at numerous sites with various monitoring methods (Delaloye et al., 2010; Käb et al., 1997; Krainer and Mostler, 2006; Lambiel and Delaloye, 2004; Wirz et al., 2014). According to these studies, a typical seasonal rhythm comprises an acceleration in early summer and a deceleration starting between autumn and winter. The creep velocity reaches its maximum during summer to early winter and its minimum in late spring (Delaloye et al., 2010; Wirz et al., 2016b). In some cases, no movement can be detected during the low-velocity period (De Sanjose et al., 2014). Previous studies using in-situ observations (Delaloye et al., 2010; Ikeda et al., 2008; Krainer and Mostler, 2006), laboratory experiments (Arenson and Springman, 2005b), rheological studies (Arenson and Springman, 2005a; Jansen and Hergarten, 2006), as well as numerical modeling (Cicoira et al., 2019a; 2019b) have investigated the mechanism of this distinctive seasonal behavior and proposed the ground temperature and water input as the controlling environmental factors. Recent studies (Cicoira et al., 2019b; Kenner et al., 2019) have suggested that water is the primary driver governing the velocity changes in rock glaciers. A time lag of a few months generally exists between the seasonal rhythm of velocity and the rapid change of air or ground surface temperatures, while the response time to the water input is as short as a few days (Wirz et al., 2016; Cicoira et al., 2019a).

Frost creep induced by the annual thaw consolidation of shallow materials can be uniform and extend over a portion of the slope, while gelifluction triggered by the elastoplastic deformation of saturated soils appears as discrete and localized displacement (Harris et al., 2003; Jaesche et al., 2002; Kinnard and Lewkowicz, 2005). In addition, movement of the aggregation of lobes display a higher degree of heterogeneity. The recorded surface velocities of solifluction lobes are a superposition of the movements caused by the two processes. The solifluction rate is strongly affected by the local climate and slope topography and is usually smaller than 100

mm yr⁻¹. The annual frost creep contributes the majority of the total surface displacement, and the theoretical maximum velocity can be estimated based on the magnitude of frost heave and slope angle (Williams, 1991). Such downslope displacement takes place simultaneously or immediately after the onset of seasonal thawing; the duration of the movement is short, usually in a few days (Matsuoka, 2001). The surface movement arising from gelifluction mainly operates in parallel with the annual frost creep component or as an abrupt and random event during external water input (Matsuoka, 2001; Jaesche et al., 2002; Kinnard and Lewkowicz, 2005).

Table 3.1 Dynamical processes of rock glaciers and solifluction lobes and their typical kinematic and morphometric features.

	Dynamical process	Kinematic behavior			Morphometric feature	
		Extent	Rate	Timing	Frontal height	Characteristic structure
Rock glacier	Permafrost creep: viscoelastic deformation of permafrost in and above shear zone	High degree of uniformity over the slope	From a few centimeters to several meters per year	Seasonal rhythm; controlled by water pressure	Usually > 10 m	Development of frontal and marginal structure; convex transverse topography
Solifluction lobe	Annual frost creep: downslope movement of shallow soils in response to annual cyclic volumetric oscillation	Uniform in a portion of the slope	Usually < 10 cm yr ⁻¹ ; dependent on local climate and topography	Concurrent with onset of seasonal thawing;	Usually < 3 m	Development of a frontal riser
	Gelifluction: elastoplastic deformation of saturated surface soils	Discrete and localized		Concurrent with seasonal thawing and/or water inflow event		

3.3 Study area

The group of landforms is located by the Qinghai-Tibet Highway near Jingxian Valley at the Kunlun Pass in the northern QTP of China (N94.0350 °, E35.6940 °, Figure 3.1a). Debris covers the uppermost part of the mound and extends a series of tongue-shaped landforms (17 in total) ranging in elevation from 4900 m to 4690 m. The lobes are large in dimension, the lengths of which are generally between 300 m to 600 m (Figure 3.1b, c).

Lobe No.4 (N94.0430 °, E35.6992 °) has drawn much attention in the previous studies due to its relatively high motion rate and easy accessibility (Cui, 1985; Harris et al., 1998). The debris consisting of the landforms mainly originates from the in-situ weathering of the Middle Pleistocene till sediments (Wu et al., 2001). The surface materials are a mix of angular boulders and pebbles whose lithologies are crystalline rocks ranging from granites to pyroxenite, all of which occur in the till (Harris et al., 1998). The ultrabasic–basic rocks in the till originates from bedrocks locating 30 km west to Xidatan, and the source of the acid constitutes occurs to the north of the study area (Wu et al., 2001). In contrast to the alpine meadow covering most of the surrounding stable slopes, vegetation is rare on the surface of the landforms.

The study site is located near the northern boundary of the QTP permafrost zone, where the lower limit for the presence of permafrost is around 4360 m. The local climate is cold and dry: the mean annual air temperature (MAAT) is -3.7 °C and the mean annual precipitation is 393 mm. The permafrost distribution and meteorological data are measured at the nearby Xidatan permafrost monitoring station (N94.1333 °, E35.7167 °) during the period of 2009–2019 (Zhao and Sheng, 2019). Moreover, previous drilling and geophysical surveys have revealed that the occurrence of underlying permafrost is continuous below the landforms (Harris et al., 1998).

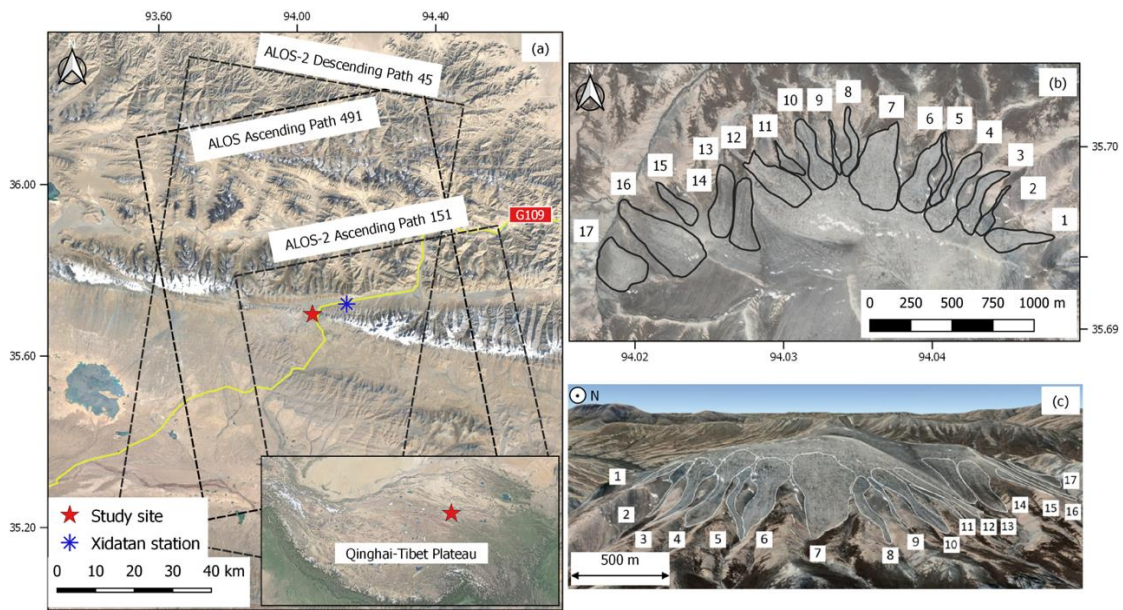


Figure 3.1 (a) Google Earth images showing the location of the study site and the ground tracks of the SAR images used in the study; (b) topographical map showing the extent and shape of the landforms (c) side-looking image of the 17 lobes extending down to the valley.

3.4 Methods

In this section, we first describe the details of the field observations and sample collection procedure. Then we introduce the specifications of the unmanned aerial vehicle (UAV) survey we conducted for measuring surface topography of the landforms. Finally, we present the dataset and InSAR processing details for calculating the surface displacements and further converting them to downslope velocities.

3.4.1 Field observations and soil sampling

During the field investigation, we visited three lobes, which were marked as Lobes No.3, 4, and 5 in the previous studies (Harris et al., 1998), and observed Lobe No.4 in detail. We carried out two field excursions to investigate the previously well-studied Lobe No.4 on June 12th 2018 and from 17th to 18th September 2019. We observed the lithology and grain size distribution of the surface debris as well as local features such as small gullies, deformed vegetation and surface running water occurring on the lobe.

We excavated two test pits on the upper and lower slope to investigate the material constitution of the active layer profile. Soil samples were collected by 100 ml cutting rings with 20 cm sampling interval from the two profiles at depths of 0–160 cm and 0–180 cm, respectively. The collected samples were stored in the hermetic aluminum boxes (120 ml). Both profiles were located within the extent of the active layer, as we observed no ground ice during the excavation conducted at the end of the 2019 thaw season.

Soil analyses were conducted at The Cryosphere Research Station on the QTP, Chinese Academy of Sciences. We measured the mass soil moisture (m_m) in each soil sample adopting the oven-drying method (105°C, 24hours), and determined soil bulk density (ρ_b) using the metal-ring method (Tian et al., 2017; Zhao and Sheng, 2015). Then volumetric soil moisture was acquired by the following equation (Lv and Li, 2006):

$$m_v = \frac{m_m \rho_w}{\rho_b} \quad (3.1)$$

where m_v is volumetric soil moisture, and ρ_w is the density of liquid water.

The soil moisture contents were further used to estimate the maximum surface displacement (D_s) resulting from the annual frost creep process by Williams (1991):

$$V_s = \frac{D_s}{T} = \frac{H_F \tan \theta}{T} = \frac{h m_v \tan \theta}{T} \frac{\rho_w - \rho_i}{\rho_i} \quad (3.2)$$

where T equals to 1 year; H_F is the amount of frost heave perpendicular to the ground surface; θ is the slope angle; h is the thickness of the soil layer involved in the annual frost creep process; ρ_i is the density of pure ice.

3.4.2 Unmanned aerial vehicle (UAV) survey

We conducted a UAV survey and applied the Structure from Motion/Multi-view Stereo (SfM-MVS) photogrammetry to reconstruct the morphology of Lobe No.4 and its surrounding region on 17th September 2019. We used the flying platform DJI Phantom 4 Advanced and its camera FC6310. The sensor size of the camera is 13.2 mm, and the effective focal length of the 24 mm (35 mm equivalent) prime lens is 8.8 mm. The flying altitude was around 230 m above the ground with a heading overlap of 85% and a lateral overlap of 60%. A total of 645 photos were captured with a rolling shutter to cover a ground surface area of approximately 2.16 km². The image size is 5472 × 3648 pixels. We used the open-source software Open Drone Map version 0.7.0 (www.opendronemap.org) to generate a digital orthophoto map (DOM), a digital surface model (DSM), and a 3D surface model by image preprocessing, aerial triangulation, and point cloud editing. We constructed the DOM, DSM, and 3D model with an average ground resolution of 4.39 cm/pixel and resampled the DSM to a grid resolution of 0.5 m. The products were georeferenced using the position and orientation data of the UAV platform instead of ground control points and thus have a meter-level positioning accuracy with respect to the World Geodetic System (WGS84). The uncertainty of the relative location of each pixel within the local coordinate system was estimated to be 0.47 pixels. The accuracies were sufficient for illustrating the ground surface cover and relative topographic relationships among the structural components of the landform (Gao et al., 2017).

3.4.3 Surface velocities derived from InSAR

Five L-band ALOS PALSAR images and fifteen ALOS-2 PALSAR-2 images covering the study area were used to generate eleven interferograms to measure the surface velocities of the landforms (Figure 3.1a). The SAR images in the two datasets were acquired from 2008 to 2009 and from 2015 to 2019, respectively. To achieve high interferometric coherence, we selected the image pairs with temporal spans of less than 70 days and perpendicular baselines shorter than 600 m. Table 3.2 presents detailed information of the interferometric pairs. The interferometric processing was implemented by the open-source software ISCE version 2.2.0 (available at <https://github.com/isce-framework/isce2>). The topographic phase was estimated and removed with the 0.4-arcsec TanDEM-X DEM (spatial resolution ~12 m). We applied a multi-looking operation (two looks in range and five looks in azimuth) and filtered the interferograms using the adaptive Goldstein filter with a window size of 8 by 8 pixels. We re-referenced the phases to a stable point at the flatten surface near a local building. By doing so,

we can effectively remove the atmospheric artifacts such as the water vapor delay and ionospheric effects, because they are spatially long-wave features and can be assumed as constant within the range of our study objects (Hanssen, 2001). Besides, we applied the Generic Atmospheric Correction Online Service for InSAR (GACOS) products, which are derived from weather model and GPS measurements, to further remove the tropospheric delay in the InSAR measurements (Yu et al., 2018a; Yu et al., 2018b; Yu et al., 2017).

We then used the unwrapped interferograms to calculate the surface velocities along the SAR satellite line-of-sight (LOS) over the observation periods. Assuming the surface motion is purely downslope, the LOS velocity (V_{LOS}) can be projected onto the downslope direction (V_{slp}) at each lobe with the equation (Liu et al., 2013):

$$V_{\text{slp}} = \frac{V_{\text{LOS}}}{\sin(\theta_{\text{asp}} - \alpha)\sin\theta_{\text{inc}}\cos\theta_{\text{slp}} + \cos\theta_{\text{inc}}\sin\theta_{\text{slp}}} \quad (3.3)$$

where α is the flight direction of the SAR satellite; θ_{inc} is the local incidence angle; θ_{asp} and θ_{slp} are the aspect angle and slope angle of the lobe, respectively. Finally, we selected the median and maximum value of all pixels within each lobe to represent its kinematic characteristics. The motion direction was manually determined based on the morphology of the landform, and the geomorphic parameters were quantified from the TanDEM-X DEM.

We estimated the uncertainties of downslope velocities by considering the error propagation of the InSAR-derived LOS velocities and geometric parameters used in Equation 3.3. To estimate the uncertainties of the LOS velocities, we first calculated the phase variance (σ_{ϕ}^2) dependent on the coherence and the multi-looking numbers used to derive the phase of each pixel, which was presented by Rodriguez and Martin (1992):

$$\sigma_{\phi}^2 = \frac{1}{2N_L} \frac{1-\gamma^2}{\gamma^2} \quad (3.4)$$

where N_L is the number of looks; γ is the coherence. We estimated the uncertainties of LOS velocities based on the phase variances (σ_{ϕ}^2). Then we quantified the uncertainties of the geometric parameters used in Equation 3.3, namely the aspect angle (θ_{asp}) and the slope angle (θ_{slp}) of the lobe, which are associated with the uncertainty of the DEM (10 m as suggested to be the nominal vertical accuracy of TanDEM DEM). We also assumed a positioning accuracy of 50 m as we manually determined the start and end points of the movement direction.

Table 3.2 List of interferograms generated from ALOS-1 PALSAR and ALOS-2 PALSAR-2 data.

Satellite	Path/frame	Orbit direction	Interferogram acquisition dates	Time span (days)	Perpendicular baseline (m)
ALOS	491/700	Ascending	20080201–20080318	46	56
ALOS	491/700	Ascending	20090621–20090806	46	-382
ALOS	491/700	Ascending	20090806–20090921	46	616
ALOS-2	45/2890	Descending	20150307–20150321	14	-225
ALOS-2	45/2890	Descending	20160305–20160430	56	102
ALOS-2	151/700	Ascending	20160721–20160929	70	-22
ALOS-2	151/700	Ascending	20170720–20170928	70	104
ALOS-2	151/700	Ascending	20180524–20180719	56	92
ALOS-2	45/2900	Descending	20180804–20181013	70	-176
ALOS-2	151/700	Ascending	20181108–20190117	70	-88
ALOS-2	151/700	Ascending	20190117–20190228	42	39

3.5 Results

3.5.1 Morphological and material features

During the field investigation, we found that the morphological structure and material constitution vary significantly among different lobes and different parts of Lobe No.4 as well. For instance, Lobe No.4 has a terminal talus as steep as around 40 °based on the UAV survey (Figure 3.2b, c), while the frontal slope angles of the other two lobes are gentle (< 25 °). In addition, the transverse profile of Lobe No.4 shows a convex morphology (Figure 3.2a). No surface topography of furrows and ridges were observed during the fieldwork or evident in the UAV DOM.

The surface of Lobe No.4 is covered by debris of contrasting sizes. About 50 percent of the surface materials are boulders ranging from 20 cm up to 2 m in length, while the other part of the lobe surface consists of pebbles smaller than 20 cm in diameter and filled with soil matrix (Figure 3.3a, b). We excavated two test pits (Figure 3.3d, e) and obtained the soil moisture (volumetric water content) of two consecutive profiles in the active layer ranging between 11.7% to 26.2% (Table 3.3).

Vegetation is sparse on the moving slopes. The major species of the plants, as identified by Harris et al. (1998), *Saussurea* spp, develops an elongated root and tilts towards the downslope direction in some cases, indicating a velocity contrast between the uppermost layer of the slope and the materials centimeters below (Figure 3.3c). At least two seepage zones were found during the 2019 excursion. Surface water was flowing along the shallow and

narrow gullies carved into the lobe and disappeared at short distance downslope into the surface debris (Figure 3.2a).

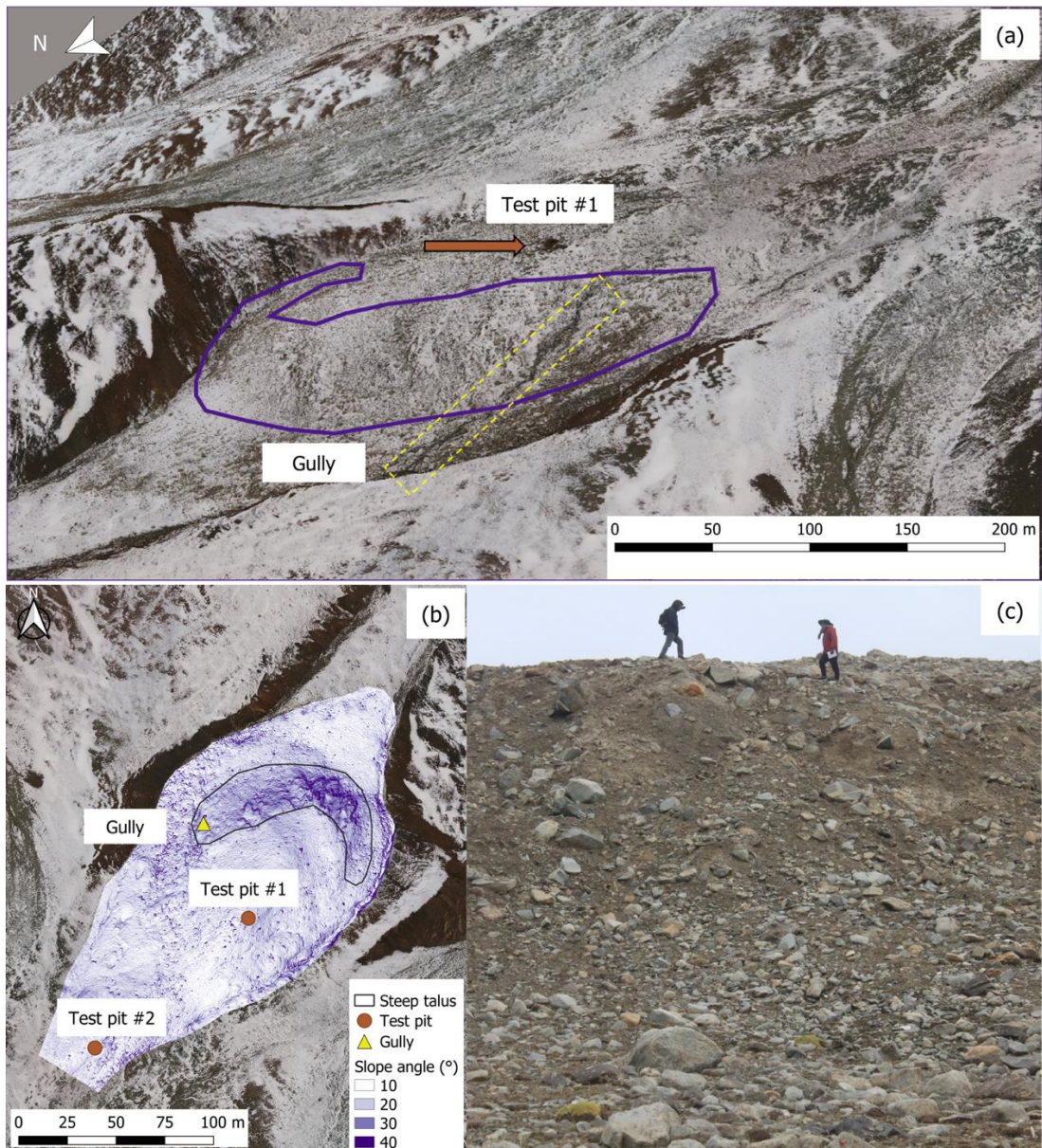


Figure 3.2 Images showing the characteristic morphology of Lobe No.4. (a) The 3D surface model of the frontal part of Lobe No.4 reconstructed from the UAV survey. The purple polygon outlines the occurrence of the over-steepened front. The yellow dashed box denotes the location of a gully shaped by surface running water. The brown arrow marks the location of Test Pit #1. (b) Slope map of the frontal part of Lobe No.4, calculated from the UAV-derived DEM. The black polygon outlines the steepest part of the frontal talus, whose slope angle reaches a maximum of 40 degrees. the background image is the DOM generated from UAV photos. (c) A field photo showing the over-steepened frontal talus of Lobe No.4.

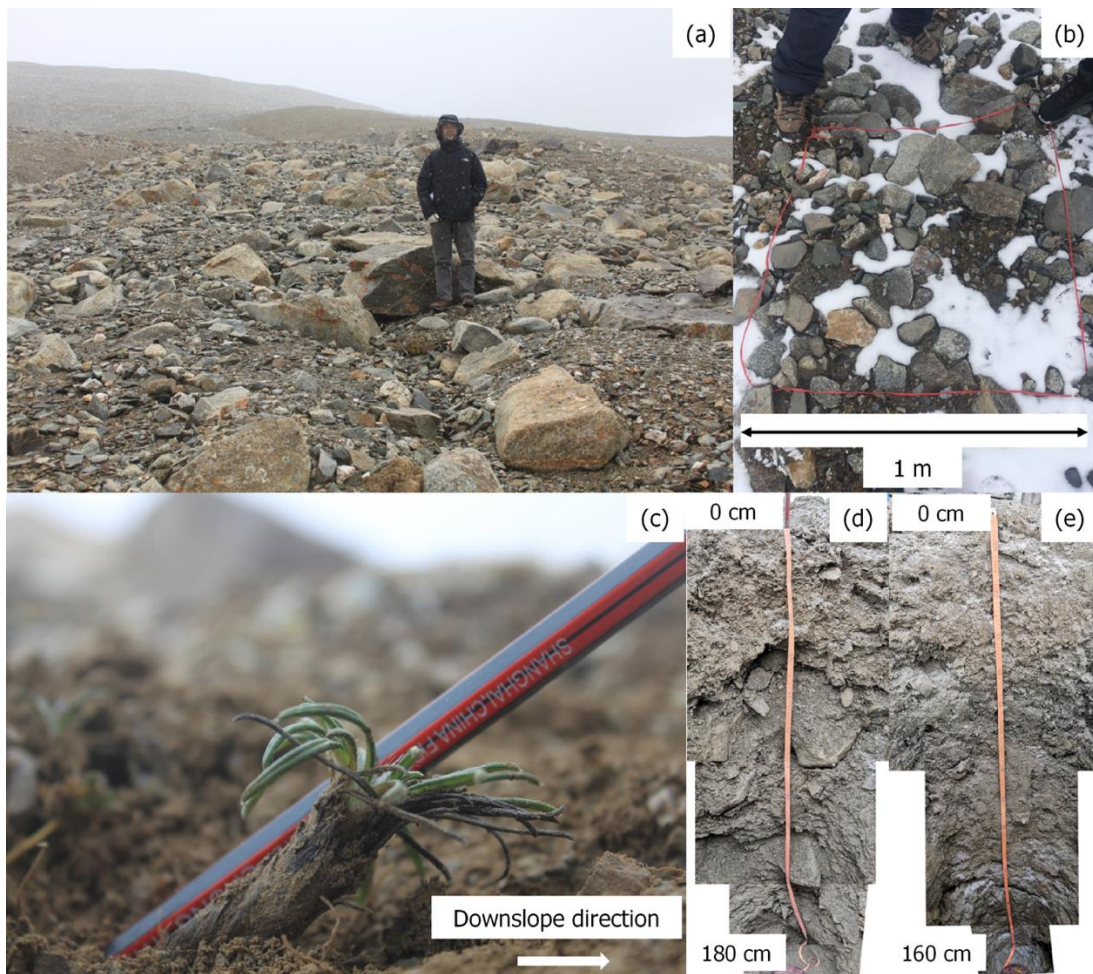


Figure 3.3 Field photos showing the material characteristics of Lobe No.4. (a) and (b) show the varying grain sizes of surface debris. (c): A plant displays a tilted form towards the downslope direction. (d) and (e) show the profiles of the two test pits we excavated on Lobe No.4. The sediments are mainly sandy soils in yellow-grey color forming a uniform soil stratum. Pebbles of various sizes (2–20 cm in diameter) occur randomly as included debris throughout the profiles.

Table 3.3 Volumetric water contents of the soil samples collected from the two test pits.

Pit #	Depth (cm)	Soil moisture (%)
01	0-20	14.9%
	20-40	15.3%
	40-60	12.4%
	60-80	21.0%
	80-100	14.9%
	100-120	13.4%
	120-140	11.7%
	140-160	13.5%
02	160-180	26.2%
	0-20	15.0%
	20-40	16.6%
	40-60	17.7%
	60-80	19.7%
	80-100	19.8%
	100-120	20.2%
	120-140	19.9%
	140-160	17.5%

3.5.2 Kinematic characteristics

Figure 3.4 shows the surface displacements along the SAR satellite LOS over two periods. We observe that during the three summer months in 2009, all the 17 lobes showed uniform deformation ranging as large as 20 cm and distributed over the entire slope surfaces despite their varying lobe aspects. However, the lobes became nearly stagnant during winter. Additionally, the interferograms reveal that the eastern slope was as active as the lobes during summer; while during winter, it turned to be inactive as well.

Moreover, we estimated the maximum surface velocity introduced by the solifluction process based on Equation 3.2 using the measured soil moisture from the two test pits. Assuming the materials consisting of the entire sample profiles are involved in the solifluction process due to the annual freeze and thaw cycle, the maximum downslope movement occurring during the thaw season is smaller than 3.6 cm.

We categorized the lobes into the NE- and NW-facing groups according to their slope aspect. We then converted the LOS displacements of the NE- and NW-facing lobes to downslope velocities based on Equation 3.3 using the interferograms generated from ascending and descending orbital paths, respectively (Figure 3.5). The lobes can differ from each other

considerably in terms of the magnitude and spatial distribution of the downslope velocities on the surface of each lobe over the same period during summer. For instance, as shown in Figure 5a, from 21st July to 29th September 2016, the NE-facing lobes range in median velocity from 10.6 cm yr⁻¹ (Lobe No.3) to 55.4 cm yr⁻¹ (Lobe No.7), and their estimated uncertainties are 7.7 cm yr⁻¹ and 10.3 cm yr⁻¹, respectively; the standard deviation of velocity represents the spatial variation and ranges from 7.3 cm yr⁻¹ (Lobe No.4) to 22.5 cm yr⁻¹ (Lobe No.7). For the NW-facing lobes, the differences are less significant as their velocities were measured during less active periods (Figure 3.5b). Nonetheless, the lobes in both groups demonstrate a consistent pattern of seasonal kinematic variations: each lobe moved at a faster rate from May to October and gradually slowed down until winter to early spring.

Figure 3.6 presents a series of downslope velocity maps of lobe No.4, which together highlight the spatial and temporal variations of kinematic behaviors and confirm the above observations. During the active season, the maximum downslope velocity of Lobe No.4 varies between 36.8 ± 8.1 cm yr⁻¹ and 94.8 ± 14.3 cm yr⁻¹. The fastest movement occurred in the summer of 2009. The two interferograms generated from the images acquired during the inactive season, namely 20080201–20080318 and 20190117–20190228, record the dormant behavior of Lobe No.4 (Table 3.4).

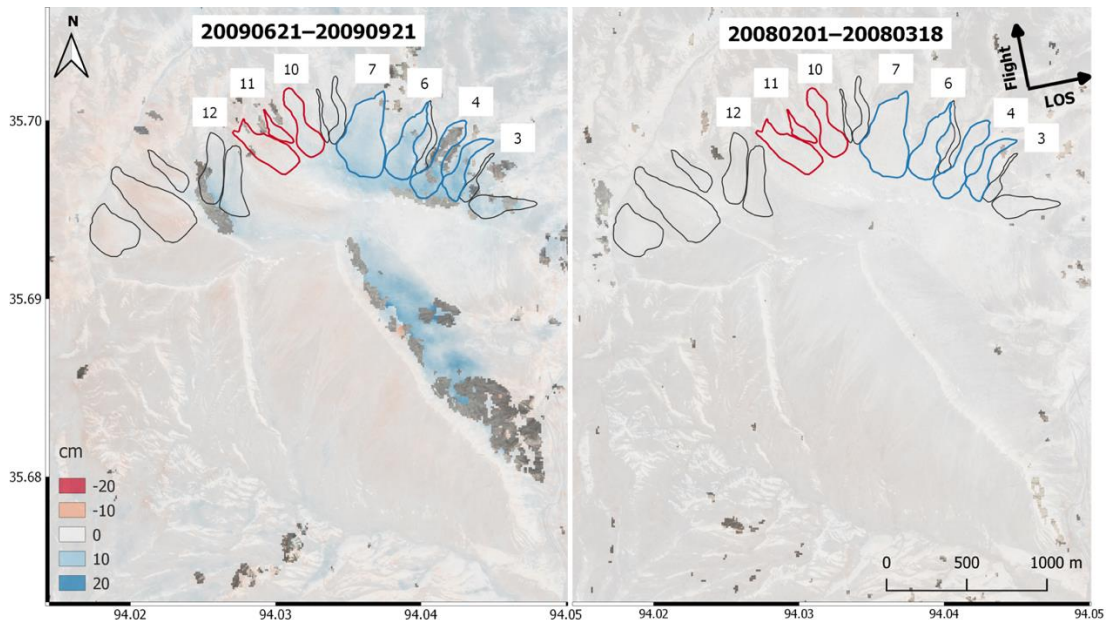


Figure 3.4 InSAR-measured LOS displacements of the landforms near Jingxian Valley during summer (left) and winter (right). Positive LOS displacement colored in blue indicates movement occurring in the same direction as the LOS vector, while negative signal mapped in red represents displacement to the opposite of LOS direction. The displacement during June to September 2009 is the stacked deformation of two interferograms generated by ALOS-1 PALSAR images (path 491/frame 700). The blue polygons outline the selected NE-facing lobes and the red polygons mark the NW-facing lobes with high data quality. The selected lobes are labeled with their corresponding lobe numbers.

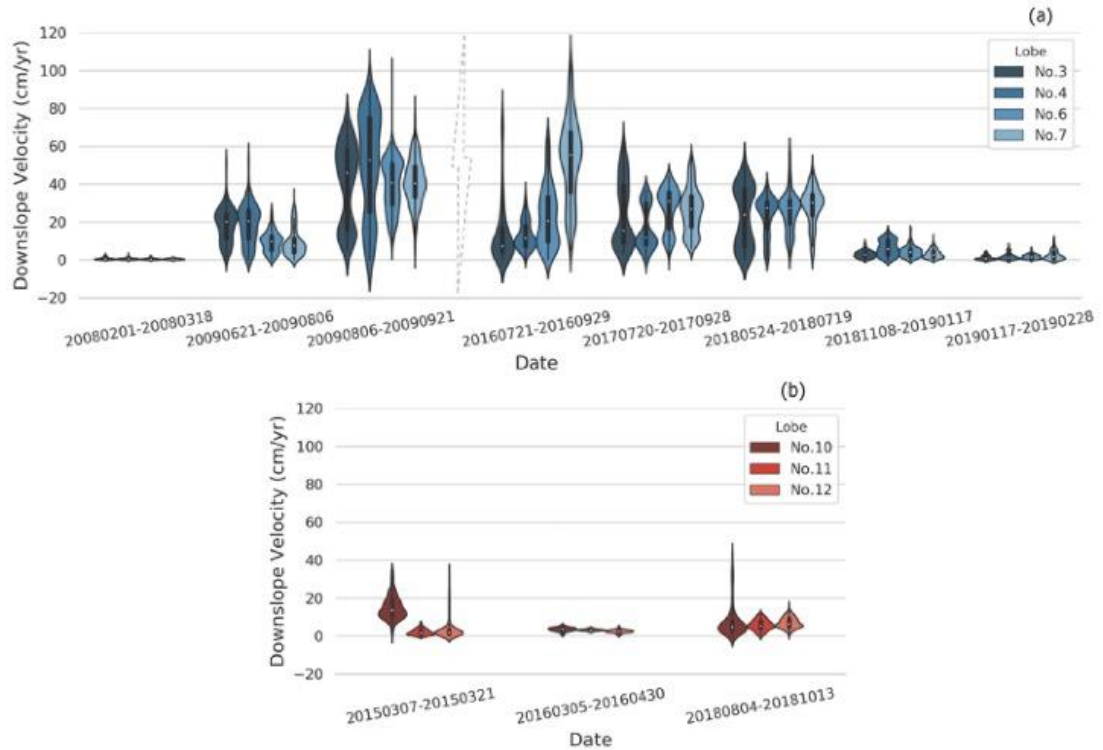


Figure 3.5 Violin plots showing the downslope velocity distributions and variations of the (a) NE-facing lobes and (b) NW-facing lobes. The box plots inside the violins display the parameters of the statistical distribution of the downslope velocity in each lobe, such as the white circle denoting the median velocity, the boundaries of the box showing the upper and lower quantiles, and the whiskers marking the maximum and minimum velocities.

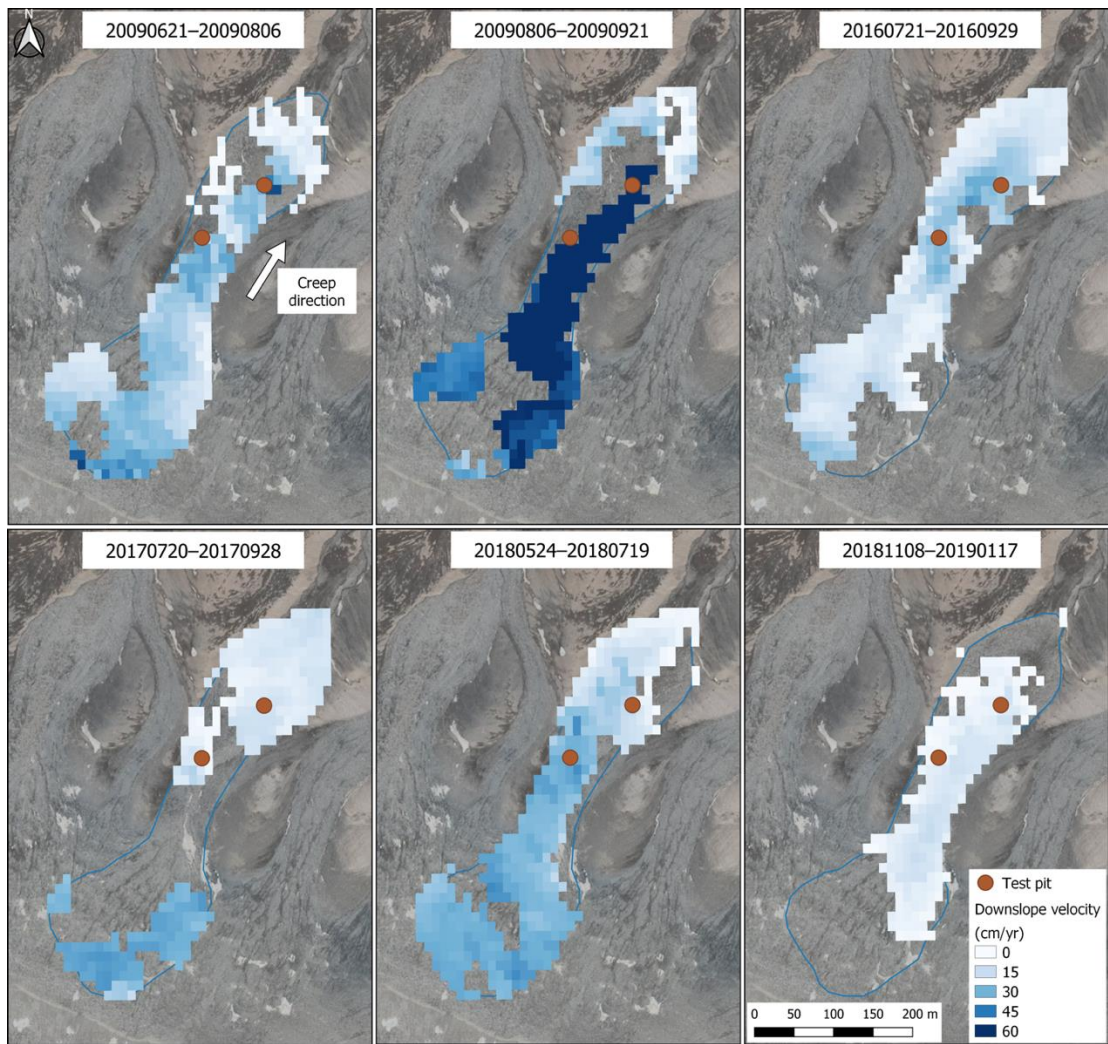


Figure 3.6 Velocity maps of Lobe No.4 showing the temporal and spatial variations of the downslope velocities. The brown circles mark the locations of the two test pits.

Table 3.4 The maximum (V_{\max}), median (V_{med}) downslope velocities and their associated uncertainties, and the standard deviation (STD) of the downslope velocities of Lobe No.4 during different periods.

Date	V_{\max} (cm yr^{-1})	V_{med} (cm yr^{-1})	STD (cm yr^{-1})
20080201–20080318	3.3 ± 2.7	0.5 ± 2.6	0.5
20090621–20090806	55.3 ± 9.9	20.6 ± 8.6	10.6
20090806–20090921	94.8 ± 14.3	52.8 ± 9.7	26.3
20160721–20160929	36.8 ± 8.1	11.3 ± 4.6	7.3
20170720–20170928	37.2 ± 6.8	11.8 ± 2.8	11.3
20180524–20180719	40.2 ± 10.1	27.4 ± 6.2	9.9
20181108–20190117	15.2 ± 3.4	5.8 ± 3.6	4.1
20190117–20190228	7.5 ± 9.2	1.3 ± 1.7	1.6

3.6 Discussion

Previous arguments over whether the landforms are rock glaciers or gelifluction deposits have been developed based on a series of field investigations in the last century, which only documented the surface movement at a few selected points and geomorphological information at Lobe No.4 (Cui, 1981; 1985; Harris et al., 1998). In this study, we systematically characterized the kinematic behaviors and geomorphological features of the lobes with a focus on Lobe No.4 based on both in-situ and remote sensing observations. We will discuss the geomorphological classification of the landforms in the perspectives of both geomorphological and kinematic approaches.

3.6.1 Geomorphological approach

Lobe No.4 has a large overall dimension, with a length of 575 m and a frontal height of 13 m. The large-scale morphology is hardly found in gelifluction-related landforms (Table 3.1), thus the lobes were previously considered as exceptionally giant gelifluction deposits or solifluction lobes (Harris et al., 1998). The other lobes display similar dimensions, yet we lack field observations of their detailed geomorphological features. An over-steepened front at the terminus of Lobe No.4 draws a convex morphology perpendicular to the downslope direction, which is considered to be a typical feature of active rock glaciers (Delaloye and Echelard, 2020). The surface debris of Lobe No.4 consists of both boulders and pebbles filled with soil matrix, possessing both the characteristics of the materials covering bouldery rock glaciers and pebbly rock glaciers (Emmert and Kneisel, 2017; Ikeda and Matsuoka, 2006).

Though being consistent with a rock glacier hypothesis, the above geomorphological features of Lobe No.4 are insufficient for us to identify it as a rock glacier. Moreover, we have observed surface features indicating the occurrence of the gelifluction processes, such as the surface runoffs and the elongation of plant roots. Gelifluction processes of the fine-grained deposits covering the slope can smooth out the surface of the landform and presumably lead to the lack of the occasionally observed surface texture of rock glaciers such as transverse furrows and ridges caused by a compressive flow (Harris, 1994; Ikeda and Matsuoka, 2006).

3.6.2 Kinematic approach

The kinematic information of the lobes has been derived from InSAR measurements. InSAR, in principle, is capable of detecting relatively small and systematic surface movement, which means that during the interval of the two SAR acquisitions, the surface scattering elements should move as a whole for a distance shorter than a few wavelengths of radar waves (one wavelength is about 24 cm for the L-band PALSAR and PALSAR-2), and remain constant relative positions within one pixel. Moreover, as an indicator of the high-quality interferogram,

high coherence implies that the ground movement tends to be continuous across more image pixels than those being taken into account to calculate the coherence (Woodhouse, 2006). If the ground movement appears to be local or heterogeneous, it cannot be well captured by InSAR. Therefore, according to the typical extent of kinematic behaviors of the different processes (Table 3.1), the large-scale and uniform movement recorded in our InSAR results reflects either the permafrost creep process and/or the frost creep due to the annual freeze-thaw action (Rouyet et al., 2019). Gelifluction movement induced by porewater saturation is likely to exist locally yet can hardly be revealed by InSAR observations.

Different dynamical processes also display different characteristics in the consequent surface velocities of the landforms (Table 3.1). The largest accumulated LOS displacement we measured by InSAR is around 20 cm for 92 days in the summer of 2009 (Figure 3.4). The annual movement associated with solifluction processes is affected by a series of environmental and topographical parameters, such as temperature, soil moisture and slope inclination, and is usually in the order of a few centimeters. In Jingxian Valley, the MAAT is -3.7 °C, which is in the range where the movement often exceeds 10 cm yr^{-1} based on previous observations of solifluction rate in various climatic conditions (Matsuoka, 2001). However, the relatively high surface velocities are mostly triggered by frequent diurnal frost which dominates surface movement of the slopes locating on subtropical high mountains or in seasonally frozen ground zone (Ballantyne, 2018). Moreover, the theoretical maximum of surface velocity can be quantified given the parameters of soil properties, depth of movement and slope topography (Section 3.4.1). As reported in Section 3.5.2, the solifluction-associated displacement occurring on Lobe No.4 is 3.6 cm, much smaller than what we have observed from the interferograms. Therefore, the widespread and relatively fast movement detected by InSAR in our results suggests the permafrost creep process instead of the solifluction process.

As regards the timing of the kinematic behaviors (Table 3.1), the observed downslope velocities of the lobes show a distinct seasonality: the active phase was from May to October and the deceleration period started in early winter followed by the inactive phase in early spring. The active phase overlapped with the period of rapid precipitation change and high precipitation accumulation (Figure 3.7). This phenomenon is consistent with the characteristics of the seasonal changes in rock glacier creep. The onset of the thawing process triggers the downslope movement of the surface materials, which only lasts for several days, and the soils uplift perpendicular to the slope during the first few days of the freezing season (Matsuoka, 1998a, 1998b). Annual frost creep dominates the short-term downslope movement, and gelifluction process operates concurrently as local and heterogeneous events. However, we have observed the occurrence of downslope motion during the frozen season of 2018 (Figure 3.7). Meanwhile, no abrupt acceleration has been detected during the thawing season

of 2016, which rejects the hypothesis that the observed seasonal rhythm is controlled by the annual frost creep or gelifluction process. In addition, our study area experiences diurnal freeze and thaw action during February to April and October to December (Yang et al., 2007), which could contribute to the small displacement detected during the two periods.

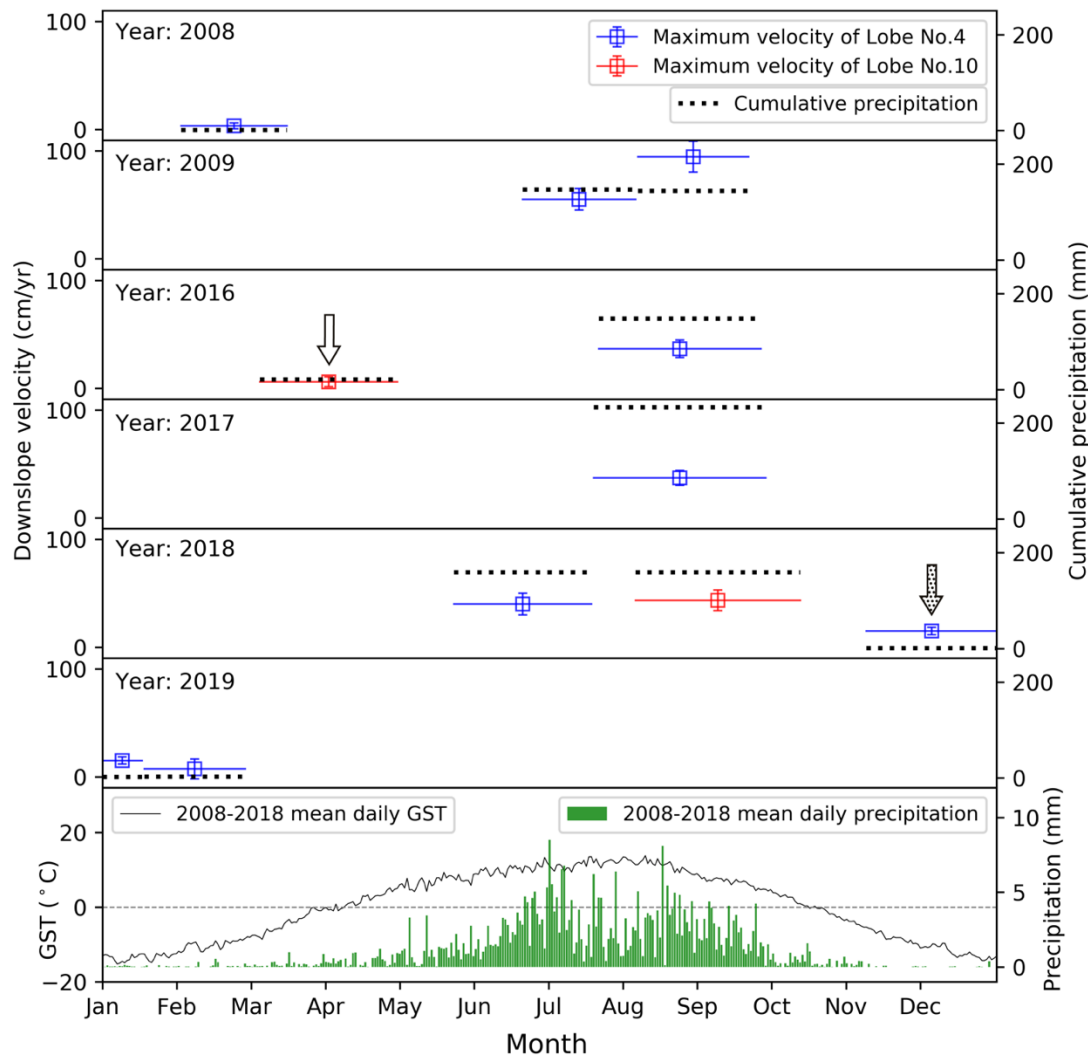


Figure 3.7 Temporal variations of the cumulative precipitation, and the downslope velocities of Lobes No.4 and No.10. The blue and red box plots show the maximum downslope velocities and their uncertainties of the NE-facing Lobe No.4 and the NW-facing Lobe No.10, respectively. The dotted line shows the cumulative amount of precipitation during each period. The blank arrow denotes one period during the thawing season of 2016, and the dotted arrow marks the one period during the frozen season of 2018. The bottom panel plots the mean daily ground surface temperature (GST) and the mean daily precipitation during 2008–2018 at the nearest meteorological station in Wudaoliang ($N35.2167^{\circ}$, $E93.0833^{\circ}$). The meteorological station is situated at 4622 m a.s.l., 100 km southwest to the region of interest. (Data source: China Meteorological Administration, <http://data.cma.cn/>).

3.6.3 Geomorphological classification of the landforms

We have so far analyzed the data using both geomorphological and kinematic approaches. Although the kinematic information can provide insight into the ongoing processes that shape the landforms, the geomorphological classification of a landform should be identified mainly on the basis of geomorphological characteristics. Accordingly, the lobes, in spite of presenting consistent kinematic features, are challenging to enable a reliable geomorphological identification, let alone the eastern slope which lacks any morphological observations. Lobe No.4 is the appropriate study object to investigate its geomorphological classification.

Lobe No.4 develops a steep talus at the terminus and shows a convex morphology in the direction perpendicular to the creep. The frontal part of the lobe is delimited by the lateral margins, which become indiscernible at the rooting zone of the lobe. These features fulfill the primary geomorphological criteria for rock glaciers (Delaloye and Echelard, 2020). The evolution of the lobe is dominantly driven by the creep of permafrost, while surface features such as the plant elongation and water flow imply the occurrence of the gelifluction process locally. One unique environmental feature of the previously proposed “Kunlun-type” rock glacier is the absence of a headwall which is commonly connected to rock glaciers and may serve as a debris source for the downslope rock glacier unit (Cui, 1981, 1985). Lobe No.4, however, is spatially connected to a debris-mantled-slope, from which materials forming the lobe are transported. The upslope unit connected to a rock glacier may vary, such as a talus, landslide, and glacier, etc. Recognizing the upslope’s different unit types usually helps to reveal the genetic characteristics of a rock glacier (Delaloye and Echelard, 2020). Therefore, considering the unique geomorphological settings, we suggest that Lobe No.4 is a debris-mantled-slope-connected rock glacier: the debris are derived from the in-situ weathering process constituting the upslope debris-mantled unit, and progressively transported downslope to finally develop into a rock glacier.

3.7 Conclusions

We investigated the geomorphological classification of a group of periglacial landforms near Jingxian Valley in the East Kunlun Mountains using a combination of geomorphological and kinematic approaches and arrived at the following conclusions:

- (1) Uniform and large-scale motion across the surface of the 17 tongue-shaped landforms have been detected with InSAR, which reflects the creep process of the underlying permafrost. A similar process tends to operate in the eastern slope as well.
- (2) The movement rate of the lobes changes seasonally. In summer, the downslope velocity reaches up to 100 cm yr^{-1} . In winter, the lobes are nearly inactive.

CHAPTER 3. RESEARCH QUESTION I

- (3) The active period of the lobes is from May to October, which overlaps with the period of rapid precipitation change and high precipitation accumulation.
- (4) There is no abrupt transition of the kinematic status of the lobes being observed during the onset of the ground surface thawing/freezing event.
- (5) Lobe No. 4 has a talus-like over-steepened front at the terminus, with an average slope angle of about 35° , the cross-section perpendicular to the creep direction is arched and convex. The surface debris consists of both large boulders and fine-grain pebbles. Based on the morphological and material characteristics, we identify Lobe No. 4 as a debris-mantled-slope-connected rock glacier, the surface of which has undergone small-scale gelifluction process locally.

This study demonstrates the effectiveness of understanding the geomorphology of periglacial landforms comprehensively by characterizing and interpreting the kinematic behaviors with InSAR. The kinematic and morphometric quantifications obtained by remote sensing methods address the long-disputed question of geomorphological classification of the unique landforms at Kunlun Pass, and illustrate the diversity and intricacy of rock glaciers and related landforms from the perspectives of both geomorphology and dynamics.

Chapter 4 Inventorying rock glaciers in the arid West Kunlun of China using SAR interferometry and deep learning

"I wisely started with a map."

—J. R. R. Tolkien

Rock glaciers manifest the creep of mountain permafrost occurring in the past or at present. Their presence and dynamics are important indicators of permafrost distribution and changes in response to climate forcing. However, knowledge of rock glaciers is completely lacking in the West Kunlun, one of the driest mountain ranges in Asia, where widespread permafrost is rapidly warming. In this study, we first mapped and quantified the kinematics of active rock glaciers based on satellite Interferometric Synthetic Aperture Radar (InSAR) and Google Earth images. Then we trained DeepLabv3+, a deep learning network for semantic image segmentation, to automate the mapping task. The well-trained model was applied for a region-wide, extensive delineation of rock glaciers from Sentinel-2 images to inventory the landforms that were previously missed in the InSAR-based identification. Finally, we inventoried 413 rock glaciers across the West Kunlun: 290 of them were active rock glaciers mapped manually based on InSAR and 123 of them were outlined by deep learning. The inventory also classifies the rock glaciers by their spatial connection to the upslope units into four types, namely the glacier-connected (total number: 202), the debris-mantled slope-connected (143), the glacier forefield-connected (41), and the talus-connected (27). All the rock glaciers are located at altitudes between 3389 m and 5541 m with an average size of 0.26 km² and a mean slope angle of 17 °. The mean and maximum surface downslope velocities of the active ones are 24 cm yr⁻¹ and 127 cm yr⁻¹, respectively. Characteristics of the inventoried rock glaciers hold implications on the interactions between glacial and periglacial processes in the West Kunlun. The method of combining InSAR and deep learning proves to be effective for compiling rock glacier inventories with kinematic information over a significant extent of cold regions, e.g., the Tibetan Plateau, which provides a baseline dataset and allows the monitoring of rock glaciers as indicators of permafrost state and potential water sources in a changing climate.

4.1 Introduction

Rock glaciers are debris-ice landforms widely distributed in the mountainous periglacial environment globally (Ballantyne, 2018). Rock glaciers have drawn a lot of research interest since their first identification at the beginning of the 20th century (Capps, 1910), because they serve as important indicators for alpine permafrost which is defined by its underground temperature and invisible in most other cases (Barsch, 1996). Inventorying rock glaciers is therefore motivated by producing baseline knowledge for addressing various scientific

questions associated with alpine permafrost, which has been warming and undergoing degradation (Biskaborn et al., 2019). Several studies have revealed that multi-annual acceleration of rock glaciers is synchronous with the rise of air and ground temperatures (Delaloye et al., 2010; Delaloye et al., 2013; Haeberli et al., 2006; Marcer et al., 2021; Sorg et al., 2015), and their short-term velocity variation is sensitive to the input of unfrozen water (Cicoira et al., 2019b; Ikeda et al., 2008; Kenner et al., 2019; Müller et al., 2016; Wirz et al., 2016b). Hence rock glacier inventories are valuable databases for studying how climatic factors cause permafrost changes manifesting in landform kinematics which can be quantified continuously and remotely. Moreover, rock glaciers contain massive amounts of ground ice and contribute significantly to hydrological systems in some catchments (Azócar and Brenning, 2010; Geiger et al., 2018; Jones et al., 2018a; Jones et al., 2021; Millar et al., 2013; Schaffer et al., 2019). A comprehensive inventory of rock glaciers lays the foundation for estimating the potential water storage and evaluating their future role in maintaining water supplies.

Numerous efforts have been put into inventorying rock glaciers in various mountain ranges worldwide in the past several decades, such as in Central Europe (Chueca, 1992; Guglielmin and Smiraglia, 1998; Onaca et al., 2017; Roer and Nyenhuis, 2007; Scotti et al., 2013), South America (Brenning, 2005a; Falaschi et al., 2014; Rangecroft et al., 2014; Villarroel et al., 2018), and North America (Ellis and Calkin, 1979; Janke, 2007; Liu et al., 2013; Millar and Westfall, 2008). Rock glaciers are abundant in the mountainous western China where a vast area of alpine permafrost is underlying and undergoing accelerated degradation in response to the warming climate (Cheng et al., 2019; Ni et al., 2020; Yang et al., 2010; Yang et al., 2019; Yao et al., 2019; Zhao and Sheng, 2019). However, few regional-scale inventories of rock glaciers have been compiled until recently (Ran and Liu, 2018; Schmid et al., 2015; Wang et al., 2017), which hinders rock glaciers functioning as a permafrost indicator. Such lack of knowledge is attributed to the following reasons: (1) rock glaciers in western China are mostly situated in remote and harsh environment where early *in situ* investigations are scarce and limited to case studies or small catchment-scale research (Cui, 1985; Cui and Zhu, 1988; Harris et al., 1998; Li and Yao, 1987; Liu et al., 1995; Zhu et al., 1992); (2) mapping rock glaciers conventionally relies on manually detecting and outlining the landforms from optical images (Schmid et al., 2015), which is labor-intensive to apply to large permafrost region (e.g., West Kunlun Mountains) following an exhaustive strategy; (3) controversial opinions of identifying rock glaciers exist due to the complexity of the landforms (Berthling, 2011; Harris et al., 1998; Hu et al., 2021), which makes it more challenging to map rock glaciers.

To address these problems, recent research progress in compiling rock glacier inventories includes (1) integrating InSAR techniques to facilitate active rock glacier identification and kinematics quantification (Barboux et al., 2014; Liu et al., 2013; Wang et al., 2017); (2)

implementing Convolutional Neural Networks (CNN) and object-based image analysis to automate rock glacier delineation (Robson et al., 2020); and (3) establishing widely accepted inventorying guidelines by the international rock glacier research community (Delaloye and Echelard, 2020).

Here we combine the InSAR technique and the state-of-the-art deep learning network, i.e., DeepLabv3+ (Chen et al., 2018), to produce the first rock glacier inventory covering the region of West Kunlun Mountains of China, one of the driest mountain ranges in Asia, where widespread permafrost is warming (Cheng et al., 2019; Li, 1986), and knowledge of rock glaciers is completely lacking. Advantage of the combined methodology is twofold: the InSAR-based mapping approach provides essential information of surface kinematics and accurate manual delineation for training the deep learning model, meanwhile the automated method improves mapping efficiency and more importantly, overcomes the conservativity of the former approach, as some rock glaciers cannot be detected by InSAR due to coherence loss in interferogram, geometric distortions, their topographic orientations insensitive to InSAR line-of-sight measurements, or simply their inactive kinematic status (Robson et al., 2020; Wang et al., 2017). Manual delineation of rock glaciers based on InSAR and high-resolution optical imagery in this study is guided by the baseline concepts proposed by the International Permafrost Association (IPA) Action Group on rock glaciers to ensure a standard high-quality dataset utilized to train the deep learning network, and thus, the final inventorying results (Delaloye and Echelard, 2020).

This study aims to develop an automated approach to compile a standard rock glacier inventory on a regional scale in western China, i.e., the West Kunlun Mountains. We demonstrate the effectiveness of using a deep-learning-based method to delineate rock glaciers efficiently and accurately. We provide essential attributes to the inventoried landforms according to the inventorying guidelines. We also conduct statistical analyses to summarize the spatial distribution and geomorphologic characteristics of the inventoried rock glaciers. The compiled inventory will serve as a baseline dataset for conducting long-term studies of rock glaciers and permafrost in a changing climate.

4.2 Study area

The West Kunlun is a major mountain range situated in the northwest of Tibetan Plateau, extending ~800 km from the eastern margin of Pamir Plateau to the Keriya Pass of Kunlun Mountains, with a total study area of ~124000 km² (74–81.5 °E, 35–39.5 °N) (Figure 4.1). Elevation of the study region ranges between 3000 m and 7500 m. Cold desert climate (Köppen climate classification BWk) is dominant in the West Kunlun mountains (Peel et al., 2007): mean annual air temperature (MAAT) and mean annual accumulated precipitation are

4.2 °C and 51 mm, respectively, as revealed by the record of the nearest meteorological station in Tashikurgan (75.23 °E, 37.77 °N; 3,090 m a.s.l.) during 1957–2017 (data source: China Meteorological Administration, <http://data.cma.cn/>). In the high-altitude region, such as near the snowline altitude (5800–6000 m) of the West Kunlun, the MAAT is estimated to be -13.2–-14.6 °C, with a temperature average in summer (June to August) being -1.5– -2.1 °C (Shi, 2006).

The easternmost part of the study region is overlapped with the West Kunlun permafrost survey area (78.8–81.4 °E, 34.5–36.0 °N; 4200–6100 m a.s.l.) established by the Cryosphere Research Station (CRS) on the Qinghai-Tibet Plateau, Chinese Academy of Sciences. In situ investigations have found that the mean air temperature in January ranges from -17 °C to -15 °C and the mean annual cumulative precipitation is ~30 mm in the survey region since 2009 (Zhao and Sheng, 2019). Vegetation is sparse due to the extremely dry conditions and thus the distribution of which is significantly affected by the local hydrological and topo-climatic environment. Ice-rich permafrost is widely distributed in the survey area (Zhao et al., 2019). The mean annual ground temperature (MAGT) is higher than -2.7 °C as revealed by borehole measurements and permafrost was warming at an average rate of 0.11 °C/10 a from 2010 to 2017 (Cheng et al., 2019; Zhao and Sheng, 2019). The lowest altitudinal limit of permafrost occurrence is between 4650 m and 4800 m depending on different slope aspects according to previous comprehensive field surveys focusing on a subregion of West Kunlun (Li et al., 2012).

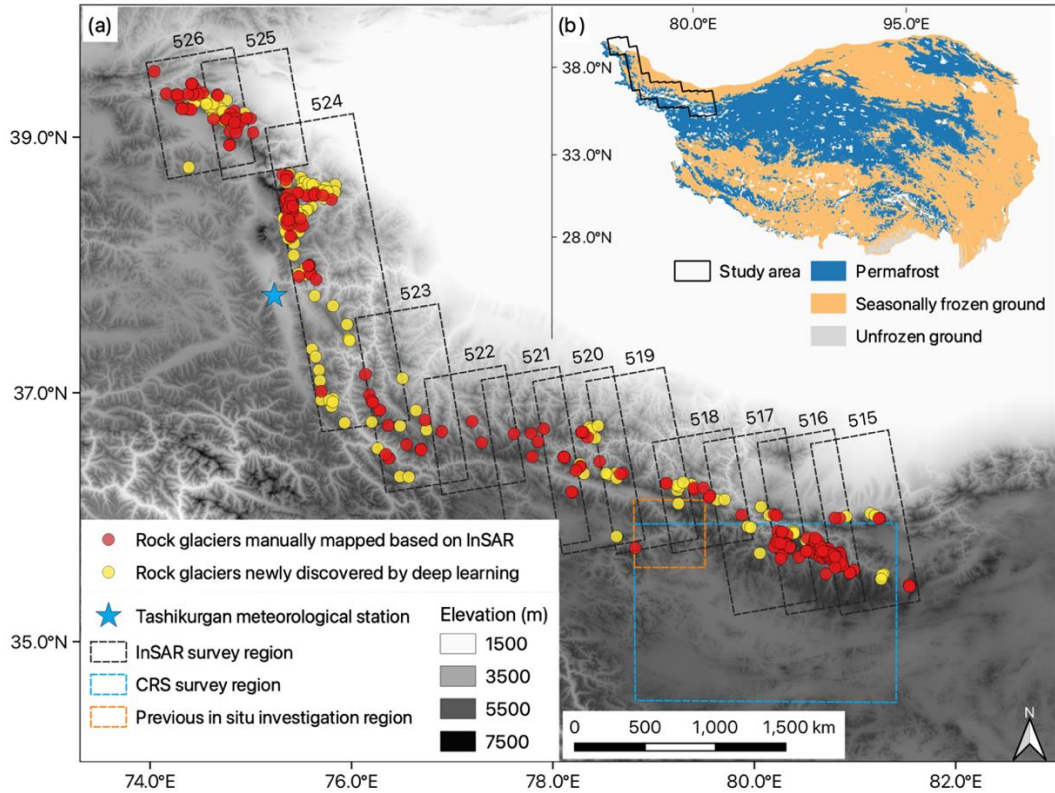


Figure 4.1 (a) Distribution of the inventoried rock glaciers in the West Kunlun. The red dots are manually mapped rock glaciers (290 in total), and the yellow dots represent newly identified rock glaciers by our deep learning method but were missed in the InSAR-based inventory (123 in total). The background is a topographical map showing the ground coverage of ALOS-1 PALSAR data used in this study (dashed black box), with the path number of each ground track labelled aside. The dashed blue and orange boxes show the extents of the CRS permafrost survey region (Zhao and Sheng, 2019), and the previous in situ investigation area (Li et al., 2012), respectively. The blue star denotes the location of the Tashikurgan meteorological station. The topography is plotted based on the 1-arcsec SRTM DEM (spatial resolution ~30 m). (b) Permafrost distribution (Zou et al., 2017) and the location of the study area on the Qinghai-Tibet Plateau.

4.3 Methodology

The method we adopted consists of two parts and is detailed below. First, we inventoried active rock glaciers manually from interferograms and Google Earth images. Second, we used the manually labelled images to train a deep learning network, i.e., DeepLabv3+, for mapping rock glaciers automatically from Sentinel-2 optical images.

4.3.1 Inventorying active rock glaciers from interferograms and Google Earth images

We mapped active rock glaciers by combining two imagery sources: interferograms and Google Earth images. The displacement maps generated by InSAR allow us to easily recognize moving parts of the ground surface, meanwhile the high-resolution and multi-temporal Google Earth images provide geomorphic information to distinguish rock glaciers from the other active surface units. Visual identification was conducted based on the geomorphological

criteria proposed by Delaloye and Echelard (2020) including the frontal and lateral margin morphology, and the surface ridge-and-furrow topography as an optional indicator. We then outlined the recognized landforms along their extended geomorphological footprints, i.e., the frontal and lateral margins are included within the boundaries.

In total, twenty-two interferograms generated from ALOS-1 PALSAR images covering the West Kunlun Mountains were used for ground movement detection during 2007–2008 (Table 4.1). To maintain high interferometric coherence and reduce topographic error, we selected image pairs with temporal spans of 46 days and perpendicular baselines smaller than 1000 m. The topographic phases were estimated and removed by using the digital elevation model (DEM) produced by the Shuttle Radar Topography Mission (SRTM) with a spatial resolution of ~30 m over most of the study region. A frame of TanDEM-X DEM (spatial resolution ~12 m) was adopted for correcting topographic phases for one interferogram overlapping with the permafrost survey region. Multi-looking operation and adaptive Goldstein filter (8×8 pixels) were applied to the interferometric processing, which was implemented by the open-source software InSAR Scientific Computing Environment (ISCE) version 2.2.0 (available at <https://github.com/isce-framework/isce2>). We then unwrapped the interferograms with the SNAPHU software (Chen and Zebker, 2002) and selected one point located at the flat and stable ground close to each rock glacier to re-reference the unwrapped phases measured within the boundary of each landform. By doing so, we managed to remove the long-wavelength orbit errors and the atmospheric artefacts including the water vapor delay and ionospheric effects, all of which can be assumed identical within the extent of a rock glacier (Hanssen, 2001).

We determined the surface downslope velocities of rock glaciers as their kinematic attributes. The surface velocities along the SAR satellite line-of-sight (LOS) direction were derived from the unwrapped interferograms and then projected to the downslope direction of each landform. Associated uncertainties including the InSAR measurements and geometric parameters were quantified through error propagation (Hu et al., 2021). We used the spatial average velocity within a rock glacier to represent its overall kinematic status. Then we refined the results by selecting data that fulfilled the following criteria: (1) after masking out the pixels with low coherence (< 0.3), the remaining pixels account for more than 40% of the entire landform extent; (2) the relative uncertainties of the spatial average velocity are lower than 20%.

Essential geomorphic attributes such as the elevation range, mean slope angle, and landform aspect were quantified using SRTM DEM. Qualitative attributes including the spatial connection of the rock glacier to the upslope unit and the activity category were described and assigned to the inventory dataset following the inventorying guideline (Delaloye and Echelard, 2020). We primarily classified the inventoried rock glaciers according to their spatial

CHAPTER 4. RESEARCH QUESTION II

connection to the upslope unit because it could provide implications regarding the landform genesis. We used the Global Land Ice Measurements from Space (GLIMS) dataset to help recognize the surrounding glacier units (GLIMS and NSIDC, 2005). Figure 4.2 presents examples of rock glaciers that were classified by their upslope units into four categories. The entire workflow is illustrated in Figure 4.3 with one example shown in Figure 4.4.

CHAPTER 4. RESEARCH QUESTION II

Table 4.1 List of interferograms generated from ALOS-1 PALSAR data.

Path/frame	Date	Perpendicular baseline (m)
515/700	20081213–20090128	300
515/710	20081213–20090128	307
516/700	20081114–20081230	-38
516/710	20081114–20081230	-31
517/700	20070829–20071014	364
517/710	20070829–20071014	370
518/710	20080317–20080502	652
519/710	20080102–20080217	972
519/720	20080102–20080217	337
520/710	20080119–20080305	581
520/720	20080119–20080305	587
521/710	20080205–20080322	62
521/720	20080205–20080322	71
522/720	20070822–20071007	212
523/720	20070608–20070724	288
523/730	20070608–20070724	289
524/730	20080210–20080327	115
524/740	20070810–20070925	108
524/750	20080210–20080327	130
524/760	20080210–20080327	137
525/770	20070712–20070827	292
526/770	20070613–20070729	471

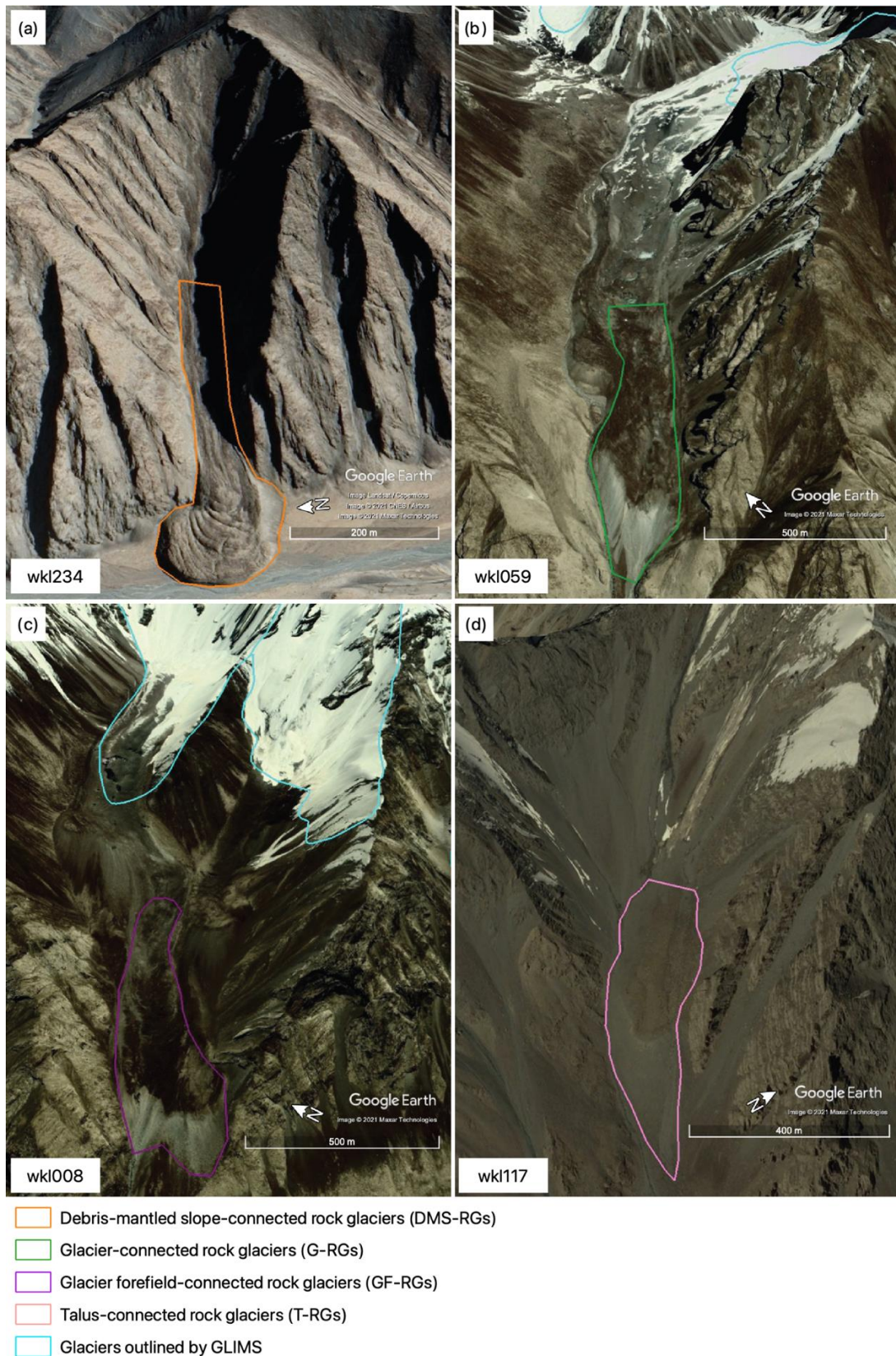


Figure 4.2 Google Earth images showing rock glaciers of four different types and their special connections to the upslope units. (a) shows a debris-mantled slope-connected rock glacier (DMS-RG) in orange (ID: wkl234). (b) focuses on a glacier-connected rock glacier (G-RG) in green (ID: wkl059). The cyan polygons are glaciers outlined by the GLIMS dataset. (c) presents a glacier forefield-connected rock glacier (GF-RG) in purple (ID: wkl008). Note that the GF-RG disconnects from the upslope glacier

in cyan, whereas the G-RG in (b) is in continuation of the upslope debris-covered glacier. (d) displays a talus-connected rock glacier in pink (ID: wkl117), from which the upslope talus can be observed.

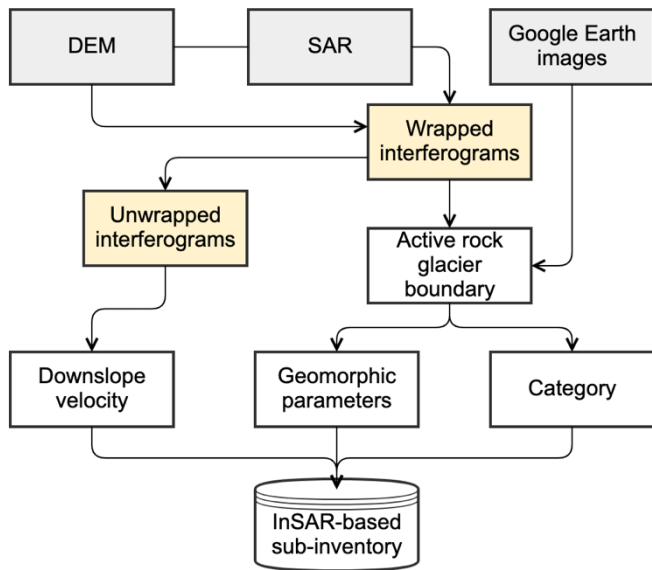


Figure 4.3 Diagram of the workflow to manually inventory active rock glaciers based on InSAR and Google Earth images.

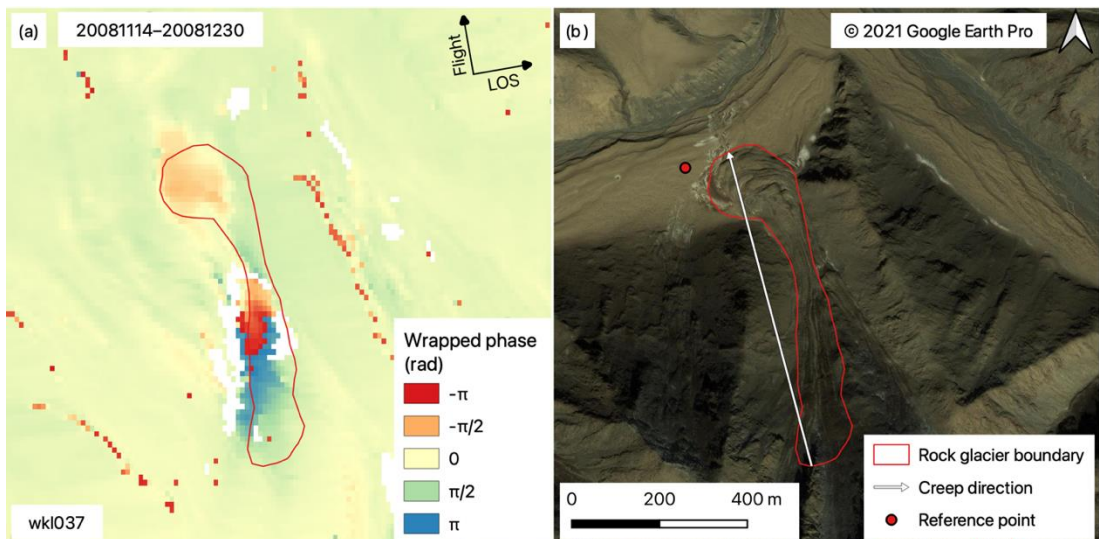


Figure 4.4 An example of identified active rock glacier (ID: wkl037). (a) shows the contrasting wrapped phases between the landform and surrounding background. The ALOS-1 PALSAR image pair generating the interferogram were acquired on 14/11/2008 and 30/12/2008. (b) is the corresponding Google Earth image presenting the geomorphic characteristics of the mapped active rock glacier. The white arrow indicates the direction of the movement, and the red dot marks the location of reference point used for phase correction. This rock glacier is debris-mantled slope-connected.

4.3.2 Automated mapping of rock glaciers using deep learning

Deep learning has proved powerful in semantic segmentation by using a convolutional neural network to progressively extract visual features at different levels from input images (LeCun et al., 2015), which is suitable for handling difficult mapping tasks as in the case of rock glaciers. Among the open-source deep learning architectures designed for semantic

segmentation, we adopted the DeepLabv3+Xception71 as the framework for us to develop the automatic mapping method (Chen et al., 2018) because of its outstanding performance demonstrated in the past PASCAL VOC tests and recent research applications to cryospheric sciences (Everingham et al., 2015; Huang et al., 2020; Zhang et al., 2021).

Development of the deep learning model for delineating rock glaciers can be divided into three major steps: (1) preparing input data, (2) training and validating deep learning network, and (3) infer and post-process results, as detailed below. Figure 4.5 illustrates the entire development workflow.

The data preparation step aimed to produce a dataset of optical images and corresponding rock glacier label images to feed into the convolutional neural network. The input optical images were cloud-free (cloud cover < 5%) Sentinel-2 images (spatial resolution ~10 m) covering the West Kunlun region acquired during July and August of 2018. We pre-processed the images by extracting the visible red, green, and blue bands and converting to 8-bit, so that the satellite images were in the same format as the training datasets used for pre-training the DeepLabv3+ network we adopted (Chen et al., 2018). To generate the label images, i.e., binary raster that have pixel values as 0 or 1, with 1 indicating rock glaciers and 0 indicating the background, we used the ESRI Shapefiles of the manually identified rock glaciers created in the InSAR-based mapping process to label the Sentinel-2 images. We removed some rock glacier samples from the dataset because they are unrecognizable due to cloud cover or relatively low resolution of the Sentinel-2 images. In addition, we delineated some negative polygons, which are similar-looking landforms such as debris-covered glaciers and solifluction slopes, and environments where no rock glaciers occur, e.g., water bodies and villages. These negative polygons were used to produce negative label images which constitute the input dataset along with the positive ones. More negative samples were included during the iterative training and validating process by adding the incorrectly inferred examples to the negative training dataset for the next experiment. We extracted the positive polygons with their surrounding background (a buffer size of 1500 m) from the optical images and cropped these sub-images into image patches of sizes no larger than 480*480 pixels. Finally, we split the whole dataset of input image patches by randomly selecting 90% of the data as the training set and the remaining 10% as the validation set.

Then we trained the DeepLabv3+Xception71 network with the initial hyper-parameters (e.g., learning rate, learning rate decay, batch size, number of iterations) suggested by Chen et al. (2018) and evaluated the model performance on the training and validation datasets, respectively. The evaluation was conducted throughout the training process by monitoring the Intersection over Union (IoU) value, which is defined as:

$$IoU = \frac{TP}{TP+FP+FN} \quad (4.1)$$

where TP (true positive), FP (false positive), and FN (false negative) are pixel-based. The mean IoU, which is calculated by averaging the IoU of each class, is commonly adopted to indicate the accuracy of semantic segmentation models. Our network classified each pixel of the optical images into two classes, namely the rock glacier and the background. As the amounts of pixels in the two classes are extremely imbalanced (the rock glacier class occupies a small portion of the images), we only used the IoU value of the rock glacier class to represent the model performance. We set 0.80 as the threshold: when the IoU value was lower than it, we increased the size of the training dataset by performing image augmentation (e.g., blurring, rotation, flip) on the positive samples and including incorrectly inferred examples to the negative samples and repeated the training and validating processes until the target IoU value was achieved.

We applied the well-trained model to map rock glaciers from Sentinel-2 images covering the West Kunlun. To refine the inference results, we excluded the predicted polygons smaller than 0.03 km² due to the limited spatial resolution of the Sentinel-2 images and the usual areal extent of rock glaciers. Then we inspected each automatically delineated landform and modified the boundaries when necessary. Finally, we determined the same set of landform attributes as the InSAR-based inventory (Section 4.3.1) and compiled the outputs produced by the two methods into one inventory.

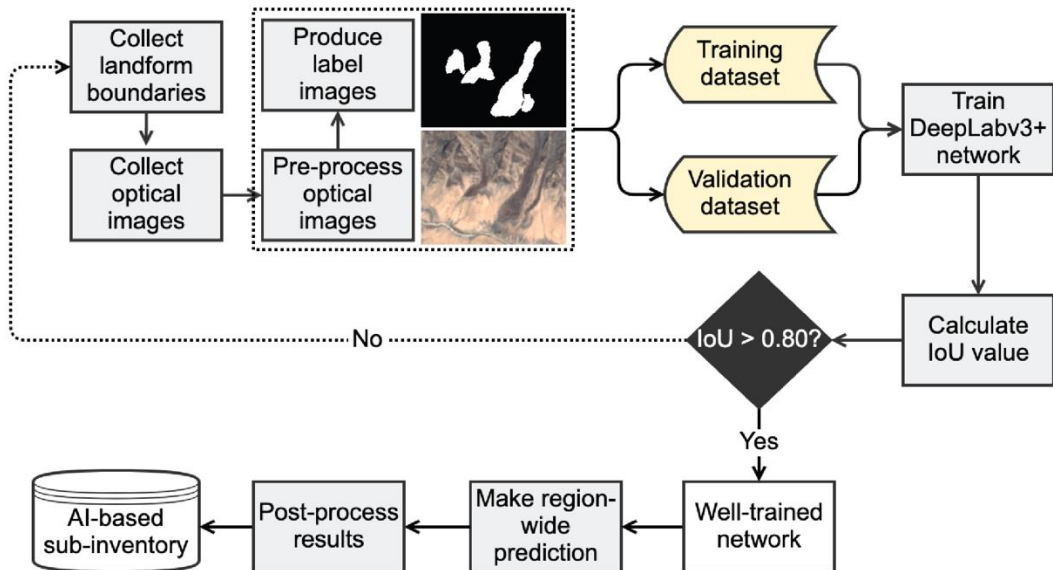


Figure 4.5 Diagram of the workflow to automatically map rock glaciers using DeepLabv3+ network. AI stands for artificial intelligence.

4.4 Results

In this section, we first present the performance of the automated mapping method. Then we analyse the features of all the inventoried rock glaciers from the geomorphological perspective. Finally, we summarize the kinematic characteristics of the active rock glaciers measured by InSAR. The locations of the mapped rock glaciers are shown in Figure 4.1.

4.4.1 Performance of the automated mapping approach

After iteratively training and improving the model (Section 4.3.2), we trained a model attaining a performance of $\text{IoU} = 0.801$ on both the training and validation datasets (Figure 4.6). The input data were derived from 172 rock glacier samples and 145 non-rock glacier samples, occupying $\sim 0.6\%$ of the total mapping area.

Over the entire West Kunlun region, our well-trained model automatically identified and delineated 337 landforms as rock glaciers, among which 123 rock glaciers were newly discovered, 49 predicted polygons were false positives, the others were true positives but already present in the InSAR-based inventory. Figure 4.7a and b present the satisfactory accuracy of automated delineation by comparing the deep learning mapped rock glaciers with the manually mapped boundaries in the training and validation datasets, respectively. The delineation accuracy was also acceptable for the newly discovered rock glaciers in general, as shown in Figure 4.7c. However, we still conducted modifications to 100 out of the 123 landforms to ensure the quality of the mapping results after manual inspection (Figure 4.7d).

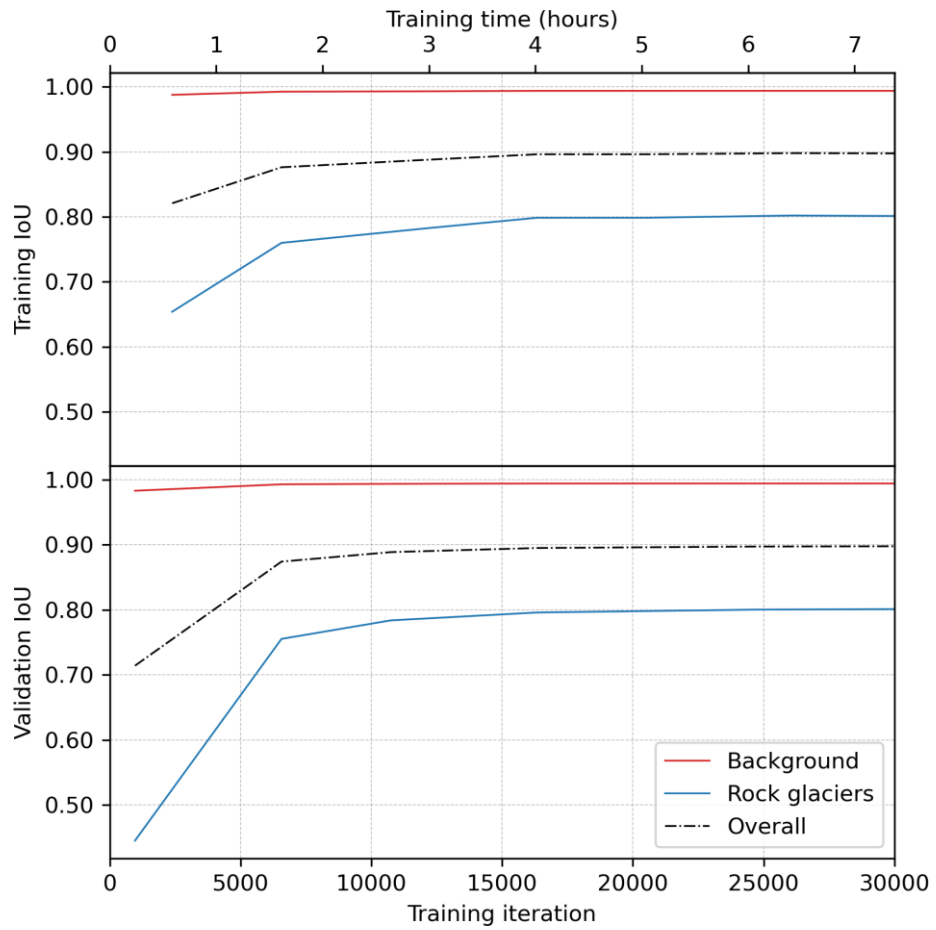


Figure 4.6 Performance of the deep learning model for recognizing rock glaciers from background on the training and validation datasets, consisting of 2007 and 223 image patches, respectively.

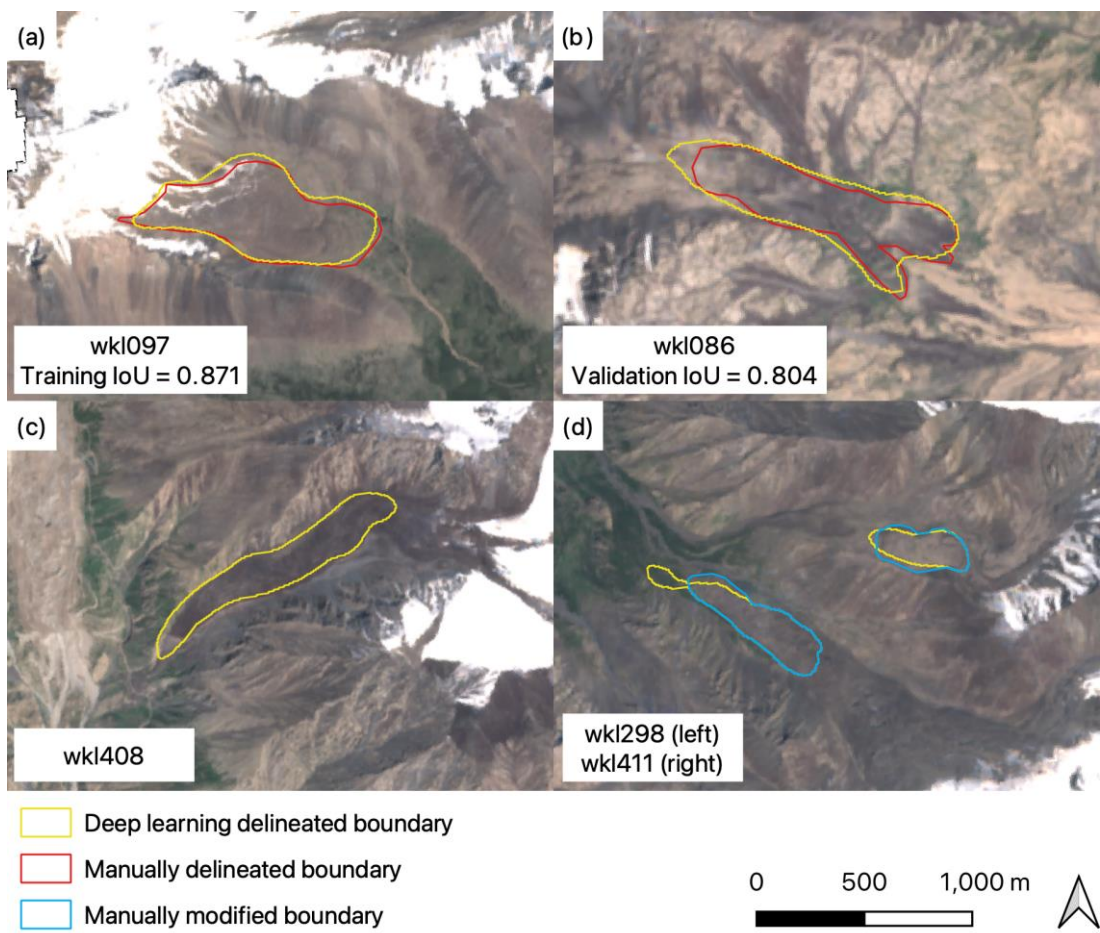


Figure 4.7 (a) Comparison of the deep learning mapped rock glacier boundary (in yellow) with the manually delineated polygon (in red) in the training dataset. The IoU between the two polygons is 0.871. (b) Similar visual comparison between the automatically outlined boundary (in yellow) and the manually mapped one (in red) in the validation dataset, with an IoU of 0.804. (c) Example of a rock glacier newly discovered by deep learning with good delineation accuracy. (d) Examples of two automatically identified and outlined rock glaciers (in yellow) that need manual modifications (in blue). The landform IDs of these examples are labelled on the figures. The background is a Sentinel-2 image acquired on 12/07/2018.

4.4.2 Geomorphic characteristics of the inventoried rock glaciers

We compiled an inventory of 413 rock glaciers across the West Kunlun Mountains: 290 of them were mapped by the conventional method based on interferograms and Google Earth images, the other 123 landforms were identified by deep learning network with supplementary modifications to the automatically delineated boundaries (Figure 4.1).

Table 4.2 presents the overall geomorphic information of the inventoried rock glaciers. Among the 413 rock glaciers (RGs), almost half of them (202 in total) are spatially connected to glaciers or debris-covered glaciers (G-RGs), and the debris-mantled slope-connected rock glaciers (DMS-RGs) are the second largest category, accounting for ~35% (143 in total) of the inventoried landforms. There are 41 rock glaciers occurring at the glacier forefield (GF-RGs)

and 27 developing at the terminus of talus (T-RGs), taking up ~10% and ~7% of the total amount, respectively.

All RGs are located at altitudes between 3389 m and 5541 m, with an average altitude of 4623 m. The G-RGs have a similar mean altitude of 4546 m. Both groups of landforms show a norm distribution in altitude (Figure 4.8a, c). The DMS-RGs generally occur at a higher altitude (Figure 4.8b), the average of which is up to 4889 m, whereas the GF-RGs and T-RGs are distributed at a lower elevation band (Figure 4.8d, e), whose average altitudes are 4265 m and 4332 m, respectively.

The G-RGs are the largest with an average area of 0.40 km² for individual landforms, followed by GF-RGs with a mean area of 0.38 km². Both are much (~50%) larger than the mean area (0.26 km²) of all RGs. The DMS-RGs are the smallest (0.05 km²), covering ~7% of the total area occupied by all RGs in the study region. The mean surface slope of all RGs is 17 °, which is similar to the mean slope (18 °) of the T-RGs. The G-RGs and GF-RGs have relatively flat surfaces with mean slope angles of 14 ° and 15 °, respectively, whereas the DMS-RGs develop a steeper average slope angle of 23 °. Most (64%) of the inventoried RGs occur on east-facing (0 °–180 °) slopes (Figure 4.9a) as the movement towards eastern direction is sensitive to the InSAR detection. Among different categories, the G-RGs and GF-RGs are more frequently located on northeastern-facing (0 °–90 °) slopes (Figure 4.9c, d), whereas the DMS-RGs and T-RGs mostly move towards southeastern directions (90 °–180 °) (Figure 4.9b, e).

Table 4.2 Statistical summary of the geomorphic parameters of the inventoried rock glaciers (All RGs), the debris-mantled slope-connected rock glaciers (DMS-RGs), the glacier-connected rock glaciers (G-RGs), the glacier forefield-connected rock glaciers (GF-RGs), and the talus-connected rock glaciers (T-RGs). Each column presents the mean values of the geomorphic parameter following by the corresponding standard deviations in the brackets.

	Number	Mean altitude (m)	Slope (°)	Area (km ²)	Total area (km ²)
All RGs	413	4623 (431)	17 (6)	0.26 (0.28)	108.27
DMS-RGs	143	4889 (325)	23 (5)	0.05 (0.04)	7.44
G-RGs	202	4546 (412)	14 (4)	0.40 (0.29)	79.79
GF-RGs	41	4265 (430)	15 (5)	0.38 (0.32)	15.51
T-RGs	27	4332 (224)	18 (5)	0.20 (0.13)	5.53

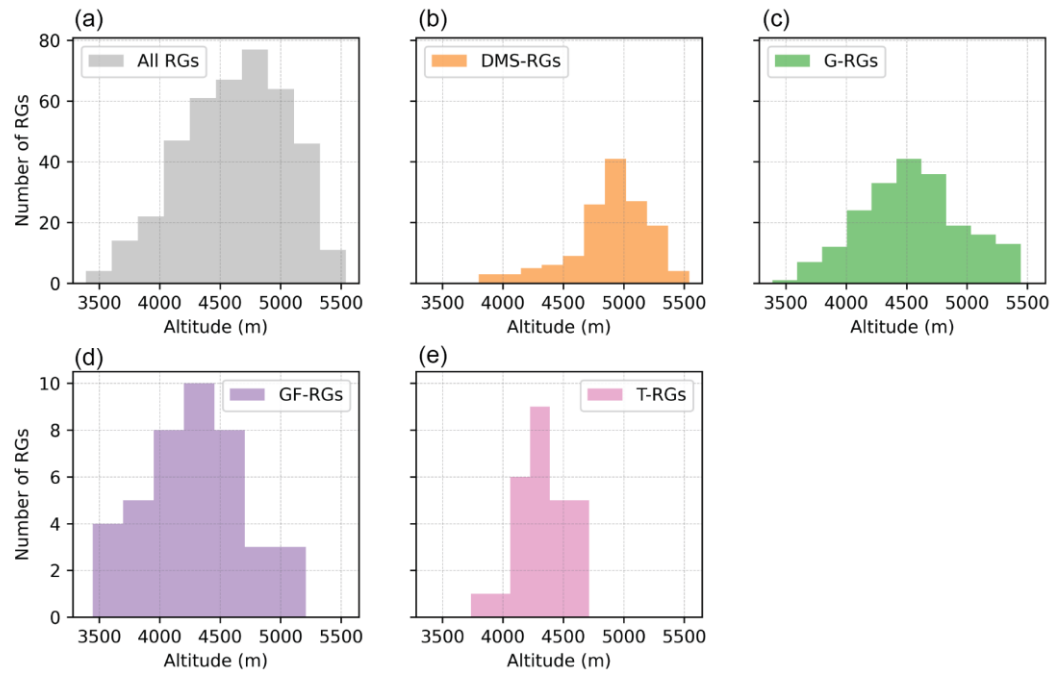


Figure 4.8 Histograms of the average altitudes for (a) all RGs, (b) DMS-RGs, (c) G-RGs, (d) GF-RGs, and (e) T-RGs, respectively. The altitudes are calculated from the SRTM DEM data.

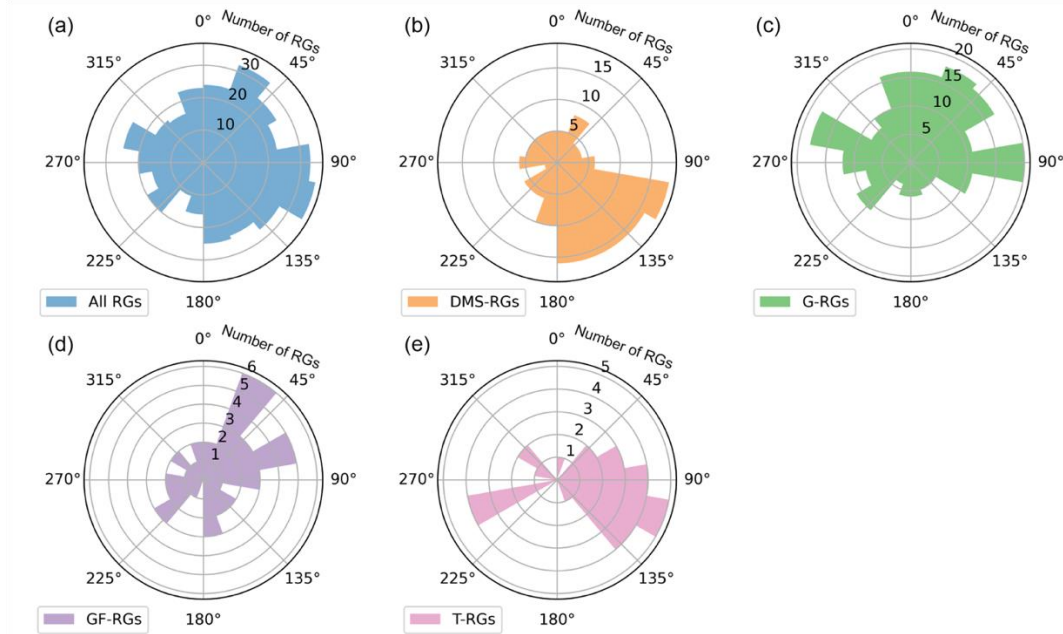


Figure 4.9 Histograms of the landform aspects for (a) all RGs, (b) DMS-RGs, (c) G-RGs, (d) GF-RGs, and (e) T-RGs.

4.4.3 Surface kinematics of the inventoried active rock glaciers

Among the 290 active rock glaciers mapped based on InSAR, we obtained the surface velocities of 256 rock glaciers in total, including 115 DMS-RGs, 97 G-RGs, 21 GF-RGs, and 23 T-RGs (Figure 4.10). Figure 4.11 gives examples of the velocity distributions of the four categories of rock glaciers. The spatial average velocities of the four rock glaciers are 79 ± 6 cm yr^{-1} (Figure 4.11a), 44 ± 1 cm yr^{-1} (Figure 4.11b), 32 ± 1 cm yr^{-1} (Figure 4.11c), and 24 ± 1 cm yr^{-1} (Figure 4.11d), respectively. The movement rates usually decrease towards the terminus with the highest values occurring in the upper and middle parts of the landforms.

Table 4.3 presents the general statistics of the documented rock glacier velocities. Most (90%) RGs move towards the downslope direction at a rate lower than 50 cm yr^{-1} , with a mean velocity of 24 cm yr^{-1} . The G-RGs and GF-RGs have faster mean velocities of 31 cm yr^{-1} and 35 cm yr^{-1} , respectively, whereas the DMS-RGs and T-RGs creep at a relatively lower rate of 17 cm yr^{-1} . The median velocities of the inventoried rock glaciers are all smaller than the corresponding mean velocities, indicating most of the data are distributed near the lower end, as shown in Figure 4.12. Among all the inventoried rock glaciers, a DMS-RG has the largest mean velocity of 127 ± 7 cm yr^{-1} .

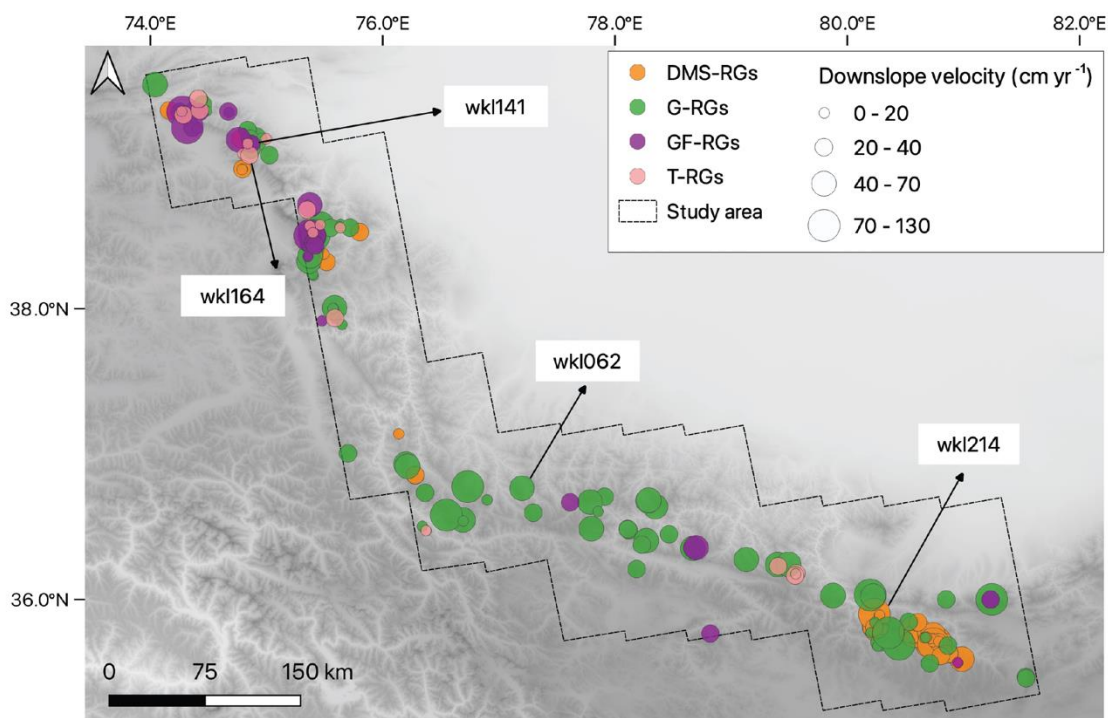


Figure 4.10 Distribution of the inventoried active rock glaciers in the study area. The four categories of rock glaciers are marked by different colours: orange for DMS-RGs, green for G-RGs, purple for GF-RGs, and pink for T-RGs. The size of the dots indicates the mean downslope velocity of each landform. Four rock glacier IDs are labelled on the figure to show the locations of the example landforms in Figure 4.11.

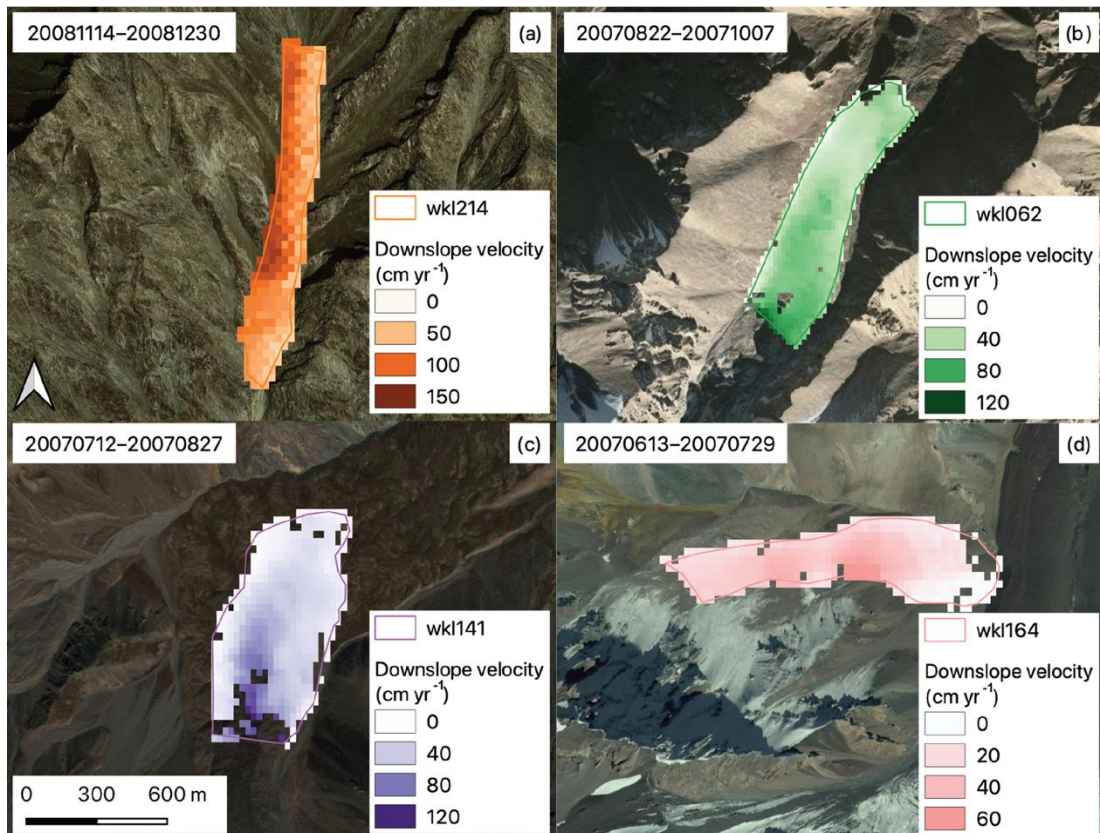


Figure 4.11 Velocity field maps show the downslope movement rates of rock glaciers of different categories including (a) a DMS-RG, (b) a G-RG, (c) a GF-RG, and (d) a T-RG. The rock glacier IDs are wkl214, wkl062, wkl141, and wkl164, respectively. The corresponding locations are shown in Figure 4.. The background maps are Google Earth images.

Table 4.3 Statistical summary of the kinematic features of the inventoried rock glaciers. The mean velocity column gives the mean value of the rock glacier movement rate for each category and the standard deviations in the brackets. The median and maximum velocity columns present the median and largest landform creep velocity in each category with their associated uncertainties, respectively.

	Number	Mean velocity (cm yr ⁻¹)	Median velocity (cm yr ⁻¹)	Maximum velocity (cm yr ⁻¹)
All RGs	256	24 (22)	17±1	127±7
DMS-RGs	115	17 (18)	12±1	127±7
G-RGs	97	31 (22)	25±1	110±1
GF-RGs	21	35 (30)	25±1	124±4
T-RGs	23	17 (8)	16±1	36±1

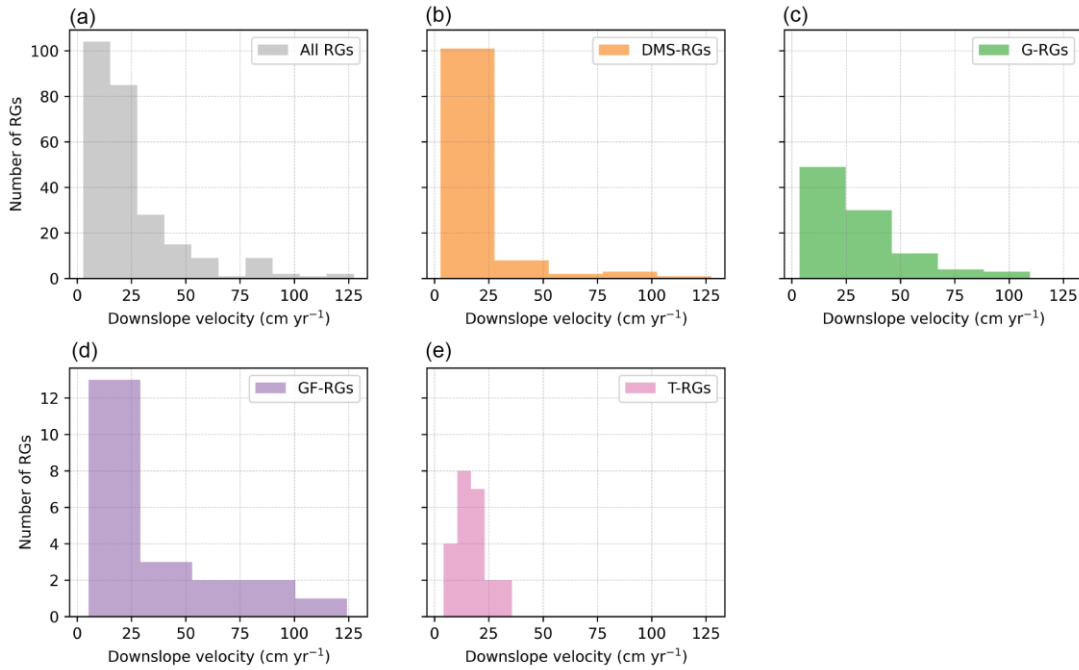


Figure 4.12 Histograms of the downslope velocities for (a) all RGs, (b) DMS-RGs, (c) G-RGs, (d) GF-RGs, and (e) T-RGs, respectively.

4.5 Discussion

In this section, we firstly summarize the potential and limitations of using the combined methodology for mapping rock glaciers (Sect. 4.5.1). Then we discuss the genetic and evolutional implications carried by the geomorphic characteristics of the inventoried rock glaciers (Sect. 4.5.2).

4.5.1 Potential and limitations of the InSAR-Deep learning combined method for mapping rock glaciers

We used an InSAR-Deep learning combined approach to inventory rock glaciers across the West Kunlun Mountains. Advantage of the combined methodology is twofold: the InSAR-based mapping approach provides essential information of surface kinematics and accurate manual delineation for training the deep learning model, meanwhile the automated method improves mapping efficiency and more importantly, overcomes the conservativeness of the former approach, as some rock glaciers cannot be detected by InSAR due to coherence loss in interferogram, geometric distortions, their topographic orientations insensitive to InSAR line-of-sight measurements, or simply their inactive kinematic status (Robson et al., 2020; Wang et al., 2017).

However, automation of the methodology is limited by the amount and quality of training and validation samples, which primarily control the performance of this approach. In this study, the training and validation datasets consist of the boundaries of active rock glaciers in the

InSAR-based sub-inventory overlying the Sentinel-2 optical images (examples as shown in Figure 4.5). The amount of rock glaciers (172) as training and validation samples is in the same magnitude as the landform amount (338) for training previously developed deep learning network (Robson et al., 2020), yet the data size can be improved to fully achieve the potential of the state-of-the-art network (DeepLabv3+Xception71) we adopted. Quality of the input images is also moderate, as Sentinel-2 images have a medium spatial resolution of ~10 m, making it challenging to characterize some rock glaciers, especially small ones, from these optical images occasionally and possibly leading to inaccuracy in the output. Therefore, manual inspection is required as the post-processing procedure to improve the accuracy of the automatically delineated boundaries. In addition, the Google Earth images (2009–2020) we referred to while creating the InSAR-based sub-inventory are unsynchronized with the Sentinel-2 images (Jul–Aug of 2018) we used for producing the training data and for predicting rock glaciers by the trained model. Accordingly, we applied an additional manual inspection while preparing the input data, although most boundaries need little modifications as rock glacier activity in this study area is relatively low (Sect. 4.4.3) and the small changes occurring during the time difference are insignificant on the medium-resolution Sentinel-2 images.

Considering the above limitations, several improvements can be implemented in our future research: (1) to increase the amount and diversity of training samples by including rock glacier boundaries from other regions; (2) to adopt high-resolution optical images for producing input dataset; and (3) to prepare training data using optical images of the same source and period as the images for landform inference.

4.5.2 Genetic and evolutional implications from the geomorphic characteristics of rock glaciers

We classified the inventoried rock glaciers into glacier-connected (G-RGs), glacier-forefield-connected (GF-RGs), debris-mantled slope-connected (DMS-RGs), and talus-connected rock glaciers (T-RGs). This classification scheme was adopted firstly for a practical reason: spatial connection of the rock glacier to upslope unit is mostly well discernible from the optical images (as illustrated in Figure 4.2). Moreover, we take the distinction as an indication of the evolution of rock glaciers in terms of their ice origin, sediment source, and debris transfer process. In this subsection, we interpret the genetic and evolutional implications held by the characteristics of rock glaciers in the regional geomorphologic context.

Nearly half (~49%) of the inventoried rock glaciers are spatially connected to glaciers. The amount appears to be reasonable because much of the West Kunlun Mountains (~12500 km²) is occupied by modern glaciers (Käab et al., 2015), constituting one of the most prominent glacierization centers on the Tibetan Plateau (Shi, 2006). G-RGs occurring at the immediate

downslope of the modern glaciers are likely to have the ice core embedded within the landforms, representing the transitional process from glacier (or debris-covered glacier) to rock glacier (Potter, 1972; Whalley and Azizi, 1994). However, we postulate that such transition is not actively ongoing given that glaciers in the West Kunlun are in mass balance or even slightly gaining mass in recent decades (Bao et al., 2015; Käb et al., 2015; Wang et al., 2018; Zhou et al., 2018). The G-RGs in our inventory are likely to gradually evolve from glacier to rock glacier since the last cold period, i.e., the Little Ice Age (LIA, 200–600 aBP), and this transitional process tend to slow down in the past several decades (Shi, 2006).

Although the landform transition is currently not active in our study area, we propose that the glacier-to-rock glacier continuum, as one classical theory about rock glacier genesis (Berthling, 2011), can be adopted to interpret the evolution of the GF-RGs in our inventory. The GF-RGs are spatially disconnected from the upslope modern glaciers (Figure 4.2c), occurring at the lowest altitudes among all categories. Interactions between the GF-RGs and the glacier units are likely to take place during the glacier advance phase in geologic history. Anderson et al. (2018) modelled the glacier – debris-covered glacier – rock glacier evolutional process by simulating the rise of environmental equilibrium line altitude (ELA) in response to climate warming: the pure glacier melts and separates from the emerging debris-covered terminus, which preserves its ice core due to insulation effect produced by the surface sediment and finally transforms into a rock glacier. Accordingly, we postulate that the GF-RGs in our study area once were part of the upslope glaciers during the Neoglaciation (3000–4000 aBP), when glaciers extended to altitudes hundreds of meters lower than the present glacier termini in the West Kunlun (Li and Shi, 1992; Shi, 2006).

In addition, the West Kunlun Mountains are characterized by the occurrence of abundant surge-type glaciers, whose flow velocities peaking at $0.2\text{--}1 \text{ km yr}^{-1}$ during their active phases (Quincey et al., 2015; Yasuda and Furuya, 2015). Excess materials consisting of ice and debris are carried downslope to areas far beyond the normal termini of the surge-type glaciers and may deliver sediments to the nearby glaciers (or debris-covered glaciers), whereby the surge events tend to contribute to the glacier-to-rock glacier transition provided that glaciers in the West Kunlun will undergo retreat in the future as the glaciers in other alpine regions worldwide nowadays. A comparable case is the ongoing glacier-to-rock glacier transition in the Himalayas: based on field observations and sedimentologic analysis, Jones et al. (2019a) elaborated that debris supply from the environmental sediment sources (in addition to the sediment derived from glaciation of the transitional landform per se) drives the evolution as an important factor. Moreover, the ice-debris body transferred and deposited at the far end of the glacier may gradually evolve into a rock glacier under favorable climatic and topographic conditions (Figure 4.13).

The T-RGs are conventionally considered as features originated in the periglacial domain: the rock glaciers contain interstitial ice developed by various processes such as burial of surface snow that typically occur in the formation of frozen ground (Berthling, 2011; Haeberli, 2000; Humlum, 1988). The DMS-RGs are seldomly reported in the literature (Hu et al., 2021), yet display unique geomorphologic characteristics and constitute the second largest category (~35%) in the study area. In the absence of an upslope glacial system, we suggest that the DMS-RGs also represent the periglacial processes controlling the landform genesis. In comparison with the other three categories in our inventory, the DMS-RGs occupy the highest and steepest slopes, where mechanical weathering dominates and produces sufficient sediments transferred and accumulated to the base of the slopes. During the glacial period, interstitial ice is formed within the deposits. The ice-debris mixture gradually develops and at one point overcomes the friction and starts to creep as an active rock glacier. Considering the lack of a headwall and the very small dimension (~one fifth of the average size of all inventoried landforms), it is likely that the DMS-RGs began to emerge during the LIA and are still at their embryonic stage.

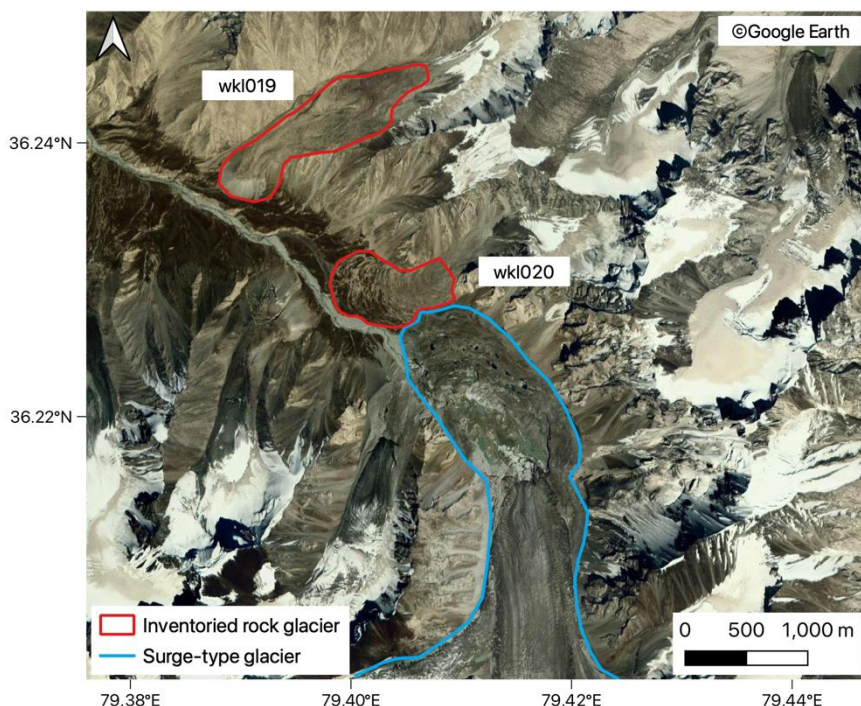


Figure 4.13 The blue line delineates the boundary of a surge-type glacier (Chudley and Willis, 2019), whose terminus part is covered by debris. Many thermokarsts develop on the surface of the ice-debris mixture, which is likely to transform into a rock glacier in a warming climate. Two rock glaciers (wkl019 and wkl020) are situated in the surroundings and may receive debris and ice input during the surge events.

4.6 Conclusions

We mapped rock glaciers at a regional scale semi-automatically and quantified their surface kinematics by combining InSAR and image semantic segmentation powered by deep learning. The combined method was applied to compile the first rock glacier inventory across the West Kunlun Mountains. We draw the main conclusions as follows:

- (1) The DeepLabv3+ network trained by manually labelled data based on InSAR and Google Earth images can successfully identify and delineate rock glaciers from Sentinel-2 images, attaining an IoU value of 0.801 for both training and validation datasets. The well-trained model newly mapped 123 rock glaciers to supplement the non-exhaustive InSAR-based inventory of 290 active rock glaciers.
- (2) There are 413 rock glaciers mapped over the study area, including 202 glacier-connected rock glaciers (G-RGs), 143 debris-mantled slope-connected rock glaciers (DMS-RGs), 41 glacier forefield-connected rock glaciers (GF-RGs), and 27 talus-connected rock glaciers (T-RGs). The inventoried rock glaciers occupy an area of $\sim 108 \text{ km}^2$ in total and are located at altitudes between 3389 m and 5541 m. The average slope angle is 17° and the dominating landform aspect is towards the east.
- (3) Among the mapped rock glaciers, the G-RGs and GF-RGs are larger (average areas: 0.40 km^2 and 0.38 km^2) and occur on gentler slopes (14° and 15°) predominantly facing northeast, whereas the DMS-RGs are the smallest (0.05 km^2) and occupy steeper (23°) southeast-facing slopes at the highest altitudes (4889 m). The T-RGs display a medium size (0.20 km^2) and slope angle (18°) and mostly occur on southeast-facing slopes at lower altitudes (4332 m). The GF-RGs have the lowest average altitude (4265 m).
- (4) Considering the geomorphologic context, we postulated that the glacier – debris-covered glacier – rock glacier transition is currently inactive due to the abnormal mass gain of glaciers in the West Kunlun: the inventoried G-RGs and GF-RGs evolved from glacier to rock glacier during the past Holocene glacial periods, e.g., the Little Ice Age and the Neoglaciation. Surge events of glaciers may provide material supply and promote the glacier-to-rock glacier transition in the future.
- (5) Based on the geomorphic characteristics of inventoried rock glaciers, we suggest that the genesis of T-RGs and DMS-RGs are controlled by periglacial processes. The DMS-RGs, as a distinct type of rock glaciers in our study area, represent embryonic rock glaciers derived from prevalent mechanical erosion of the slopes and interstitial ice formation during the Little Ice Age. Note that the hypothesis on landform genesis formulated here need further validation based on measured evidence.

(6) We adopted the spatial average velocity of all pixels within the boundary of each rock glacier to represent the landform surface kinematics. In total, 256 rock glaciers have valid kinematic quantifications. Nearly 90% of the rock glaciers move at a rate lower than 50 cm yr^{-1} . The mean downslope velocity is 24 cm yr^{-1} , and the standard deviation is 22 cm yr^{-1} . The median and maximum velocities are 17 cm yr^{-1} and 127 cm yr^{-1} , respectively.

(7) Among the active rock glaciers, the G-RGs and GF-RGs move faster at mean velocities of 31 cm yr^{-1} and 35 cm yr^{-1} , respectively. The DMS-RGs and T-RGs creep at a slower average rate of 17 cm yr^{-1} .

In summary, combining InSAR and high-resolution optical imagery to manually map active rock glaciers proves to be an effective way to quantify rock glacier kinematics consistently in remote areas. With the utilization of deep learning techniques, it is promising to compile rock glacier inventories efficiently over a significant extent of permafrost areas, e.g., the Tibetan Plateau, which provides a baseline dataset and allows the monitoring of rock glaciers as indicators of permafrost degradation and potential water sources in a changing climate.

Chapter 5 Modelling rock glacier velocity and ice content, Khumbu and Lhotse Valleys, Nepal

*“So far as the laws of mathematics refer to reality, they are not certain.
And so far as they are certain, they do not refer to reality.”
—Albert Einstein, Geometry and Experience*

Rock glaciers contain significant amounts of ground ice and serve as important freshwater resources as mountain glaciers melt in response to climate warming. However, current knowledge about ice content in rock glaciers has been acquired mainly from in situ investigations in limited study areas, which hinders a comprehensive understanding of ice storage in rock glaciers situated in remote mountains over local to regional scales. In this study, we develop an empirical rheological model to infer ice content of rock glaciers using readily available input data, including rock glacier planar shape, surface slope angle, active layer thickness, and surface creep rate. The model is calibrated and validated using observational data from the Chilean Andes and Swiss Alps. We apply the model to infer the ice content of five rock glaciers in Khumbu and Lhotse Valleys, north-eastern Nepal. The velocity constraints applied to the model are derived from Interferometric Synthetic Aperture Radar (InSAR) measurements. The inferred volumetric ice fraction in Khumbu and Lhotse Valleys ranges from 71% to 75.3% and water volume equivalents lie between 1.40 to 5.92 million m³ for individual landforms. Considering previous mapping results and extrapolating from our findings to the entire Nepalese Himalaya, the total amount of water stored in rock glaciers could be in the magnitude of 10 billion m³, equivalent to a ratio of 1:17 between rock glacier and glacier reservoirs. Due to the accessibility of the input parameters of the model developed in this study, it is promising to apply the approach to permafrost regions where previous information about ice content of rock glaciers is lacking, and ultimately to estimate the water storage potential of the remotely located rock glaciers.

5.1 Introduction

Rock glaciers are valley-floor and valley-side landforms consisting of ice-rock mixtures and are common in all arid and cold mountain regions. Recent research has suggested that they represent significant hydrological resources in areas where ice glaciers are undergoing recession in the face of climate change (Azócar and Brenning, 2010; Jones et al., 2018a; Munroe, 2018; Rangecroft et al., 2014). The potential hydrological value of rock glaciers, and thus their importance in terms of hydrological research, was first noted by Corte (1976); despite this, research on the role of rock glaciers in maintaining hydrological stores in mountain catchments remains limited.

In regions such as the Himalaya, recent research has argued that rock glaciers might represent the end-member of an evolutionary process where some ice glaciers undergo transitions to debris-covered glaciers, a proportion of which will then undergo further transition to rock glaciers (Jones et al., 2019a; Knight et al., 2019). This process would be triggered by the paraglacial response of high mountain slopes as glaciers undergo downwasting, producing rock slope failures, mountain side collapse, and increasing the flux of rock debris to glacier surfaces. Depending on debris cover thickness, this would be expected to limit ice melting and increase the resilience of the glacier to climate change (e.g., Reznichenko et al., 2010).

Recent work (Jones et al., 2021) was the first to show that around 25,000 rock glaciers exist in the Himalayas, covering $3,747 \text{ km}^2$ and containing $51.80 \pm 10.36 \text{ km}^3$ of water. The comparative importance of rock glacier ice content versus that in glaciers in the region was 1:24, ranging from 1:42 to 1:17 in the Eastern and Central Himalaya and falling to 1:9 in Nepal. Importantly, we expect these existing ratios to reduce significantly as ice glaciers melt and undergo transitions to rock glaciers; yet the rates of transition from glacier to rock glacier are not understood. We also expect rock glaciers to provide water supplies long after ice glaciers have melted; in other high arid mountains, such as the Andes, ice-cored rock glaciers have persisted in valleys long after glacier recession (Azúcar and Brenning, 2010; Monnier and Kinnard, 2015b). However, there have been no modelling studies to test these postulations and assess the likelihood of glacier-rock glacier transition and the hydrological implications of this process.

A significant gap in our understanding of the likely future hydrological role of rock glaciers in arid mountains is the absence of quantitative information concerning their ice content. Currently, estimates of ice content in rock glaciers have focused on empirical information from drilling cores and boreholes (Arenson et al., 2002; Berthling et al., 2000; Croce and Milana, 2002; Florentine et al., 2014; Fukui et al., 2007; Fukui et al., 2008; Guglielmin et al., 2004; Guglielmin et al., 2018; Haeberli et al., 1998; Haeberli et al., 1999; Hausmann et al., 2007; Krainer et al., 2015; Leopold et al., 2011; Monnier and Kinnard, 2013, 2015a, 2015b; Steig et al., 1998), and from geophysical surveys (e.g., for reviews see: Hauck, 2013; Kneisel et al., 2008; Scott et al., 1990). However, these approaches are costly, time-consuming and extremely difficult to apply to rock glaciers at high altitudes and in remote mountains. It is therefore desirable to develop other alternative approaches to understanding the likely ice content of rock glaciers, especially for regional-scale estimate.

Ice content is one factor controlling the movement of rock glaciers by influencing the driving force and the rheological properties of materials which constitute the permafrost core (Arenson and Springman, 2005a; Cicoira et al., 2020), thus it is feasible to infer ice content using

rheological modelling and observed kinematic data. Here we adapt an empirical rheological model by integrating rheological properties of rock glaciers derived from laboratory experiments (Arenson and Springman, 2005a), and parameterize the rheological model based on the structure and composition data of Las Liebres rock glacier (Monnier and Kinnard, 2015a; Monnier and Kinnard, 2016). We then apply the model to simulate surface velocities of four rock glaciers with known ice content in the Swiss Alps and evaluate the modelling results to determine a suitable parameterization scheme. Finally, we present results from modelling the kinematic response of the coherently moving part of five rock glaciers in the study region of north-eastern Nepal and assessing the modelled movement as a proxy for ice content by using InSAR-derived downslope velocities as constraints.

5.2 Study area

Our study area comprises the Khumbu and Lhotse valleys in North-eastern Nepal (Figure 5.1a). The glaciers draining Everest and Lhotse (e.g., Khumbu and Lhotse glaciers) are the highest in the world and have well defined debris-covered snouts. The tributary valleys contain a variety of rock glaciers and composite landforms where ice glaciers are transitioning to rock glaciers (Jones et al., 2019a; Knight et al., 2019). There are five rock glaciers in the study area, namely Kala-Patthar, Kongma, Lingten, Nuptse, and Lobuche (Figure 5.1b). The ice-debris landforms in this study are situated at 4900–5090 m a.s.l., near the altitudinal boundary of discontinuous permafrost in the region. Previous seismic refraction surveys conducted on active rock glaciers indicate that the lower limit of permafrost occurrence in this region to be approximately 5000–5300 m a.s.l. (Jakob, 1992), which is consistent with an earlier estimate of 4900 m a.s.l. based on ground temperature measurements (Fujii and Higuchi, 1976).

Meteorological data provided by the Pyramid Observatory Laboratory near Lobuche village on the western side of the Khumbu Glacier (5050 m a.s.l.) reveal that the dominating climate of this area is the South Asian Summer Monsoon. For the period of 1994–2013, recorded accumulated annual precipitation is 449 mm yr⁻¹, with a concentration of 90% of precipitation amount during June–September (Salerno et al., 2015). The mean annual air temperature is -2.4 °C (Salerno et al., 2015).

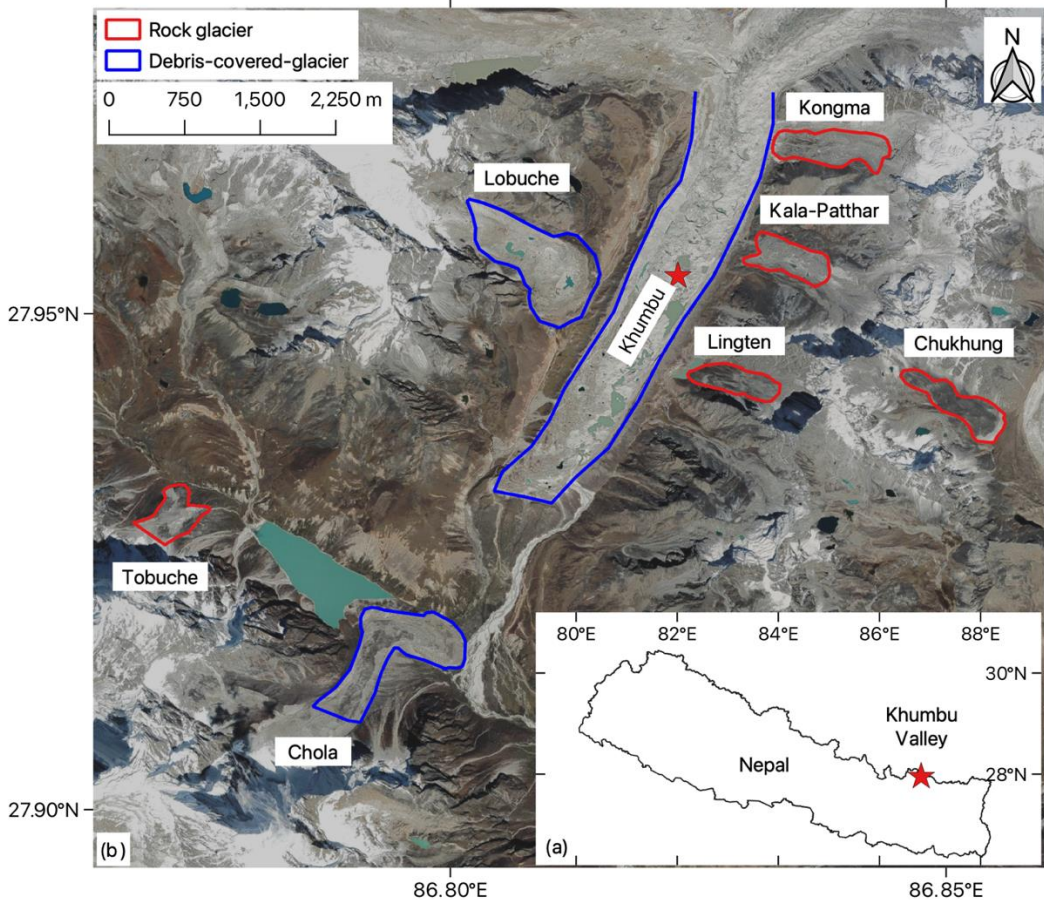


Figure 5.1 (a) Location of the study site; (b) Google Earth images showing the spatial distribution of the active ice-debris landforms, including rock glaciers (RG) in red outlines and debris-covered glaciers (DCG) in blue boundaries. RGs are delineated based on Google Earth images (Jones et al., 2018b).

5.3 Methods

Our methods are divided into two parts and detailed in the subsections below. First, we derived surface kinematics of rock glaciers using Interferometric Synthetic Aperture Radar (InSAR; Section 5.3.1). Second, we developed a rheological model for estimating ice content of rock glaciers by using surface velocity as a constraint. We detailed the model design, calibration, and validation procedures, as well as application of the model (Section 5.3.2).

5.3.1 Deriving surface kinematics with InSAR

Nineteen L-band ALOS PALSAR images and twenty-one ALOS-2 PALSAR-2 images acquired during 2006–2010 and 2015–2020, respectively, were used to form more than fifty interferograms to measure the surface displacement of the landforms in the study area (Table 5.1). We selected SAR data to achieve high interferometric coherence by following the criteria as: (1) short temporal spans (less than 92 days for ALOS pairs and 70 days for ALOS-2 pairs); (2) short perpendicular baselines (smaller than 800 m for ALOS pairs and 400 m for ALOS-2

pairs). We estimated and removed the topographic phase with the 1-arcsec digital elevation models (DEM) produced by the Shuttle Radar Topography Mission (SRTM) (spatial resolution ~30 m). Multi-looking operation and adaptive Goldstein filter (8×8 pixels) were applied to the interferometric processing, which was implemented by the open-source software ISCE version 2.4.2 (available at <https://github.com/isce-framework/isce2>). The interferograms were unwrapped using the SNAPHU software (Chen and Zebker, 2002). We randomly selected three pixels located at flat and stable ground near each ice-debris landform and averaged their phase values to re-reference the unwrapped phases measured within the landforms. By doing so, atmospheric artifacts including the water vapor delay and ionospheric effects can be effectively removed because these are spatially long-wave features and can be assumed as constant within the range of our study objects (Hanssen, 2001).

We then derived the surface velocities along the SAR satellite line-of-sight (LOS) from the unwrapped interferograms and projected the LOS velocities to the downslope direction of the landforms. Uncertainties were quantified by considering the error propagation of the InSAR measurements and associated geometry parameters (Hu et al., 2021).

After that, to ensure high data quality, we selected the InSAR observations meeting the following criteria as valid results for further analyses: (1) the average coherence of all the pixels within the boundary of one landform is higher than 0.3; (2) the pixels showing low coherence (<0.3) are masked out before velocity statistics, and more than 40% of pixels remain after the masking procedure; (3) the mean velocity of the landform is larger than 5 cm yr^{-1} .

Next, we defined and outlined the coherently moving part of the landform by considering the time series of downslope velocity of each pixel acquired during all the observational periods. If one pixel moved at a rate larger than 5 cm yr^{-1} in more than half of the periods, it was included into the coherently moving part of the landform.

Finally, we analyzed the velocity values of all pixels within the coherently moving part of the landform and selected the mean, median, and maximum values for each observation to characterize the surface kinematics of the landforms.

Table 5.1 List of ALOS-1 PALSAR and ALOS-2 PALSAR-2 data information.

Satellite	Acquisition interval (days)	Period	Path/frame	Orbit direction	No. of interferograms
ALOS	46	Dec 2007 to Feb 2010	507/540	Ascending	8
		Dec 2007 to Feb 2010	507/550		6
		Jun 2007 to Feb 2010	508/540		4
		May 2006 to Jul 2006	511/540		1
ALOS-2	14	Mar 2015	48/3050	Descending	1
		Jun 2015 to Feb 2020	156/550	Ascending	20

5.3.2 Estimating ice content from a surface-velocity-constrained model

This subsection describes the process of model development. The detailed workflow is illustrated in Figure 5.2.

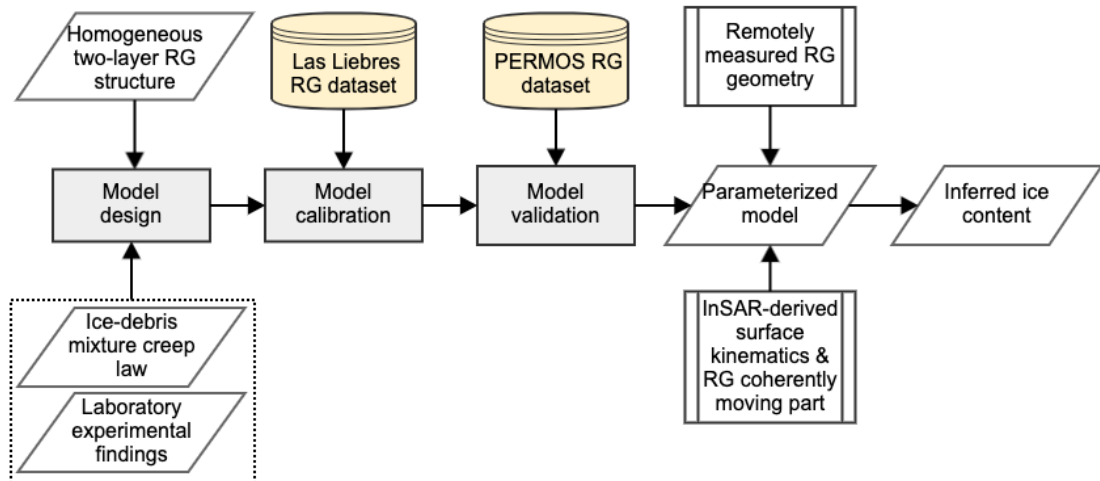


Figure 5.2 Diagram of the workflow conducted in this study to develop and apply a modelling approach for inferring ice content of rock glaciers (RG).

5.3.3 Model design and assumptions

Active rock glaciers creep as a result of two internal processes: plastic deformation of the ice-rich permafrost core, and deformation at the shear horizon at depth (e.g., Arenson et al., 2002; Berthling, 2011; Ciciora et al., 2019b; Haeberli, 2000; Kenner et al., 2019). Many previous modelling studies depict the deformation mechanism of rock glaciers based on Glen's flow law (e.g., Arenson and Springman, 2005a; Ciciora et al., 2020; Whalley and Azizi, 1994), which essentially introduces strain rate ($\dot{\varepsilon}$) with effective shear stress (τ) and describes the rheology of ice flow (Glen, 1955):

$$\dot{\varepsilon} = A\tau^n , \quad (5.1)$$

where A and n are parameters reflecting variations in environmental conditions (mainly including temperature and pressure), material properties (such as composition, structure, and texture), and operating creep mechanisms (e.g., diffusion and dislocation).

In this study, we primarily adopted a creep model of ice-debris mixture, proposed by Moore (2014), based on Glen's flow law:

$$\dot{\varepsilon} = EA[(\tau - \tau_{th})\Gamma]^n, \quad (5.2)$$

where E is a strain enhancement factor; Γ is a parameter reflecting the strength of the ice-debris mixture, associated with the volumetric debris content (θ_d). When θ_d is less than a critical volumetric debris content (θ_{dc}), the strength of the mixture is governed by interparticle friction, and the value of Γ equals to one. Theoretically, θ_{dc} is around 0.52 (Moore, 2014). τ_{th} is a threshold stress imparted by the frictional strength between debris particles, also depending upon the volumetric debris content (θ_d).

Assuming that $\tau_{th} \ll \tau$, $\theta_d < \theta_{dc}$, and $\Gamma = 1$, Equation 5.2 can be reduced to the following form (Monnier and Kinnard, 2016):

$$\dot{\varepsilon} = \left(\frac{\tau}{B}\right)^n, \quad (5.3)$$

where B is the effective viscosity and is equal to $\left(\frac{1}{EA}\right)^{\frac{1}{n}}$.

We consider each rock glacier as a slab with uniform width and thickness and a semi-elliptical cross-section, resting on a bed of constant slope, following a common setup in glaciology (Cuffey and Paterson, 2010). It constitutes of two layers: an active layer and a permafrost core. The active layer is a mixture of debris and air, and the permafrost core consists of ice, water, debris and air. Both layers are assumed as homogeneous. Movement of rock glaciers results from the steady creep of the permafrost core in the plane parallel to the bed slope. The active layer moves passively along with the inner core, which has been validated by observations (Arenson et al., 2002; Haeberli, 2000). From Equation 5.3 and the structure and geometry illustrated in Figure 5.3, we have:

$$\frac{du}{dz} = 2 \left(\frac{\tau}{B}\right)^n, \quad (5.4)$$

where $\frac{du}{dz}$ is the velocity derivative relative to the depth z in the permafrost core.

At a given depth z , the driving stress τ is imparted, taking into account the loading of the above material and the effect of frictional drag occurring between the lateral margins and surrounding bedrocks, which is represented by a shape factor S_f (Cuffey and Paterson, 2010):

$$\tau(z) = S_f \sin \alpha (\rho_{al} g h_{al} + \rho_{core} g z), \quad (5.5)$$

where α is the slope angle; g is the gravitational acceleration; ρ_{al} and ρ_{core} are the densities of the active layer and the permafrost core, respectively; h_{al} is the active layer thickness.

The shape factor is expressed as (Oerlemans, 2001):

$$S_f = \frac{\pi}{2} \arctan\left(\frac{W}{2T}\right), \quad (5.6)$$

where W and T are the width and thickness of the rock glacier, respectively.

The integration of the velocity profile (Equation 5.4 and 5.5) is expressed as:

$$\int_0^z du = -2 \left(\frac{S_f g \sin \alpha}{B} \right)^n \int_0^z (\rho_{al} h_{al} + \rho_{core} z)^n dz, \quad (5.7)$$

$$u(z) = u_s - \frac{2(\rho_{al} h_{al} + \rho_{core} z)^{n+1}}{\rho_{core}(n+1)} \left(\frac{S_f g \sin \alpha}{B} \right)^n, \quad (5.8)$$

where u_s is the surface velocity as illustrated in Figure 5.3. When z is set as the thickness of the ice core (h_{core}) and basal sliding is assumed to be absent, u_s is then expressed as:

$$u_s = \frac{2(\rho_{al} h_{al} + \rho_{core} h_{core})^{n+1}}{\rho_{core}(n+1)} \left(\frac{S_f g \sin \alpha}{B} \right)^n, \quad (5.9)$$

The densities of the active layer (ρ_{al}) and the permafrost core (ρ_{core}) are given as:

$$\rho_{al} = \theta_{d,al} \rho_d + \theta_{a,al} \rho_a, \quad (5.10)$$

$$\rho_{core} = \theta_{d,core} \rho_d + \theta_{a,core} \rho_a + \theta_{i,core} \rho_i + \theta_{w,core} \rho_w, \quad (5.11)$$

where $\theta_{d,al}$ and $\theta_{a,al}$ are the volumetric contents of debris and air in the active layer, respectively. The volumetric contents of the components in the inner core, namely debris, air, ice and water, are expressed as $\theta_{d,core}$, $\theta_{a,core}$, $\theta_{i,core}$, and $\theta_{w,core}$, respectively. ρ_d , ρ_a , ρ_i , and ρ_w are the densities of debris, air, ice, and water, respectively.

For the flow law exponent (n), we first used an empirical average value as assumed in numerous glaciological studies:

$$n = 3, \quad (5.12)$$

We also adopted a linear relationship between n and the volumetric ice content ($\theta_{i,core}$) based on laboratory experiments undertaken on borehole samples from two rock glaciers (Arenson and Springman, 2005a):

$$n = 3\theta_{i,core}, \quad (5.13)$$

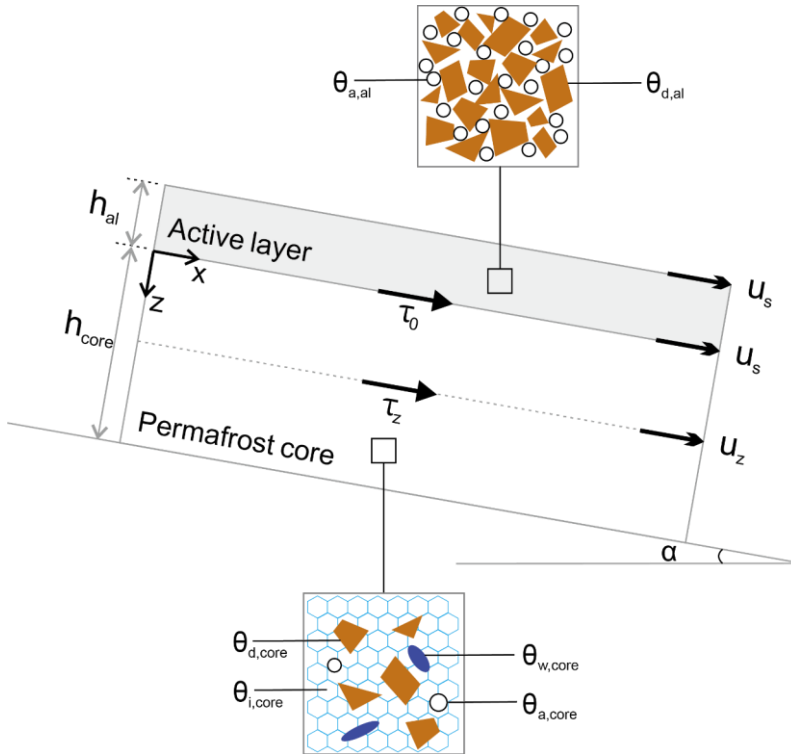


Figure 5.3 Schematic geometry, structure, stress status, and composition of rock glaciers. The rock glacier consists of a permafrost core underlying the active layer. Parameters involved in the model include surface slope (α), active layer thickness (h_{al}), thickness of permafrost core (h_{core}), driving stress at the base of the active layer (τ_0), driving stress at depth z (τ_z), surface velocity (u_s), velocity at depth z (u_z). $\theta_{d,al}$ and $\theta_{a,al}$ refer to the debris fraction and air fraction of the active layer. $\theta_{d,core}$, $\theta_{i,core}$, $\theta_{w,core}$, and $\theta_{a,core}$ are the fractions of debris, ice, water, and air in the permafrost core, respectively.

5.3.3.1 Model calibration

Combining Equations 5.9–5.11 with Equations 5.12 or 5.13, we formulated several models depicting the relationship between the surface velocity and properties of rock glaciers; including their composition, structure and geometry. We then calibrated the models to determine the curve of best fit between the effective viscosity (B) and the volumetric ice content ($\theta_{i,core}$) using observational data of Las Liebres rock glacier in Central Chilean Andes, collected by Monnier and Kinnard (2015a). This dataset includes information of structure (h_{core} and h_{al}), geometry (α and S_f), and composition ($\theta_{d,core}$, $\theta_{a,core}$, $\theta_{i,core}$, and $\theta_{w,core}$), all of which were derived from Ground Penetrating Radar (GPR) measurements. Surface velocities (u_s) were provided by a Differential Global Positioning System (DGPS) along the

central creep line at 14 locations on Las Liebres rock glacier, as detailed in Monnier and Kinnard (2015 & 2016).

First we adopted the exponential $B-\theta_{i,core}$ relation estimated by Monnier & Kinnard (2016) with the same dataset and a constant creep parameter n (Equation 5.12) (Figure 5.4a). Then by integrating the relationship between n and ice content (Equation 5.13), we applied both a 2nd degree polynomial regression model and an exponential regression model to determine the $B-\theta_{i,core}$ relationship (Figure 5.4b, c) The polynomial regression model is used to capture the subtle increase in effective viscosity when ice fraction becomes larger at the ice-rich end. This trend is also depicted in the laboratory experiment conducted by Arenson and Springman (2005a) as a parabolic relationship between the minimum axial creep strain rate and the volumetric ice content. Finally, we obtained three candidate parameterization schemes expressed as:

$$u_s = \frac{2(\rho_{at}h_{al} + \rho_{core}h_{core})^4}{\rho_{core}(n+1)} \left(\frac{S_f g \sin \alpha}{35300e^{2.01\theta_{i,core}}} \right)^3, \quad (5.14)$$

$$u_s = \frac{2(\rho_{at}h_{al} + \rho_{core}h_{core})^{3\theta_{i,core}+1}}{\rho_{core}(n+1)} \left(\frac{S_f g \sin \alpha}{7183435\theta_{i,core}^2 - 9543596\theta_{i,core} + 3322637} \right)^{3\theta_{i,core}}, \quad (5.15)$$

$$u_s = \frac{2(\rho_{at}h_{al} + \rho_{core}h_{core})^{3\theta_{i,core}+1}}{\rho_{core}(n+1)} \left(\frac{S_f g \sin \alpha}{5217905e^{-5.26\theta_{i,core}}} \right)^{3\theta_{i,core}}, \quad (5.16)$$

For simplicity, the parameterization scheme proposed in Monnier & Kinnard (2016) is labelled as Scheme 1 (Equation 5.14). The parameterization schemes considering the empirical relation between n and $\theta_{i,core}$ (Equation 5.13) and parameterization scheme derived from the polynomial and exponential relationship between B and $\theta_{i,core}$ are marked as Scheme 2 and Scheme 3 (Equations 5.15 and 5.16), respectively.

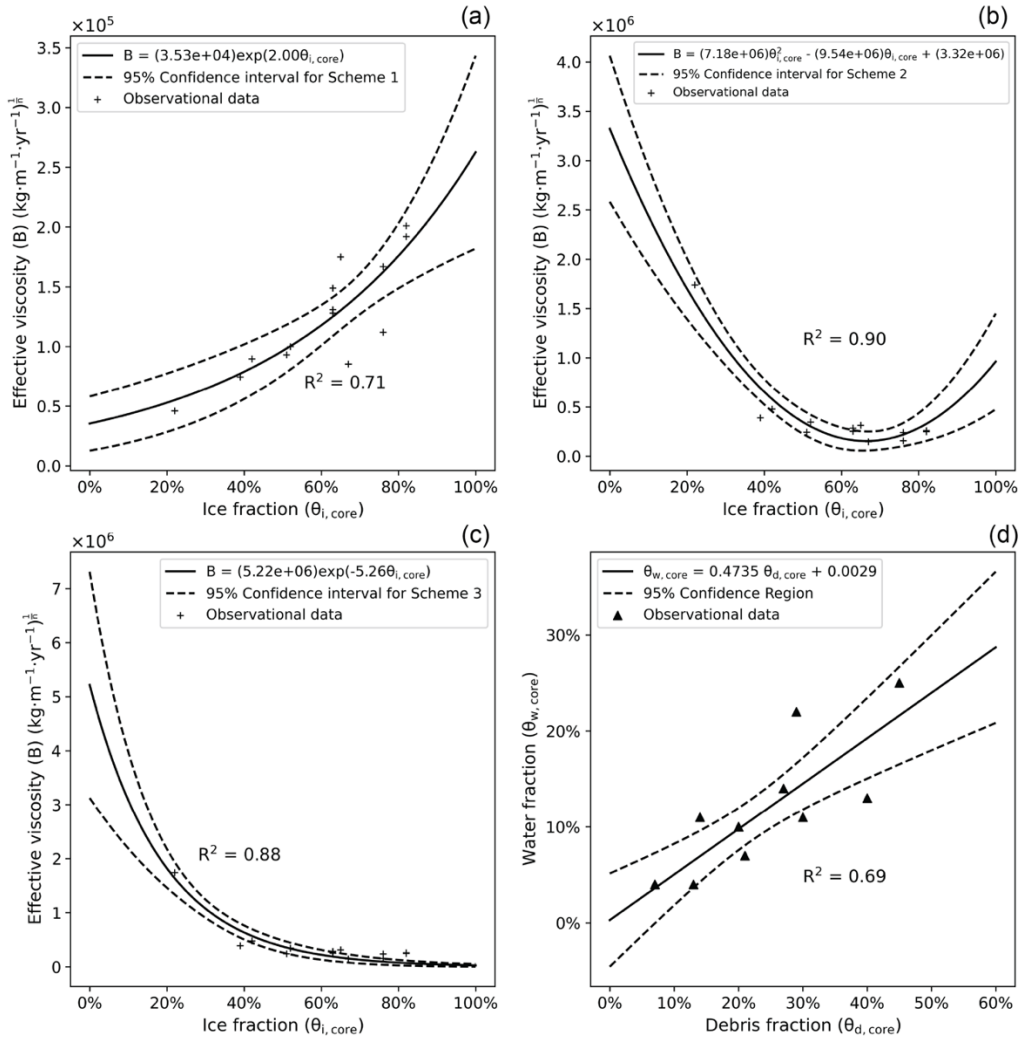


Figure 5.4 (a)–(c) Relationships between the ice fraction ($\theta_{i,\text{core}}$) and the effective viscosity (B) estimated from the three regression equations and parameterization schemes (Equations 5.14, 5.15, and 5.16, respectively). (d) Relationship between debris fraction ($\theta_{d,\text{core}}$) and water fraction ($\theta_{w,\text{core}}$). The observational data are derived from the GPR and DGPS measurements in Monnier and Kinnard (2015a).

5.3.3.2 Model validation

The three parameterization schemes (Equations 5.14–5.16) were validated using observational data of four rock glaciers in the Swiss Alps, namely Murt ñ-Corvatsch, Gruben, Muragl, and Schafberg (Arenson et al., 2002; Barsch et al., 1979; Cicoira et al., 2019a; Hoelzle et al., 1998). We simulated the surface velocity (u_s) of each rock glacier by varying volumetric ice content ($\theta_{i,\text{core}}$) of the permafrost core, and inferred its ice fraction by comparing the modelled velocity and the measured velocity from Terrestrial Geodetic Surveys (PERMOS, 2019). We then referred to the previously estimated ice content of the selected rock glaciers to validate our predicted results (Figure 5.7, Table 5.5).

To derive the input parameters, we first outlined the boundaries of the four rock glaciers, from which their shape and areal extent can be extracted. An empirical relationship established by

Brenning (2005a) was then applied to calculate the rock glacier thickness (T) from its areal extent (A_{rg}):

$$T = 50A_{rg}^{0.2}, \quad (5.17)$$

where the area (A_{rg}) is in km^2 . The width of each glacier was quantified as the width of its minimum envelop rectangle. We took the mean value of the active layer thickness obtained from borehole measurements in the PERMOS network as the input parameter h_{al} for each rock glacier. The surface slope (α) was calculated based on the SRTM DEM with a spatial resolution of 30 m. A detailed overview of the above parameters is in Table 5.2. The permafrost core thickness (h_{core}) can be obtained by subtracting h_{al} from the total thickness T calculated using Equation 5.17.

We assumed the volumetric ice content ($\theta_{i,core}$) of the permafrost core to be between 40% to 100%, considering the prerequisites of the modified ice-debris mixture flow law (Equation 5.3) that the debris fraction ($\theta_{d,core}$) should be less than the threshold (θ_{dc}) (Section 5.3.2.1). We varied the ice content ($\theta_{i,core}$) by 1% in each step to model the corresponding surface velocities (u_s). We fixed the air content in the permafrost core as 7.5%, which is a mean value of the air fraction in ice-rich permafrost samples (Arenson and Springman, 2005b). At near 0 °C, the volumetric content of water ($\theta_{w,core}$) displays a positive correlation with the debris fraction ($\theta_{d,core}$) (Monnier and Kinnard, 2016). Thus, we calculated the $\theta_{d,core}$ - $\theta_{w,core}$ correlation based on the data published in Monnier & Kinnard (2015) and assumed the constitution of the selected rock glaciers followed the same linear relationship (Figure 5.4d). The debris density (ρ_d) was given as 2450 kg/m^3 (Monnier and Kinnard, 2016). The density of air (ρ_a) is determined by the elevation of each rock glacier. The ice density (ρ_i) is 916 kg/m^3 and the water density (ρ_w) is 1000 kg/m^3 .

Table 5.2 Summary of the geometric and structural parameters used in the validation.

Rock glacier	Area (A_{rg}) (km^2)	Width (m)	(W) (m)	Active layer thickness (h_{al})	Surface slope (α) (°)
Murt d-Corvatsch	0.06487	29	3.0		16
Gruben	0.7422	47	2.0		10
Muragl	0.02666	24	4.5		12
Schafberg	0.02715	24	4.8		16

5.3.3.3 Sensitivity analysis

To explore how uncertainties of the input parameters contribute to the final output of the developed approach, we tested response of the model to varying input parameters by performing a series of synthetic sensitivity experiments. For these experiments, we simulated surface velocities of the rock glacier with varying ice fraction, and inferred the current ice content from the velocity constraint. Parameters explored here are detailed in Table 5.3. A reference scenario is set up with the parameters of Murt d-Corvatsch rock glacier and labelled as Sc-1.0. We designed eight scenarios extending from Sc-1.0, naming each scenario after a multiplication factor which indicates the ratio between the parameter in each scenario and that in the reference scenario; with the exception of two parameters, namely debris density (ρ_d) and debris fraction in the active layer ($\theta_{d,al}$), where we changed the upper or lower boundary of the value range to be consistent with the usual value range in reality. We performed the sensitivity experiments by varying one parameter at a time while keeping the other variables constant.

Table 5.3 Parameters of the sensitivity experiments. Scn-1.0 is the reference scenario which includes the parameters of Murt d-Corvatsch rock glacier. The other scenarios are designed by multiplying the reference value of each variable with the corresponding factor in their scenario labels.

Scenario	A_{rg} (km ²)	W (m)	α (°)	h_{al} (m)	ρ_d (kg/m ³)	$\theta_{d,al}$ (%)	$\theta_{a,core}$ (%)
Scn-0.2	0.01297	40	3.2	0.6	1450	13	1.5
Scn-0.4	0.02594	80	6.4	1.2	1700	26	3.0
Scn-0.6	0.03892	120	9.6	1.8	1950	39	4.5
Scn-0.8	0.05189	160	12.8	2.4	2200	52	6.0
Scn-1.0	0.06487	200	16	3.0	2450	65	7.5
Scn-1.2	0.07784	240	19.2	3.6	2700	72	9.0
Scn-1.4	0.09081	280	22.4	4.2	2950	79	10.5
Scn-1.6	0.10379	320	25.6	4.8	3200	86	12.0
Scn-1.8	0.11677	360	28.8	5.4	3450	93	13.5

5.3.3.4 Model application

We applied the validated model with the optimal parameterization scheme to infer ice contents of the coherently moving parts of five rock glaciers in the Khumbu and Lhotse Valleys. The geometric and structural data used as input parameters are detailed in Table 5.4. Area, width, and slope angle are quantified using the same method as described in Section 5.3.2.3. Active layer thickness is determined as the mean value over the extent of each rock glacier during 2006–2017 from the European Space Agency Permafrost Climate Change Initiative Product (ESA CCI) (Obu et al., 2020). The same empirical relation for calculating rock glacier

thickness as used in the validation procedure is adopted here to obtain the thickness parameter. The surface velocity constraint is the range of InSAR-derived downslope velocity during the observed period (Section 5.3.2.2); except for Tobuche RG where the abnormal value in 2015 is removed from the range (see Section 5.4.1 for details). Finally, we calculated the water volume equivalent to estimate the amount of water stored in rock glaciers by considering the inferred ice content, areal extent, and permafrost core thickness.

Table 5.4 Summary of the geometric and structural parameters used for inferring ice content of the coherently moving parts of rock glaciers in the study area.

Rock glacier	Area (km ²)	Width (m)	(W) (m)	Active layer thickness (h _{al})	Surface slope (α) (°)
Kala-Patthar	0.074	240	0.68		9
Kongma	0.077	300	0.83		13
Lingten	0.094	240	0.65		20
Nuptse	0.234	400	0.30		13
Tobuche	0.128	400	1.67		16

5.4 Results

In this section we first summarize the surface kinematic characteristics of rock glaciers in Khumbu and Lhotse Valleys measured by InSAR. Then we show the results of model validation and sensitivity experiments. Finally, we present the inferred ice contents and estimated water storage of rock glaciers in the study area.

5.4.1 InSAR-derived surface kinematics of rock glaciers

Figure 5.5 shows the time series of InSAR-derived surface velocities of the coherently moving parts of rock glaciers. We observe that the median and mean velocities of each landform have similar values, and both are capable of characterizing the kinematic status of the landforms. By selecting the mean velocity as the representative value, most rock glaciers, except for Tobuche, moved at a nearly stable rate, ranging from 5 cm yr⁻¹ to 30 cm yr⁻¹ during the observational period, with the largest standard deviation being 3.4 cm yr⁻¹ for Lingten. The maximum velocity represents the local extreme of downslope motion and was as high as 112.1±12.4 cm yr⁻¹ for Lingten during 2019/07/15–2019/08/26. Tobuche displays similar stable kinematic behavior before 2010, but had accelerated by more than four times from 14.9±0.2 cm yr⁻¹ to 81.4±2.4 cm yr⁻¹ since 2010. The maximum velocity was 181.0±57.4 cm yr⁻¹ for the period 2015/03/18–2015/03/22. However, the associated uncertainties during this period were high: the relative uncertainties of mean, median, and maximum velocity were 2.9%, 38.2%, and 31.7%, respectively. Therefore, the acceleration of Tobuche cannot be confidently revealed by our data. The extents of coherently moving parts of the five rock

glaciers are presented in Figure 5.6, with the average velocities derived from the interferograms obtained during the past several years.

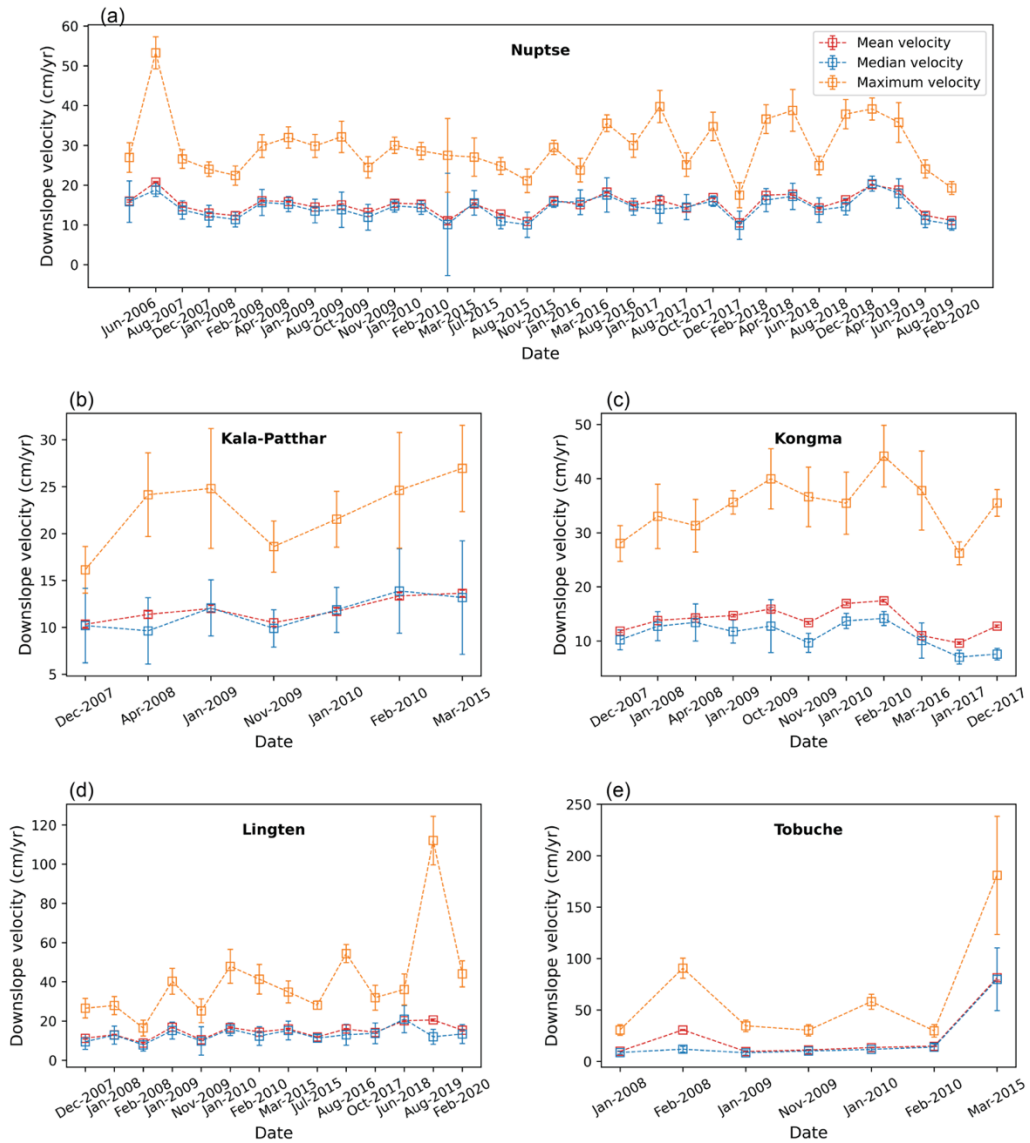


Figure 5.5 Time series of the InSAR-derived downslope velocities of the landforms. The spatial mean velocities and uncertainties during each period are shown (red squares and error bars) as well as the median (blue) and maximum (orange) velocities.

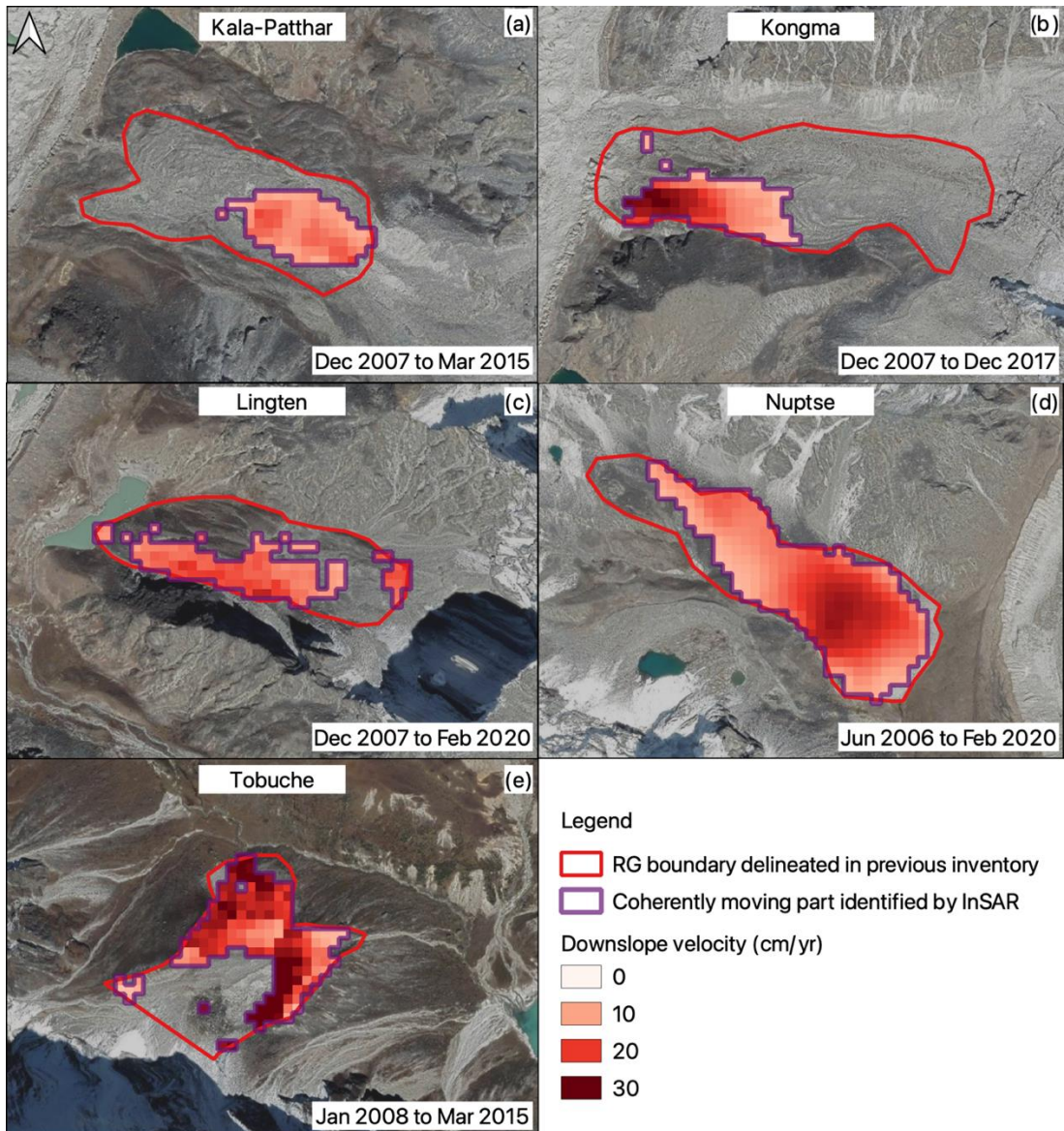


Figure 5.6 Velocity field maps show the average movement rate of the coherently moving parts of the five rock glaciers (purple outlines) in the study area. The boundaries of the landforms delineated in previous inventory work are in red polygons. The background is the Google Earth Images.

5.4.2 Model validation

With the input parameters and model setup as detailed in Section 5.3.2.3, we simulated the surface velocities (u_s) of each rock glacier using Schemes 1–3. Uncertainties generated through the statistical analysis used to establish the model (as shown in Figure 5.4), have all been considered in the simulation. We used the annual mean surface velocities calculate from the Terrestrial Ground Survey data (PERMOS, 2019), as the constraint for inferring the ice content.

For each rock glacier, an inferred ice content range is derived based on the velocity constraint and modelled u_s - $\theta_{i,core}$ relationship. The median of the range is selected as the inferred ice content and compared with the reference ice content (taken as the average value of the

estimated ice content based on previous field measurements; (Arenson et al., 2002; Barsch et al., 1979; Cicora et al., 2019a; Hoelzle et al., 1998).

Comparing the reference and inference ice content from the three schemes, Scheme 2 is the optimal one for the following two reasons: (1) the reference ice content is within the range inferred from Scheme 2 (Figure 5.8); (2) Scheme 2 gives the smallest average bias (8.4%) compared with Scheme 1 (12.9%) and Scheme 3 (13.3%) (Table 5.5). However, the above bias is not statistically useful for correcting the modelling results due to the limited amount of validation data.

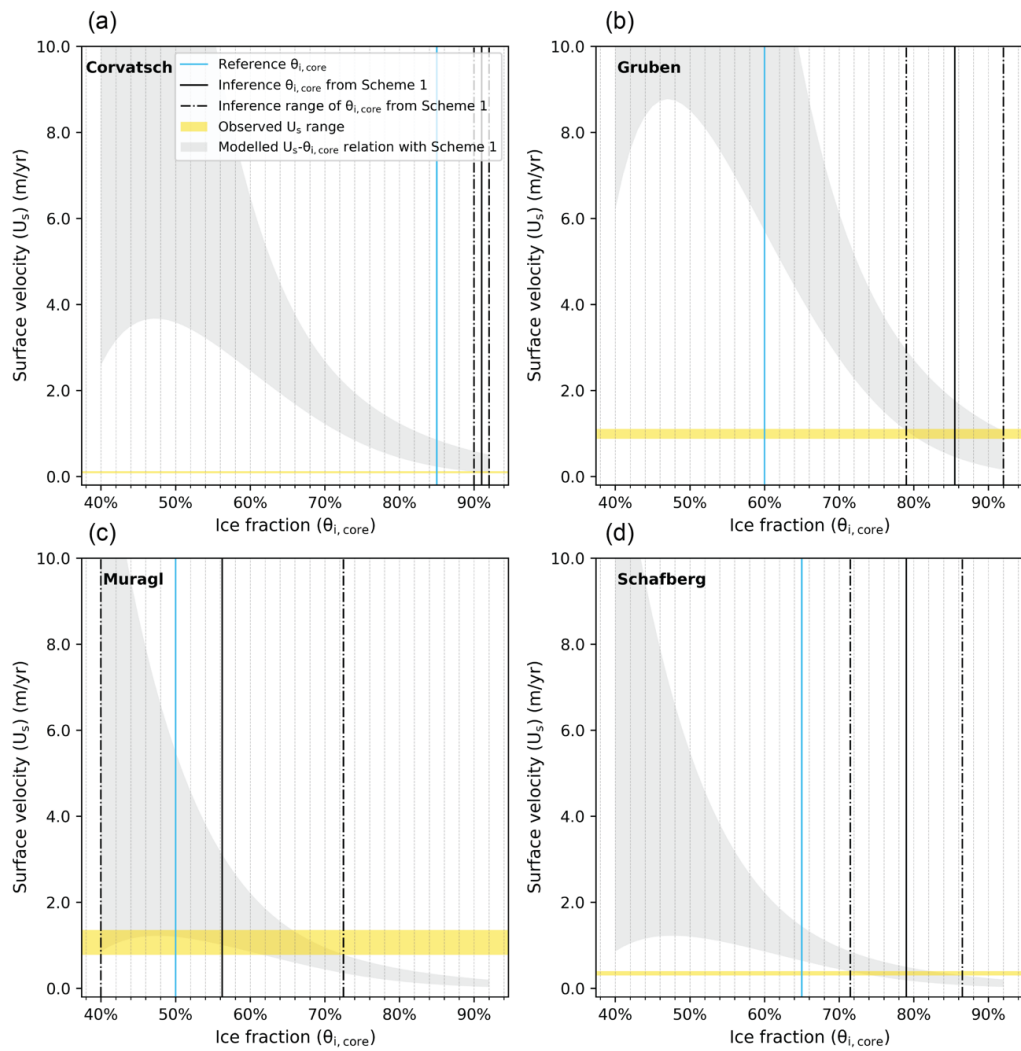


Figure 5.7 Modelled relationships (grey shaded areas) between the ice fraction ($\theta_{i,core}$) and the surface velocity (U_s) of 95% confidence intervals for the four RGs monitored in the PERMOS network with model parameterization Scheme 1. The ranges of the observed velocities (yellow bands) are used as velocity constraints for inferring ice content from the modelled relationships. Also shown are the reference ice content obtained from previous field-based surveys (blue lines). The inference ice contents are the mean values (solid black lines) with the estimated ranges (dash-dotted black lines).

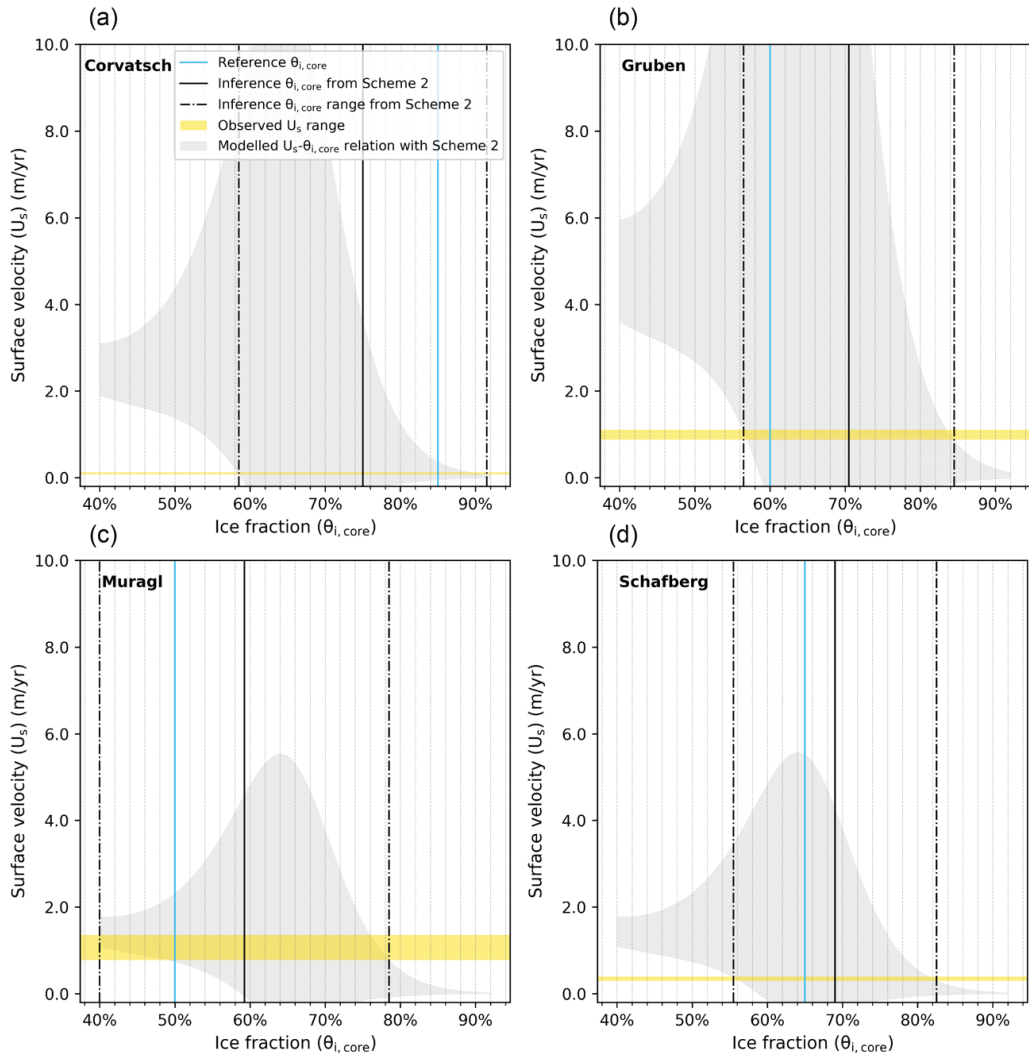


Figure 5.8 Similar to Figure 5.7, but showing results obtained based on model parameterization Scheme 2.

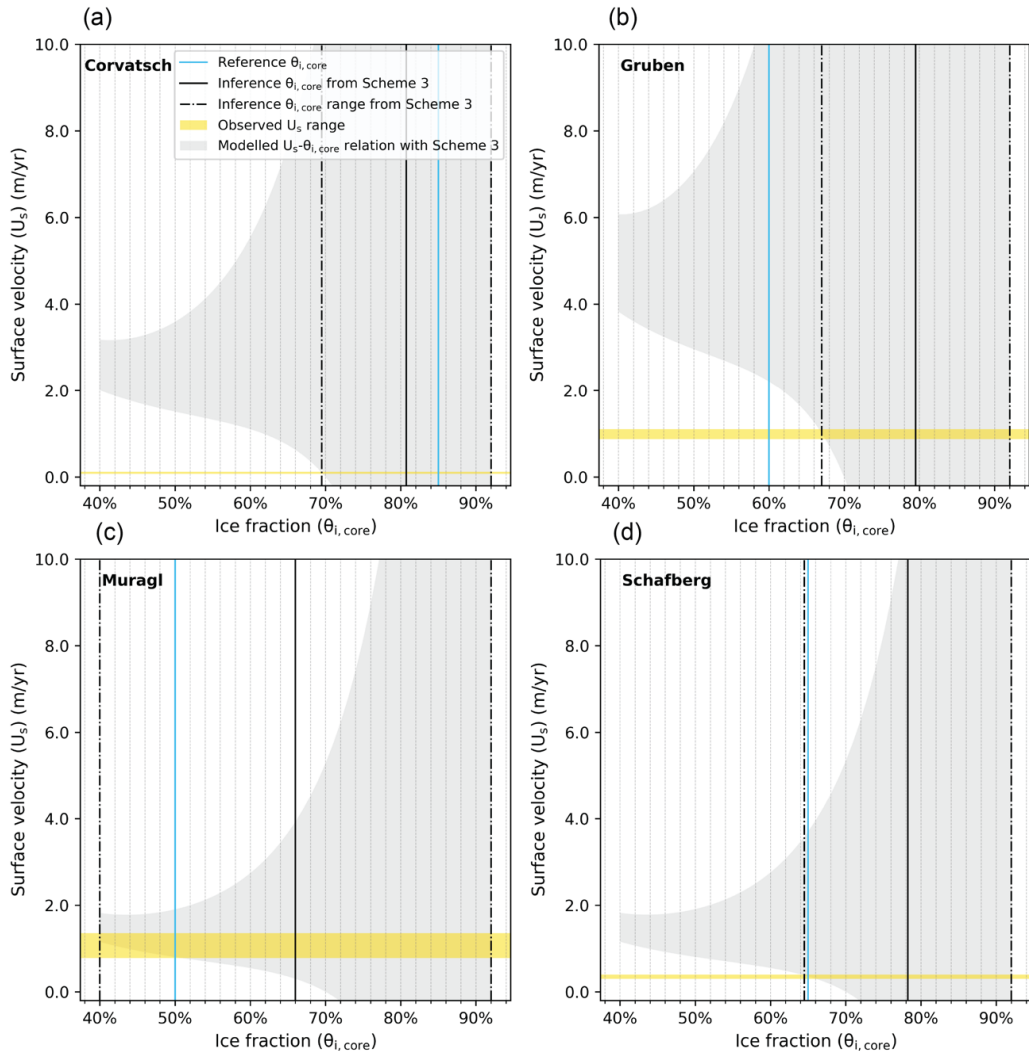


Figure 5.9 Similar to Figures 5.7 and 5.8, but showing results derived from model parameterization Scheme 3.

Table 5.5 Summary of the reference and inference ice contents derived from the three model parameterization schemes. The values in brackets following the inference ice contents give the corresponding bias from the reference ice contents.

Rock glacier	Referecne (%)	Inference and bias		
		Scheme 1(%)	Scheme 2 (%)	Scheme 3 (%)
Murt -Corvatsch	85	91 (7)	75 (-10)	81 (-4)
Gruben	60	85 (25)	71 (11)	80 (20)
Muragl	50	56 (6)	59 (9)	66 (16)
Schafberg	65	79 (14)	69 (4)	78 (13)
Mean bias		12.9	8.4	13.3

5.4.3 Model sensitivity

The results of sensitivity experiments are shown, normalized to the corresponding values of the reference scenario (Scn-1.0), in Figure 5.10. We observe that the inference result remains stable in response to most varying parameters, with a bias of less than 5%, relative to the reference scenario (Scn-1.0). Surface slope angle influences the result most: in the extreme scenario (Scn-0.2), the inferred ice content can be altered by 15%. In non-extreme cases (e.g., Scn-0.8, Scn-0.6), the influences of varying slope angles can be well constrained within the 5% range. In general, the model is insensitive to the uncertainties of any single input parameters.

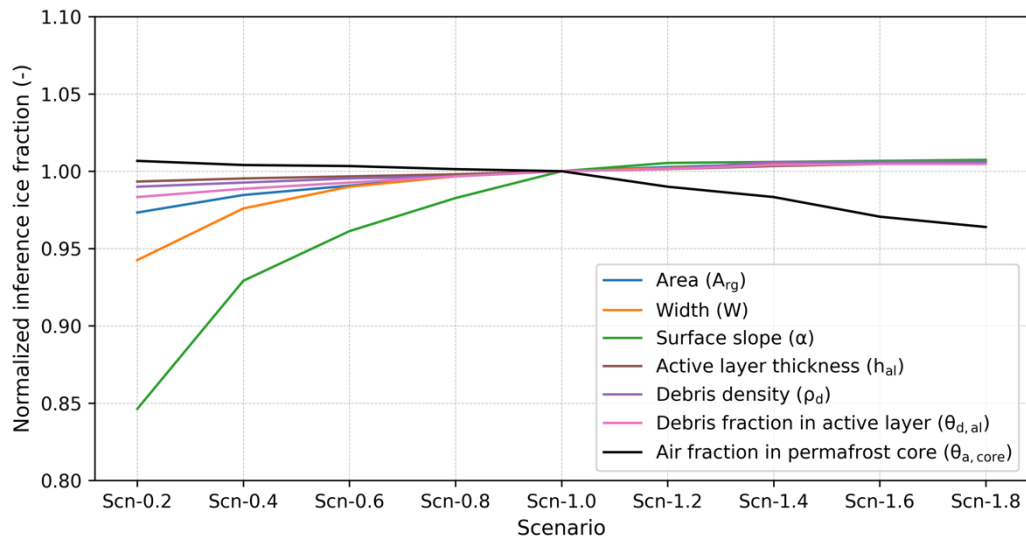


Figure 5.10 Normalized inference ice fractions from sensitivity experiments with the different parameter scenarios. The varying parameters include rock glacier area (blue line), width (orange line), surface slope (green line), active layer thickness (brown line), debris density (purple line), debris fraction in the active layer (pink line), and air fraction in permafrost core (black line).

5.4.4 Modelled ice contents

Figure 5.11 and Table 5.6 present the inference ice contents of rock glaciers in the study area. The inferred average ice fractions of the landforms are in the range of 71.0–75.3%; the water volume equivalent ranges from 1.40 to 5.92 million m³ for individual landforms. The maximum range of ice fraction is estimated to be 57.5–92.0%; the corresponding water volume equivalent ranges from 1.13 to 7.24 million m³. Nuptse stores the most ice by volume due to its largest dimensions. The total amount of water stored in the five rock glaciers lies between 10.61 and 16.54 million m³, with an average value of 13.57 million m³.

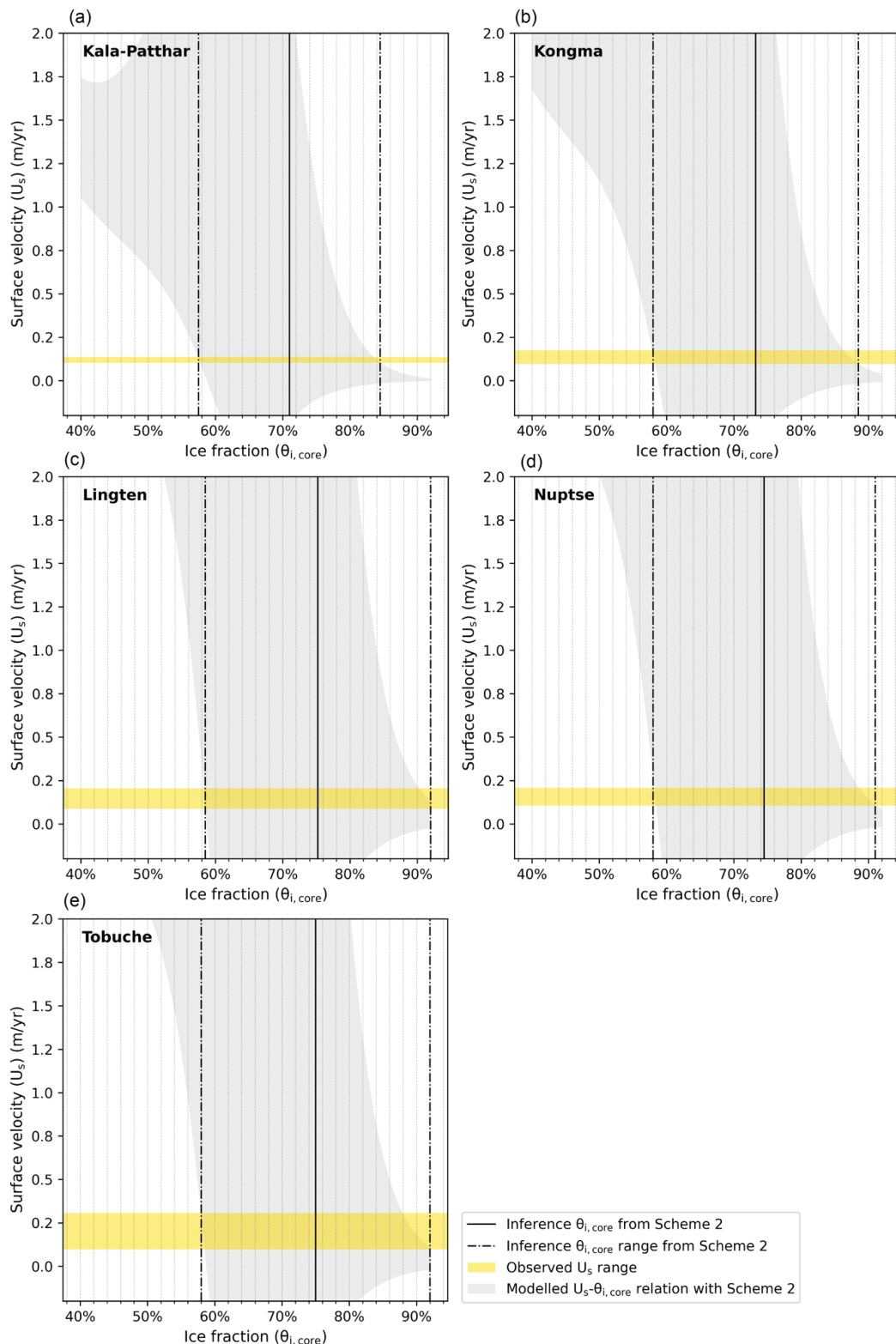


Figure 5.11 Modelled relationships between the ice fraction ($\theta_{i,\text{core}}$) and the surface velocity (U_s) of 95% confidence intervals for the five RGs in Khumbu Valley with model parameterization Scheme 2 (grey shaded areas). The ranges of the InSAR-derived velocities are shown (yellow bands), which are used as the velocity constraints for inferring ice contents from the modelled relationships. The upper and lower boundaries of the estimated ice contents are within the range outlined by the dash-dotted black lines and the solid black lines show the mean values representing the inference ice contents.

Table 5.6 Modelled average ice contents, as well as the minimum, and maximum estimates (in brackets) of rock glaciers in Khumbu and Lhotse Valleys and the corresponding water volume equivalents.

Rock glacier	Inference ice content (%)	Water volume equivalent (million m ³)
Kala-Patthar	71.0 (57.5–84.5)	1.40 (1.13–1.66)
Kongma	73.3 (58.0–88.5)	1.50 (1.19–1.82)
Nuptse	74.5 (58.0–91.0)	5.92 (4.61–7.24)
Lingten	75.3 (58.5–92.0)	1.98 (1.54–2.42)
Tobuche	75.0 (58.0–92.0)	2.77 (2.14–3.40)

5.5 Discussion

The following subsections firstly investigate the potential water storage of rock glaciers over the Nepalese Himalaya by extrapolating the estimated water storage in the Khumbu and Lhotse Valleys (Section 5.5.1). We then discuss the validity of the approach developed in this study for inferring ice content by analyzing the general assumptions and design of the surface-velocity-constrained model (Section 5.5.2), based upon which, we discuss the application of the method to large-scale regions and further improvements (Section 5.5.3).

5.5.1 Potential water storage in rock glaciers in the Nepalese Himalaya

The inferred average ice content of the five rock glaciers in the study area lies within a narrow range (71.0–75.3%), due to their similar observed downslope velocities (5–30 cm yr⁻¹), used as modelling constraints (Figure 5.5; Figure 5.6; Section 5.4.1). In general, rock glaciers typically creep at a rate ranging from decimeter to several meters per year (Delaloye and Echelard, 2020), thus the average ice content of the five rock glaciers may not be able to represent the motion of all rock glaciers situated in the entire mountain range.

Previous study has compiled an inventory including 4,226 intact rock glaciers over the Nepalese Himalaya, and a first-order estimate has indicated that these landforms contain between 16.72 and 25.08 billion m³ of water (Jones et al., 2018b). By extrapolating from the estimated water storage in the five rock glaciers found in this study, the total amount of water stored in all the intact rock glaciers ranges from 8.97 to 13.98 billion m³ over the entire mountain range, which is in the same magnitude predicted by the previous research (Jones et al., 2018b). In Nepalese Himalaya, the ratio between the amount of water stored in rock glaciers (11.47 billion m³) and in ice glaciers (197.63 billion m³) is 1:17. By using the minimum and maximum inference values, the estimated ratio ranges between 1:21 and 1:13. Our modelling-based results are lower than earlier estimates (1:9), yet reveal higher hydrological importance than across the Himalayas (1:24) (Jones et al., 2018b; Jones et al., 2021).

5.5.2 Validity of general assumptions and model design

Our aim was to develop a rheological model that allows for inferring ice content of rock glaciers in areas where in-situ investigations are scarce. To achieve this objective, certain simplifications have been applied to the model setup. Here we discuss the validity of the method through the following six aspects of the model assumptions and design, including (1) assumption of a steady-state rock glacier creep; (2) homogeneous warm permafrost hypothesis; (3) neglect of shear horizon in the model design; (4) accuracy of rock glacier thickness derivation; (5) identification of the coherently moving part of rock glaciers; and (6) generalization of statistical relationships derived from Las Liebres rock glacier.

5.5.2.1 Steady-state creep of rock glaciers

By using the adapted form of Glen's flow law (Equation 5.2), we primarily assume the rock glacier movement to be steady-state creep driven by viscoelastic deformation of the ice-debris mixture (Moore, 2014). This premise indicates that our method is applicable to rock glaciers currently moving at a relatively stable rate. Recent research has reported abrupt and significant acceleration of rock glaciers triggered by abnormal surface warming events (Delaloye et al., 2013). These destabilized rock glaciers are beyond the applicability of our method. In this study, we quantified surface kinematics of rock glaciers over multiple years to quantify the stability of the rock glacier motion. The seasonal variation in creep rate is neglected and sudden acceleration events are excluded in the velocity range used as the model constraint (Section 5.4.1).

We also exclude the component of basal sliding processes in our model design (Figure 5.3), which operates at the base of some rock glaciers as observed in the Tien Shan (Harrison unpubl.). This is not surprising; many clean ice glaciers undergo basal sliding in certain situations (e.g., Vivian and Bocquet, 1973) although, more generally a debris-rich layer with high water content at the base undergoes enhanced deformation and some sliding (e.g., Boulton and Jones, 1979; Echelmeyer and Wang, 1987). This process also occurs in rock glaciers with a high ice content and is accompanied by the disruption of sediment and vegetation at the front of such features. Kinematics of these rock glaciers cannot be appropriately simulated by the current approach.

5.5.2.2 Homogeneous warm permafrost

Ground temperature is one of the factors controlling the creep parameter (A) (Equation 5.1), as described by the Arrhenius relation (Mellor and Testa, 1969). As ground temperature changes with depth, primarily due to heat diffusion, creep parameter (A) varies along the vertical profile of the rock glacier. Previous studies implemented different relationships

between creep parameter and temperature, and integrated a heat diffusion model (proposed by Carslaw and Jaeger, 1959) to consider this effect (Arenson and Springman, 2005a; Azizi and Whalley, 1996; Käab et al., 2007; Ladanyi, 2003).

In our model design, we use the effective viscosity (B) to absorb the intricate effects of strain enhancement factor (E), threshold stress (τ_{th}), and most importantly, the creep parameter (A) (Equation 5.3), which reduces the number of input parameters and allows for developing an empirical relationship between effective viscosity and ice content based on an existing observational dataset and laboratory findings (Equation 5.13). The data and relationship between variables we used for model calibration are derived from observations of rock glaciers situated in a warm permafrost environment (>-3 °C) (Arenson and Springman, 2005a; Monnier and Kinnard, 2016)

Measurements of ground temperature in the study area are scarce in general. However, we infer that these rock glaciers develop in a warm permafrost environment for the following reasons: (1) the landforms are located near or below the altitudinal limit of permafrost distribution in Nepal (Section 5.2) (Fujii and Higuchi, 1976; Jakob, 1992), indicating that the local environment is at the critical condition of permafrost occurrence; (2) based on empirical relationships between mean annual ground temperature (MAGT), mean annual air temperature latitude, and altitude, the estimated MAGT is >0.5 °C, which suggests that permafrost in this area is in a warm and unstable condition (Nan et al., 2002; Zhao and Sheng, 2015).

5.5.2.3 Neglect of shear horizon

The shear horizon is discovered from borehole investigations and is defined as the thin layer situated at more than ten meters deep where the majority of internal deformation takes place (Arenson et al., 2002; Buchli et al., 2018; Haeberli et al., 1998). Field observations and numerical modelling suggest that unfrozen water within the shear horizon plays an important role in controlling the seasonal variations in rock glacier creep (Buchli et al., 2018; Cicoira et al., 2019b; Kenner et al., 2019). This short-term feature of rock glacier kinematics is insignificant to modelling the relationship between ice content and multi-annual average movement velocity in our study.

Previous studies have considered the enhanced deformation occurring in the shear horizon additionally, but it requires detailed knowledge of the internal structure; i.e., the depth of shear horizon (Frehner et al., 2015; Ladanyi, 2003). To tackle the issue of data insufficiency of internal rock glacier structure in this study area – as with most permafrost areas – we neglect the distinct rheology in the shear horizon and assume a constant effective viscosity instead.

This simplification has also been adopted in other research aiming at studying rock glacier dynamics over a large-scale extent (Cicoira et al., 2020).

5.5.2.4 Accuracy of rock glacier thickness derivation

The accuracy of rock glacier thickness is discussed here because it influences the surface kinematics most significantly. As shown in Equation 8, the surface velocity is proportional to the thickness to the power of $n + 1$, resulting from the vertical integration of Equation 5.7. We adopt the empirical relationship between rock glacier area and thickness (Equation 5.17) based on field observations in the Andes (Brenning, 2005b). The derived thicknesses of the four rock glaciers in the Swiss Alps, used for validation are consistent with previous in-situ measurements. However, another rock glacier, namely Ritigraben, situated in the same region, does not follow this empirical relationship, and has a bias as large as ten meters compared with the field estimates. We also test a linear relationship between surface slope angle and thickness, recently established by Cicoira et al. (2020). The accuracies of the results turn out to be at the same level, with four out of five rock glaciers having good estimation results (Table 5.7). Thus, the uncertainty introduced by thickness derivation when applied to rock glaciers without known information of structure is unavoidable.

Table 5.7 Estimated rock glacier thickness derived from the thickness-area relationship used in this study (T_{area}) (Equation 17), and the corresponding bias relative to in-situ measured thickness (Arenson et al., 2002; Barsch et al., 1979; Cicoira et al., 2019a; Hoelzle et al., 1998). The rock glacier thickness derived from slope angle (T_{slp}) proposed by Cicoira et al. (2020), and the associated bias.

Rock glacier	T_{area} and bias (m)	T_{slp} and bias (m)	T_{ref} (m)
Murtal-Corvatsch	29 (2)	26.2 (-0.8)	27
Gruben	47 (-3)	28 (-22)	50
Muragl	24 (4)	19 (-1)	20
Schafberg	24 (-1)	20.8 (-4.2)	25
Ritigraben	28 (10)	12.7 (-5.3)	18

5.5.2.5 Identification of the coherently moving part of rock glaciers

Taking advantage of the multi-temporal observations and continuous spatial coverage of the InSAR measurements, we define the coherently moving part of each rock glacier in our study area (Figure 5.6; Section 5.3.1), and infer the ice content of the coherently moving part using the developed modelling approach. We introduce this concept because it corresponds with the general model setup (Figure 5.3). Moreover, with the assistance of displacement maps generated by InSAR, the defined boundary of coherently moving rock glacier avoids the ambiguities involved when delineating rock glaciers solely based on geomorphologic features from a highly dynamic environment where complex glacial, periglacial, and paraglacial

processes take place (Delaloye and Echelard, 2020; Jones et al., 2019a). In addition, defining the coherently moving part associates with the uncertainty in rock glacier area, which is unlikely to affect the modelling result significantly due to the insensitive response of our model to this input parameter (Figure 5.10). Finally, employing this kinematics-based definition, may also contribute to the currently inevitable uncertainties in thickness estimation (Section 5.5.2.4), as Equation 5.17 (proposed by Brenning, 2005a) uses rock glacier area as a variable without considering the landform activity.

5.5.2.6 Generalization of statistical relationships derived from Las Liebres rock glacier

The model we developed in this study essentially relies on the statistical relationships, especially the effective viscosity-ice content relationship, derived from geophysical surveys conducted on Las Liebres rock glacier in the Andes (Monnier and Kinnard, 2015a). Applying the calibrated model to rock glaciers in other areas is primarily based on the assumption that a common flow law governs the rheology of rock glaciers developed in warm permafrost environment, irrespective of locality. In addition to the general hypothesis, we tackled this issue in two ways. First, we validated the model using samples from a different region, i.e., the Swiss Alps (Section 5.3.2.3). Secondly, the uncertainties introduced by the statistical analysis have all been quantified in the validation and inference procedures, which leads to a wide range of inference ice contents (Sections 5.3.2.3 and 5.4.4).

5.5.3 Application of the model and outlook

By adopting the assumptions and setups as discussed in Section 5.5.2, we firstly present an approach for estimating ice content of rock glaciers with simple input parameters; including the planar shape (area and width), surface slope angle, active layer thickness, and surface velocity, all of which can be obtained directly or derived from remote sensing techniques and products. Therefore, this established method for estimating the amount of ice stored in numerous rock glaciers with well-quantified uncertainties is ready to be applied to many remote alpine environments.

To improve the performance of the approach, more data obtained from field and geophysical investigations, especially detailed data of rock glacier composition, can be integrated in the future to calibrate and validate the empirical rheological model. More reliable methods for estimating rock glacier thickness will also improve the accuracy of the modelling results.

5.6 Conclusions

We develop an empirical rheological model for inferring ice content of rock glaciers and apply it to estimate the water storage of rock glaciers situated in the Khumbu and Lhotse Valleys

using surface-velocity-constraints derived from InSAR measurements. The main findings are summarized as follows:

- (1) An empirical rheological model is presented in this study for estimating ice content of rock glaciers using five input parameters, namely rock glacier area, width, surface slope angle, active layer thickness, and surface velocity, all of which can be obtained from readily available remote sensing products or emerging datasets.
- (2) Mean downslope velocities of the rock glaciers situated in Khumbu and Lhotse Valleys ranged from 5 cm yr^{-1} to 30 cm yr^{-1} and mostly remained stable during the observational period (2006–2020).
- (3) The inferred average ice content of rock glaciers in Khumbu Valley are in the range of 71.0–75.3%; the water volume equivalent ranges from 1.40 to 5.92 million m^3 for individual landforms. Nuptse RG stores the most ice due to its largest dimensions among the five studied rock glaciers.
- (4) The inference range of ice content of the landforms lies between 57.5 and 92.0%. Total amount of water stored in the five rock glaciers in Khumbu Valley ranges from 10.61 to 16.54 million m^3 , with an average value of 13.57 million m^3 .
- (5) Considering previous estimates and extrapolating from our inference results in Khumbu Valley, the total amount of water stored in rock glaciers over the Nepalese Himalaya is in the magnitude of 10 billion m^3 , and the ratio between water storage in rock glaciers and ice glaciers ranges from 1:13 to 1:21, averaging at 1:17.

This study demonstrates the effectivity of inferring ice content of rock glaciers by using a surface-velocity-constrained model. The estimated ice content and water storage in the study area highlights the hydrological significance of rock glaciers in Nepalese Himalaya. The approach developed here can be readily applied to other alpine permafrost regions where rock glaciers are widespread for a preliminary water resource evaluation.

Chapter 6 Conclusion and outlook

*“Nothing in life is to be feared, it is only to be understood.
Now is the time to understand more, so that we may fear less.”
—Marie Curie*

In this chapter, we first recapitulate the main research findings by responding to the three key scientific questions raised at the beginning of the thesis. Then we summarize the innovative merits and potential impacts of this work. Finally, we conclude the thesis by presenting our perspectives on the future research paths based on the current studies of rock glaciers on the Tibetan Plateau.

6.1 Conclusion

This thesis pursues the research objectives (Sect. 1.1) by extending knowledge of rock glaciers on the Tibetan Plateau in three aspects: (1) we resolve the long-standing dispute over rock glacier definition and classification on the plateau by combining geomorphologic and kinematic methods. (2) we map rock glaciers across the West Kunlun Mountains based on InSAR and deep learning and document their geomorphic and kinematic attributes. (3) we infer ground ice content stored in rock glaciers in a valley of Nepalese Himalaya from remotely sensed data of landform geometry and kinematics using an empirical rheological model. The main findings are summarized to address the three research questions as follows:

Research Question I: What type of landform is a puzzling periglacial lobe at the Kunlun Pass?

Response: It is a debris-mantled slope-connected rock glacier with gelifluction processes superimposed as discrete and local events.

We draw the conclusion from observing the geomorphic characteristics of the landform and analyzing its dynamic variations in surface movement quantified by InSAR. The developed frontal and lateral margins are essential rock glacier features according to the latest consensus achieved on rock glacier definition among the IPA Rock Glacier Action Group. The landform-scale, spatially uniform, seasonally rhythmed, and relatively fast motion indicates a permafrost creep process occurring at depth, which corroborates the geomorphologic identification from the kinematic perspective.

Research Question II: What is the distribution and kinematic status of rock glaciers in West Kunlun Mountains?

Response: We identify and map 413 rock glaciers, situated at altitudes between 3389 m and 5541 m. There are 256 active rock glaciers with valid kinematic quantifications. The mean and maximum surface downslope velocities are 24 cm yr^{-1} and 127 cm yr^{-1} , respectively.

We develop an approach for mapping rock glaciers at a regional scale semi-automatically and quantifying their surface kinematics by combining InSAR and image semantic segmentation powered by deep learning. The combined method is applied to compile the first rock glacier inventory across the West Kunlun Mountains. The inventory classifies the rock glaciers by their spatial connection to the upslope units into four types, namely the glacier-connected (G-RGs), the debris-mantled slope-connected (DMS-RGs), the glacier forefield-connected (GF-RGs), and the talus-connected (T-RGs). Among the 413 mapped rock glaciers, there are 202 G-RGs, 143 DMS-RGs, 41 GF-RGs, and 27 T-RGs. Nearly 90% of the 256 active rock glaciers move at a rate slower than 50 cm yr^{-1} . The G-RGs and GF-RGs move faster at mean velocities of 31 cm yr^{-1} and 35 cm yr^{-1} , respectively. The DMS-RGs and T-RGs creep at a slower average rate of 17 cm yr^{-1} .

Research Question III: How much ground ice is stored in rock glaciers?

Response: Among five rock glaciers situated in Nepalese Himalaya, their average volumetric ice contents are inferred to range from 71% to 75.3% by using an empirical rheological model. The total water volume equivalent in the study area lies between 10.61 and 16.54 million m^3 .

We develop an empirical rheological model for estimating ice content of rock glaciers using remotely sensed input data, including rock glacier geometric parameters and surface kinematics derived from InSAR. We apply the model to infer ice storage in five rock glaciers situated in northeastern Nepal and extrapolate the inference results to the Nepalese Himalaya. We find that the total amount of water stored in rock glaciers over the entire mountain range is in the magnitude of 10 billion m^3 , and the ratio between water storage in rock glaciers and glaciers ranges from 1:13 to 1:21, averaging at 1:17.

6.2 Innovative merits and potential impacts

This thesis focuses on rock glacier kinematics and takes a step forward towards integrating this parameter as a proxy for studying permafrost on the Tibetan Plateau. Chapter 3 and 4 present two studies aiming to address the fundamental problems, such as the basic concepts and inventory compilation strategy, which hinder further insights gained from the knowledge of rock glacier kinematics on the plateau. Chapter 5 explores the potential to adopt rock glacier kinematics as a proxy for inferring ground ice content.

In summary, the innovative merits and potential impacts of this thesis consist of four parts:

- (1) We have obtained insights into the periglacial processes operating on rock glaciers by critically analyzing the surface kinematics measured by InSAR. It has provided a novel perspective that improves the understanding of periglacial geomorphology and illustrates the diversity and intricacy of rock glaciers on the Tibetan Plateau.
- (2) We have developed a deep-learning-based method to automate the identification and delineation of rock glaciers from remote sensing imagery. The new method has allowed for inventorying rock glaciers in an efficient and consistent way over the vast permafrost regions on the plateau.
- (3) We have provided data of InSAR-derived rock glacier surface velocities to improve the previously limited records of rock glacier kinematics on the Tibetan Plateau. The new dataset has increased the knowledge of current kinematic status of rock glaciers on the plateau and laid foundation for reconstructing long-term time series of rock glacier kinematics in the past and monitoring spatial and temporal changes in the future.
- (4) We have presented an empirical rheological model for quantitatively estimating ice content of rock glaciers with readily available input parameters including InSAR-derived surface kinematics. It is the first modelling method for quantifying ground ice stored in rock glaciers and it is promising to be applied to permafrost regions where rock glaciers are widespread for a preliminary water resource evaluation.

6.3 Future research

New research paths towards a better understanding of rock glacier kinematics on the Tibetan Plateau have emerged out of the studies conducted for approaching the three initial scientific questions. Here we document four aspects of future research closely relevant to this thesis as follows:

- (1) Compile a comprehensive and standard inventory of rock glaciers over the Tibetan Plateau using deep learning. We will increase the size of training dataset and improve the performance of the automated mapping method. The output inventory will serve as a baseline dataset for monitoring the degrading permafrost and evaluating ground ice storage in rock glaciers over the plateau, which is one of most sensitive areas to climatic warming.
- (2) Reconstruct multi-decadal variations in surface kinematics of selected rock glaciers using InSAR and optical images. We will derive the response of rock glacier kinematics to climatic forcing, which will offer insights into both the spatial and temporal patterns of permafrost changes on the plateau during the reconstructed period. We will also compare the rock glacier response with the variations in other permafrost ECVs (e.g., active layer thickness) and

cryospheric components (e.g., glacier mass balance and glacier lake extent) to form an overall understanding of the cryosphere changes in the Third Pole.

(3) Study the environmental interactions between the short-term (e.g., a few days to seasonal) kinematic variations of rock glaciers and the meteorological factors in various climatic zones, such as the arid West Kunlun. Current knowledge of the rock glacier short-term dynamic response to environmental factors is mainly acquired from observations and modelling work conducted in the European Alps (Cicoira et al., 2019b; Kenner et al., 2019; Müller et al., 2016; Wirz et al., 2016b). However, climatic conditions on the plateau significantly differ from that in the Alps, especially regarding the precipitation rate which is considered to be the controlling factor to seasonal rhythm of rock glacier dynamics. Such comparison will increase our understanding of the controlling mechanism of environmental variables on rock glacier kinematics.

(4) Calibrate the ground ice model with more in situ data to improve the model accuracy. We will collect more data of rock glacier composition from geophysical surveys and borehole observations, especially from rock glaciers on the Tibetan Plateau. The better calibrated model will be applied to assess the potential water storage in rock glaciers with reference to the plateau-wide inventory.

Abbreviations

3D	Three Dimensional
a.s.l.	above sea level
ALS	Airborne Laser Scanning
BCF	Bulk Creep Factor
CNN	Convolutional Neural Network
CRS	Cryospheric Research Station
DEM	Digital Elevation Model
DGPS	Differential Global Positioning System
DMS-RG	debris-mantled slope-connected rock glacier
DSM	Digital Surface Model
DTM	Digital Terrain Model
ECV	Essential Climate Variable
ESA CCI	European Space Agency Permafrost Climate Initiative Product
ESRI	Environmental Systems Research Institute
FN	False Negative
FP	False Positive
G-RG	glacier-connected rock glacier
GACOS	Generic Atmospheric Correction Online Service
GCOS	Global Climate Observing System
GF-RG	glacier forefield-connected rock glacier
GLIMS	Global Land Ice Measurements from Space
GST	Ground Surface Temperature
HCO	Holocene Climatic Optimum
InSAR	Interferometric Synthetic Aperture Radar
IoU	Intersection over Union
IPA	International Permafrost Association
ISCE	InSAR Scientific Computing Environment
LiDAR	Light Detection and Ranging
LOS	Line-of-Sight
MAAT	Mean Annual Air Temperature
MAGST	Mean Annual Ground Surface Temperature
MAGT	Mean Annual Ground Temperature
MWP	Medieval Warm Period
PERMOS	The Swiss Permafrost Monitoring Network
QTP	Qinghai-Tibet Plateau
RPAS	Remotely Piloted Aircraft System
SAA	Shape Accel Array
SBAS	Small Baseline Subset
SfM-MVS	Structure from Motion-Multiview Stereo
SRTM	Shuttle Radar Topography Mission
T-RG	talus-connected rock glacier
TLS	Terrestrial Laser Scanning
TP	True Positive
UAV	Unmanned Aerial Vehicle
WGS	World Geodetic System

Bibliography

- Amschwand, D., Ivy-Ochs, S., Frehner, M., Steinemann, O., Christl, M., and Vockenhuber, C. (2021). Deciphering the evolution of the Bleis Marscha rock glacier (Val d'Err, eastern Switzerland) with cosmogenic nuclide exposure dating, aerial image correlation, and finite element modeling. *The Cryosphere*, 15(4), 2057-2081. <https://doi.org/10.5194/tc-15-2057-2021>
- Andersland, O. B., and Ladanyi, B. (2003). *Frozen ground engineering*. John Wiley & Sons.
- Anderson, R. S., Anderson, L. S., Armstrong, W. H., Rossi, M. W., and Crump, S. E. (2018). Glaciation of alpine valleys: The glacier – debris-covered glacier – rock glacier continuum. *Geomorphology*, 311, 127-142. <https://doi.org/10.1016/j.geomorph.2018.03.015>
- Arenson, L., Hoelzle, M., and Springman, S. (2002). Borehole deformation measurements and internal structure of some rock glaciers in Switzerland. *Permafrost and Periglacial Processes*, 13(2), 117-135. <https://doi.org/https://doi.org/10.1002/ppp.414>
- Arenson, L., and Springman, S. (2005a). Mathematical descriptions for the behaviour of ice-rich frozen soils at temperatures close to 0 °C. *Canadian Geotechnical Journal*, 42(2), 431-442. <https://doi.org/https://doi.org/10.1139/t04-109>
- Arenson, L., and Springman, S. (2005b). Triaxial constant stress and constant strain rate tests on ice-rich permafrost samples. *Canadian Geotechnical Journal*, 42(2), 412-430. <https://doi.org/https://doi.org/10.1139/t04-111>
- Arenson, L. U., Hauck, C., Hilbich, C., Seward, L., Yamamoto, Y., and Springman, S. M. (2010). Sub-surface Heterogeneities in the Murtal: Corvatsch Rock Glacier, Switzerland. Proceedings of the joint 63rd Canadian Geotechnical Conference and the 6th Canadian Permafrost Conference,
- Arenson, L. U., Käb, A., and O'Sullivan, A. (2016). Detection and Analysis of Ground Deformation in Permafrost Environments. *Permafrost and Periglacial Processes*, 27(4), 339-351. <https://doi.org/https://doi.org/10.1002/ppp.1932>
- Arenson, L. U., Springman, S. M., and Sego, D. C. (2007). The rheology of frozen soils. *Applied Rheology*, 17(1), 12147-12141-12147-12114.
- Avian, M., Kaufmann, V., and Lieb, G. (2005). Recent and Holocene dynamics of a rock glacier system: The example of Langtalkar (Central Alps, Austria). *Norwegian Journal of Geography*, 59(2), 149-156. <https://doi.org/10.1080/00291950510020637>
- Avian, M., Kellerer-Pirkbauer, A., and Bauer, A. (2009). LiDAR for monitoring mass movements in permafrost environments at the cirque Hinteres Langtal, Austria, between 2000 and 2008. *Nat. Hazards Earth Syst. Sci.*, 9(4), 1087-1094. <https://doi.org/10.5194/nhess-9-1087-2009>
- Azizi, F., and Whalley, W. B. (1996). Numerical modelling of the creep behaviour of ice-debris mixtures under variable thermal regimes. *International Offshore and Polar Engineering Conference Proceedings* The Sixth International Offshore and Polar Engineering Conference, Los Angeles.
- Azócar, G. F., and Brenning, A. (2010). Hydrological and geomorphological significance of rock glaciers in the dry Andes, Chile (27°-33°S). *Permafrost and Periglacial Processes*, 21, 42-53. <https://doi.org/https://doi.org/10.1002/ppp.669>
- Ballantyne, C. K. (2018). *Periglacial geomorphology*. John Wiley & Sons.
- Bao, W.-j., Liu, S.-y., Wei, J.-f., and Guo, W.-q. (2015). Glacier changes during the past 40 years in the West Kunlun Shan. *Journal of Mountain Science*, 12(2), 344-357.

BIBLIOGRAPHY

- Baral, P., Haq, M. A., and Yaragal, S. (2020). Assessment of rock glaciers and permafrost distribution in Uttarakhand, India. *Permafrost and Periglacial Processes*, 31(1), 31-56. <https://doi.org/https://doi.org/10.1002/ppp.2008>
- Barboux, C., Bertone, A., Bodin, X., Delaloye, R., Rouyet, L., and Strozzi, T. (2020). *Kinematics as an optional attribute in standardized rock glacier inventories: version 2.1.* https://bigweb.unifr.ch/Science/Geosciences/Geomorphology/Pub/Website/IPA/Guidelines/KinematicsAttribute/200429_KinematicsAttribute_V2.1.pdf
- Barboux, C., Delaloye, R., and Lambiel, C. (2014). Inventorying slope movements in an Alpine environment using DInSAR. *Earth Surface Processes and Landforms*, 39(15), 2087-2099. <https://doi.org/10.1002/esp.3603>
- Barsch, D. (1971). Rock glaciers and Ice-cored moraines. *Geografiska Annaler: Series A, Physical Geography*, 53(3-4), 203-206. <https://doi.org/10.1080/04353676.1971.11879846>
- Barsch, D. (1996). *Rockglaciers : indicators for the present and former geoecology in high mountain environments.* Springer-Verlag.
- Barsch, D., Fierz, H., and Haeberli, W. (1979). Shallow core drilling and borehole measurements in the permafrost of an active rock glacier near the Grubengletscher, Wallis, Swiss Alps. *Arctic and Alpine Research*, 11(2), 215-228. <https://doi.org/https://doi.org/10.2307/1550646>
- Barsch, D., and Hell, G. (1975). Photogrammetrische Bewegungsmessungen am Blockgletscher Murt à I, Oberengadin, Schweizer Alpen. *Z Gletscherk Glazialgeol*, 11, 111–142.
- Bauer, A., Paar, G., and Kaufmann, V. (2003). *Terrestrial laser scanning for rock glacier monitoring* Proceedings of the 8th International Permafrost Conference, Zurich, Balkema.
- Berthling, I. (2011). Beyond confusion: Rock glaciers as cryo-conditioned landforms. *Geomorphology*, 131(3-4), 98-106. <https://doi.org/https://doi.org/10.1016/j.geomorph.2011.05.002>
- Berthling, I., Etzelmüller, B., Eiken, T., and Sollid, J. L. (1998). Rock glaciers on Prins Karls Forland, Svalbard. I: internal structure, flow velocity and morphology. *Permafrost and Periglacial Processes*, 9(2), 135-145. [https://doi.org/https://doi.org/10.1002/\(SICI\)1099-1530\(199804/06\)9:2<135::AID-PPP284>3.0.CO;2-R](https://doi.org/https://doi.org/10.1002/(SICI)1099-1530(199804/06)9:2<135::AID-PPP284>3.0.CO;2-R)
- Berthling, I., Etzelmüller, B., Isaksen, K., and Sollid, J. L. (2000). Rock glaciers on Prins Karls Forland. II: GPR soundings and the development of internal structures. *Permafrost and Periglacial Processes*, 11, 357-369. <https://doi.org/https://doi.org/10.1002/1099-1530>
- Biskaborn, B. K., Smith, S. L., Noetzli, J., Matthes, H., Vieira, G., Streletskiy, D. A., Schoeneich, P., Romanovsky, V. E., Lewkowicz, A. G., Abramov, A., Allard, M., Boike, J., Cable, W. L., Christiansen, H. H., Delaloye, R., Diekmann, B., Drozdov, D., Etzelmüller, B., Grosse, G., Guglielmin, M., Ingeman-Nielsen, T., Isaksen, K., Ishikawa, M., Johansson, M., Johannsson, H., Joo, A., Kaverin, D., Kholodov, A., Konstantinov, P., Kröger, T., Lambiel, C., Lanckman, J.-P., Luo, D., Malkova, G., Meiklejohn, I., Moskalenko, N., Oliva, M., Phillips, M., Ramos, M., Sannel, A. B. K., Sergeev, D., Seybold, C., Skryabin, P., Vasiliev, A., Wu, Q., Yoshikawa, K., Zheleznyak, M., and Lantuit, H. (2019). Permafrost is warming at a global scale. *Nature Communications*, 10(1). <https://doi.org/10.1038/s41467-018-08240-4>
- Blöthe, J. H., Rosenwinkel, S., Höser, T., and Korup, O. (2019). Rock-glacier dams in High Asia. *Earth Surface Processes and Landforms*, 44(3), 808-824. <https://doi.org/https://doi.org/10.1002/esp.4532>
- Bodin, X., Krysiecki, J.-M., Schoeneich, P., Le Roux, O., Lorier, L., Echelard, T., Peyron, M., and Walpersdorf, A. (2017). The 2006 Collapse of the Béard Rock Glacier (Southern French Alps). *Permafrost and Periglacial Processes*, 28(1), 209-223. <https://doi.org/https://doi.org/10.1002/ppp.1887>

BIBLIOGRAPHY

- Bodin, X., and Schoeneich, P. (2008). *High-resolution DEM extraction from terrestrial LiDAR topometry and surface kinematics of the creeping alpine permafrost: The Laurichard rock glacier case study (Southern French Alps)* Ninth International Conference on Permafrost, Institute of Northern Engineering, University of Alaska at Fairbanks.
- Bodin, X., Thibert, E., Fabre, D., Ribolini, A., Schoeneich, P., Francou, B., Reynaud, L., and Fort, M. (2009). Two decades of responses (1986–2006) to climate by the Laurichard rock glacier, French Alps. *Permafrost and Periglacial Processes*, 20(4), 331-344. <https://doi.org/https://doi.org/10.1002/ppp.665>
- Bodin, X., Thibert, E., Sanchez, O., Rabatel, A., and Jaitlet, S. (2018). Multi-Annual Kinematics of an Active Rock Glacier Quantified from Very High-Resolution DEMs: An Application-Case in the French Alps. *Remote Sensing*, 10(4), 547. <https://www.mdpi.com/2072-4292/10/4/547>
- Böhlert, R., Compeer, M., Egli, M., Brandova, D., Maisch, M., Kubik, P., and Haeberli, W. (2011). A combination of relative-numerical dating methods indicates two high alpine rock glacier activity phases after the glacier advance of the Younger Dryas. *The Open Geography Journal*, 4, 115–130. <https://doi.org/10.5167/uzh-42941>
- Bolch, T., Marchenko, S., Braun, L. N., Hagg, W., Severskiy, I. V., and Young, G. (2009). Significance of glaciers, rockglaciers and ice-rich permafrost in the Northern Tien Shan as water towers under climate change conditions. *IHP/HWRP-Berichte*(8), 132-144.
- Bollmann, E., Girstmair, A., Mitterer, S., Krainer, K., Sailer, R., and Stötter, J. (2015). A Rock Glacier Activity Index Based on Rock Glacier Thickness Changes and Displacement Rates Derived From Airborne Laser Scanning. *Permafrost and Periglacial Processes*, 26(4), 347-359. <https://doi.org/https://doi.org/10.1002/ppp.1852>
- Boulton, G. S., and Jones, A. S. (1979). Stability of temperate ice caps and ice sheets resting on beds of deformable sediment. *Journal of Glaciology*, 24(90), 29-43. <https://doi.org/https://doi.org/10.3189/S0022143000014623>
- Brardinoni, F., Scotti, R., Sailer, R., and Mair, V. (2019). Evaluating sources of uncertainty and variability in rock glacier inventories. *Earth Surface Processes and Landforms*, 44(12), 2450-2466. <https://doi.org/10.1002/esp.4674>
- Brenning, A. (2005a). *Climatic and geomorphological controls of rock glaciers in the Andes of Central Chile* Humboldt-Universität zu Berlin, Mathematisch-Naturwissenschaftliche Fakultät III].
- Brenning, A. (2005b). Geomorphological, hydrological and climatic significance of rock glaciers in the Andes of Central Chile (33-35 degrees S). *Permafrost and Periglacial Processes*, 16(3), 231-240. <https://doi.org/https://doi.org/10.1002/ppp.528>
- Buchli, T., Kos, A., Limpach, P., Merz, K., Zhou, X. H., and Springman, S. M. (2018). Kinematic investigations on the Furggwanghorn Rock Glacier, Switzerland. *Permafrost and Periglacial Processes*, 29(1), 3-20. <https://doi.org/https://doi.org/10.1002/ppp.1968>
- Buchli, T., Merz, K., Zhou, X., Kinzelbach, W., and Springman, S. M. (2013). Characterization and Monitoring of the Furggwanghorn Rock Glacier, Turtmann Valley, Switzerland: Results from 2010 to 2012. *Vadose Zone Journal*, 12(1), vjz2012.0067. <https://doi.org/https://doi.org/10.2136/vzj2012.0067>
- Bucki, A. K., and Echelmeyer, K. A. (2004). The flow of Fireweed rock glacier, Alaska, USA. *Journal of Glaciology*, 50(168), 76-86.
- Capps, S. R. (1910). Rock Glaciers in Alaska. *The Journal of Geology*, 18(4), 359-375. <https://doi.org/10.1086/621746>
- Carr, M. H. (1987). Water on Mars. *Nature*, 326(6108), 30-35. <https://doi.org/10.1038/326030a0>

BIBLIOGRAPHY

- Carr, M. H., and Schaber, G. G. (1977). Martian permafrost features. *Journal of Geophysical Research*, 82(28), 4039-4054.
- Carslaw, H. S., and Jaeger, J. C. (1959). *Conduction of heat in solids*. Oxford Science Publications. Clarendon Press.
- Chaix, A. (1919). Coulées de blocs dans le Parc National Suisse de la Basse-Engadine. *CR Séances Soc Phy Hist Nat Geneve*, 36, 12-15.
- Chen, C. W., and Zebker, H. A. (2002). Phase unwrapping for large SAR interferograms: statistical segmentation and generalized network models. *IEEE Transactions on Geoscience and Remote Sensing*, 40(8), 1709-1719. <https://doi.org/https://doi.org/10.1109/TGRS.2002.802453>
- Chen, L.-C., Zhu, Y., Papandreou, G., Schroff, F., and Adam, H. (2018). *Encoder-decoder with atrous separable convolution for semantic image segmentation* European Conference on Computer Vision (ECCV), Munich, Germany.
- Cheng, G. D., Zhao, L., Li, R., Wu, X., Sheng, Y., Hu, G., Zou, D., Jin, H., Li, X., and Wu, Q. (2019). Characteristic, changes and impacts of permafrost on Qinghai-Tibet Plateau. *Chinese Science Bulletin*, 64(27), 2783-2795. <https://doi.org/10.1360/tb-2019-0191>
- Chudley, T. R., and Willis, I. C. (2019). Glacier surges in the north-west West Kunlun Shan inferred from 1972 to 2017 Landsat imagery. *Journal of Glaciology*, 65(249), 1-12.
- Chueca, J. (1992). A Statistical-Analysis of the Spatial-Distribution of Rock Glaciers, Spanish Central Pyrenees. In *Permafrost and Periglacial Processes, Vol 3, No 3, Jul-Sept 1992: Permafrost and Periglacial Environments in Mountain Areas* (pp. 261-265).
- Cicoira, A., Beutel, J., Faillettaz, J., Gartner-Roer, I., and Vieli, A. (2019a). Resolving the influence of temperature forcing through heat conduction on rock glacier dynamics: a numerical modelling approach. *The Cryosphere*, 13(3), 927-942. <https://doi.org/https://doi.org/10.5194/tc-13-927-2019>
- Cicoira, A., Beutel, J., Faillettaz, J., and Vieli, A. (2019b). Water controls the seasonal rhythm of rock glacier flow. *Earth and Planetary Science Letters*, 528. <https://doi.org/https://doi.org/10.1016/j.epsl.2019.115844>
- Cicoira, A., Marcer, M., Gartner-Roer, I., Bodin, X., Arenson, L. U., and Vieli, A. (2020). A general theory of rock glacier creep based on in-situ and remote sensing observations. *Permafrost and Periglacial Processes*. <https://doi.org/https://doi.org/10.1002/ppp.2090>
- Colaprete, A., and Jakosky, B. M. (1998). Ice flow and rock glaciers on Mars. *Journal of Geophysical Research: Planets*, 103(E3), 5897-5909. <https://doi.org/https://doi.org/10.1029/97JE03371>
- Corte, A. (1976). The Hydrological Significance of Rock Glaciers. *Journal of Glaciology*, 17(75), 157-158. <https://doi.org/https://doi.org/10.3189/s0022143000030859>
- Croce, F. A., and Milana, J. P. (2002). Internal structure and behaviour of a rock glacier in the Arid Andes of Argentina. *Permafrost and Periglacial Processes*, 13(4), 289-299. <https://doi.org/https://doi.org/10.1002/ppp.431>
- Cuffey, K., and Paterson, W. S. B. (2010). *The physics of glaciers* (4th ed.). Butterworth-Heinemann/Elsevier.
- Cui, Z. (1981). Periglacial landforms and regional characteristics on Qinghai-Xizang Plateau. *Kexue Tongbao*(6), 724-733.
- Cui, Z. (1985). Discovery of Kunlunshan-type rock glaciers and the classification of rock glaciers. *Kexue Tongbao*, 30(3), 365-369. <https://doi.org/10.1360/sb1985-30-3-365>

BIBLIOGRAPHY

- Cui, Z., and Zhu, C. (1988). *Rock glaciers in the source region of Urumqi River, middle Tian Shan, China* 5th International Conference on Permafrost,
- De Sanjose, J. J., Berenguer, F., Atkinson, A. D. J., De Matias, J., Serrano, E., Gomez-Ortiz, A., Gonzalez-Garcia, M., and Rico, I. (2014). Geomatics Techniques Applied to Glaciers, Rock Glaciers, and Ice Patches in Spain (1991-2012). *Geografiska Annaler Series a-Physical Geography*, 96(3), 307-321. <https://doi.org/10.1111/geoa.12047>
- Degenhardt, J. J. (2003). Subsurface investigation of a rock glacier using ground-penetrating radar: Implications for locating stored water on Mars. *Journal of Geophysical Research*, 108(E4). <https://doi.org/10.1029/2002je001888>
- Delaloye, R., Barboux, C., Bodin, X., Brenning, A., Hartl, L., Hu, Y., Ikeda, A., Kaufmann, V., Kellerer-Pirklbauer, A., Lambiel, C., Liu, L., Marcer, M., Rick, B., Scotti, R., Takadema, H., Liudat, D. T., Vivero, S., and Winterberger, M. (2018). *Rock glacier inventories and kinematics: a new IPA Action Group* 5th European Conference on Permafrost, Chamonix, France.
- Delaloye, R., and Echelard, T. (2020). *Towards standard guidelines for inventorying rock glaciers: Baseline concepts version 4.0.* https://bigweb.unifr.ch/Science/Geosciences/Geomorphology/Pub/Website/IPA/Guidelines/V4/200117_Baseline_Concepts_Inventorying_Rock_Glaciers_V4.pdf
- Delaloye, R., Lambiel, C., and Gärtner-Roer, I. (2010). Overview of rock glacier kinematics research in the Swiss Alps. *Geographica Helvetica*, 65(2), 135-145. <https://doi.org/10.5194/gh-65-135-2010>
- Delaloye, R., Morard, S., Barboux, C., Abbet, D., Gruber, V., Riedo, M., and Gachet, S. (2013). Rapidly moving rock glaciers in Matteringal. *Geographica Helvetica*, 21-31.
- Delaloye, R., Perruchoud, E., Avian, M., Kaufmann, V., Bodin, X., Hausmann, H., Ikeda, A., Käib, A., Kellerer-Pirklbauer, A., and Krainer, K. (2008). Recent interannual variations of rock glacier creep in the European Alps. *9th International Conference on Permafrost*, 343–348.
- Dini, B., Daout, S., Manconi, A., and Loew, S. (2019). Classification of slope processes based on multitemporal DInSAR analyses in the Himalaya of NW Bhutan. *Remote Sensing of Environment*, 233. <https://doi.org/10.1016/j.rse.2019.111408>
- Echelmeyer, K., and Wang, Z. (1987). Direct Observation of Basal Sliding and Deformation of Basal Drift at Sub-Freezing Temperatures. *Journal of Glaciology*, 33(113), 83-98. <https://doi.org/https://doi.org/10.3189/S0022143000005396>
- Ellis, J. M., and Calkin, P. E. (1979). Nature and Distribution of Glaciers, Neoglacial Moraines, and Rock Glaciers, East-Central Brooks Range, Alaska. *Arctic and Alpine Research*, 11(4), 403-420. <https://doi.org/10.1080/00040851.1979.12004149>
- Emmert, A., and Kneisel, C. (2017). Internal structure of two alpine rock glaciers investigated by quasi-3-D electrical resistivity imaging. *Cryosphere*, 11(2), 841-855. <https://doi.org/10.5194/tc-11-841-2017>
- Eriksen, H. Ø., Rouyet, L., Lauknes, T. R., Berthling, I., Isaksen, K., Hindberg, H., Larsen, Y., and Corner, G. D. (2018). Recent Acceleration of a Rock Glacier Complex, Ádjet, Norway, Documented by 62 Years of Remote Sensing Observations. *Geophysical Research Letters*, 45(16), 8314-8323. <https://doi.org/https://doi.org/10.1029/2018GL077605>
- Everingham, M., Eslami, S. M. A., Van Gool, L., Williams, C. K. I., Winn, J., and Zisserman, A. (2015). The Pascal Visual Object Classes challenge: a retrospective. *International Journal of Computer Vision*, 111(1), 98-136. <https://doi.org/10.1007/s11263-014-0733-5>
- Falaschi, D., Castro, M., Masiokas, M., Tadono, T., and Ahumada, A. L. (2014). Rock Glacier Inventory of the Valles Calchaquíes Region (~ 25°S), Salta, Argentina, Derived from ALOS Data.

BIBLIOGRAPHY

- Permafrost and Periglacial Processes*, 25(1), 69-75.
<https://doi.org/https://doi.org/10.1002/ppp.1801>
- Florentine, C., Skidmore, M., Speece, M., Link, C., and Shaw, C. A. (2014). Geophysical analysis of transverse ridges and internal structure at Lone Peak Rock Glacier, Big Sky, Montana, USA. *Journal of Glaciology*, 60(221), 453-462.
<https://doi.org/https://doi.org/10.3189/2014jog13j160>
- Francou, B., and Reynaud, L. (1992). 10 year surficial velocities on a rock glacier (Laurichard, French Alps). *Permafrost and Periglacial Processes*, 3(3), 209-213.
- Frehner, M., Ling, A. H. M., and Gärtner-Roer, I. (2015). Furrow-and-ridge morphology on rockglaciers explained by gravity-driven buckle folding: A case study from the Murtal rockglacier (Switzerland). *Permafrost and Periglacial Processes*, 26(1), 57-66.
<https://doi.org/https://doi.org/10.1002/ppp.1831>
- Fujii, Y., and Higuchi, K. (1976). Ground Temperature and its Relation to Permafrost Occurrences in the Khumbu Region and Hidden Valley. *Journal of the Japanese Society of Snow and Ice*, 38(Special), 125-128. https://doi.org/https://doi.org/10.5331/sepyo.38.Special_125
- Fukui, K., Sone, T., Strelin, J. A., Torielli, C. A., and Mori, J. (2007). Ground penetrating radar sounding on an active rock glacier on James Ross Island, Antarctic Peninsula region. *Polish Polar Research*(No 1), 13-22. <http://journals.pan.pl/Content/110589>
- Fukui, K., Sone, T., Strelin, J. A., Torielli, C. A., Mori, J., and Fujii, Y. (2008). Dynamics and GPR stratigraphy of a polar rock glacier on James Ross Island, Antarctic Peninsula. *Journal of Glaciology*, 54(186), 445-451. <https://doi.org/https://doi.org/10.3189/002214308785836940>
- Gao, M., Xu, X., Klinger, Y., van der Woerd, J., and Tapponnier, P. (2017). High-resolution mapping based on an Unmanned Aerial Vehicle (UAV) to capture paleoseismic offsets along the Altyn-Tagh fault, China. *Sci Rep*, 7(1), 8281. <https://doi.org/10.1038/s41598-017-08119-2>
- Geiger, S. T., Daniels, J. M., Miller, S. N., and Nicholas, J. W. (2018). Influence of Rock Glaciers on Stream Hydrology in the La Sal Mountains, Utah. *Arctic, Antarctic, and Alpine Research*, 46(3), 645-658. <https://doi.org/10.1657/1938-4246-46.3.645>
- Glen, J. W. (1955). The creep of polycrystalline ice. *Proceedings of the Royal Society of London. Series A, Mathematical and Physical Sciences* (1934-1990), 228(1175), 519-538. <https://doi.org/https://doi.org/10.1098/rspa.1955.0066>
- Gorbunov, A. P., Titkov, S. N., and Polyakov, V. G. (1992). Dynamics of rock glaciers of the Northern Tien Shan and the Djungar Ala Tau, Kazakhstan. *Permafrost and Periglacial Processes*, 3(1), 29-39. <https://doi.org/https://doi.org/10.1002/ppp.3430030105>
- Guglielmin, M., Camusso, M., Polesello, S., and Valsecchi, S. (2004). An old relict glacier body preserved in permafrost environment: The Foscagno rock glacier ice core (Upper Valtellina, Italian central Alps). *Arctic Antarctic and Alpine Research*, 36(1), 108-116. <https://doi.org/https://doi.org/10.1657/1523-0430>
- Guglielmin, M., Ponti, S., and Forte, E. (2018). The origins of Antarctic rock glaciers: periglacial or glacial features? *Earth Surface Processes and Landforms*, 43(7), 1390-1402. <https://doi.org/https://doi.org/10.1002/esp.4320>
- Guglielmin, M., and Smiraglia, C. (1998). The rock glacier inventory of the Italian Alps. The 7th International Permafrost Conference, Yellowknife, Canada.
- Haeberli, W. (2000). Modern research perspectives relating to permafrost creep and rock glaciers: A discussion. *Permafrost and Periglacial Processes*, 11(4), 290-293. [https://doi.org/https://doi.org/10.1002/1099-1530\(200012\)11:4](https://doi.org/https://doi.org/10.1002/1099-1530(200012)11:4)

BIBLIOGRAPHY

- Haeberli, W., Hallet, B., Arenson, L., Elconin, R., Humlum, O., Käab, A., Kaufmann, V., Ladanyi, B., Matsuoka, N., Springman, S., and Mühl, D. V. (2006). Permafrost creep and rock glacier dynamics. *Permafrost and Periglacial Processes*, 17(3), 189-214. <https://doi.org/https://doi.org/10.1002/ppp.561>
- Haeberli, W., Hoelzle, M., Kaab, A., Keller, F., Vonder Mühl, D., and Wagner, S. (1998). Ten years after drilling through the permafrost of the active rock glacier Murtel, Eastern Swiss Alps: answered questions and new perspectives. Seventh International Conference on Permafrost, Yellowknife.
- Haeberli, W., Kaab, A., Wagner, S., Vonder Mühl, D., Geissler, P., Haas, J. N., Glatzel-Mattheier, H., and Wagenbach, D. (1999). Pollen analysis and C-14 age of moss remains in a permafrost core recovered from the active rock glacier Murtel-Corvatsch, Swiss Alps: Geomorphological and glaciological implications. *Journal of Glaciology*, 45(149), 1-8. <https://doi.org/https://doi.org/10.3189/s0022143000002975>
- Haeberli, W., King, L., and Flotron, A. (1979). Surface Movement and Lichen-Cover Studies at the Active Rock Glacier near the Grubengletscher, Wallis, Swiss Alps. *Arctic and Alpine Research*, 11(4), 421-441. <https://doi.org/10.2307/1550561>
- Haeberli, W., and Schmid, W. (1988). *Aerophotogrammetrical monitoring of rock glaciers* Proceedings of the 5th International Conference on Permafrost, Trondheim, Norway.
- Hanssen, R. F. (2001). *Radar interferometry : data interpretation and error analysis*. Kluwer Academic.
- Harris, C., Davies, M. C. R., and Rea, B. R. (2003). Gelifluction: viscous flow or plastic creep? *Earth Surface Processes and Landforms*, 28(12), 1289-1301. <https://doi.org/10.1002/esp.543>
- Harris, S. A. (1994). Climatic Zonality of Periglacial Landforms in Mountain Areas. *Arctic*, 47(2), 184-192.
- Harris, S. A., Cui, Z. J., and Cheng, G. D. (1998). Origin of a bouldery diamictite, Kunlun pass, Qinghai-Xizang plateau, People's Republic of China: Gelifluction deposit or rock glacier? *Earth Surface Processes and Landforms*, 23(10), 943-952. [https://doi.org/10.1002/\(SICI\)1096-9837\(199810\)23:10<943::AID-ESP913>3.0.CO;2-7](https://doi.org/10.1002/(SICI)1096-9837(199810)23:10<943::AID-ESP913>3.0.CO;2-7)
- Hartl, L., Fischer, A., Stocker-waldhuber, M., and Abermann, J. (2016). Recent speed-up of an alpine rock glacier: an updated chronology of the kinematics of outer hochebenkar rock glacier based on geodetic measurements. *Geografiska Annaler: Series A, Physical Geography*, 98(2), 129-141. <https://doi.org/10.1111/geoa.12127>
- Hauber, E., Reiss, D., Ulrich, M., Preusker, F., Trauthan, F., Zanetti, M., Hiesinger, H., Jaumann, R., Johansson, L., Johnsson, A., Van Gasselt, S., and Olvmo, M. (2011). Landscape evolution in Martian mid-latitude regions: insights from analogous periglacial landforms in Svalbard. *Geological Society, London, Special Publications*, 356(1), 111-131. <https://doi.org/10.1144/sp356.7>
- Hauck, C. (2013). New concepts in geophysical surveying and data interpretation for permafrost terrain. *Permafrost and Periglacial Processes*, 24(2), 131-137. <https://doi.org/https://doi.org/10.1002/ppp.1774>
- Hausmann, H., Krainer, K., Bruckl, E., and Mostler, W. (2007). Internal structure and ice content of reichenkar rock glacier (Stubai alps, Austria) assessed by geophysical investigations. *Permafrost and Periglacial Processes*, 18(4), 351-367. <https://doi.org/https://doi.org/10.1002/ppp.601>
- Hoelzle, M., Wagner, S., Käab, A., and Vonder Mühl, D. (1998). Surface movement and internal deformation of ice-rock mixtures within rock glaciers in the Upper Engadin, Switzerland. *Proceedings of the 7th International Conference on Permafrost*, 465-471.

BIBLIOGRAPHY

- Hu, Y., Liu, L., Wang, X., Zhao, L., Wu, T., Cai, J., Zhu, X., and Hao, J. (2021). Quantification of permafrost creep provides kinematic evidence for classifying a puzzling periglacial landform. *Earth Surface Processes and Landforms*, 46(2), 465-477. <https://doi.org/https://doi.org/10.1002/esp.5039>
- Huang, L., Luo, J., Lin, Z., Niu, F., and Liu, L. (2020). Using deep learning to map retrogressive thaw slumps in the Beiluhe region (Tibetan Plateau) from CubeSat images. *Remote Sensing of Environment*, 237. <https://doi.org/10.1016/j.rse.2019.111534>
- Humlum, O. (1988). Rock Glacier Appearance Level and Rock Glacier Initiation Line Altitude - a Methodological Approach to the Study of Rock Glaciers. *Arctic and Alpine Research*, 20(2), 160-178. <https://doi.org/10.2307/1551495>
- Ikeda, A., and Matsuoka, N. (2006). Pebby versus bouldery rock glaciers: Morphology, structure and processes. *Geomorphology*, 73(3-4), 279-296. <https://doi.org/10.1016/j.geomorph.2005.07.015>
- Ikeda, A., Matsuoka, N., and Kaab, A. (2008). Fast deformation of perennially frozen debris in a warm rock glacier in the Swiss Alps: An effect of liquid water. *Journal of Geophysical Research-Earth Surface*, 113(F1). <https://doi.org/10.1029/2007JF000859>
- Immerzeel, W. W., van Beek, L. P. H., and Bierkens, M. F. P. (2010). Climate Change Will Affect the Asian Water Towers. *Science*, 328(5984), 1382. <https://doi.org/10.1126/science.1183188>
- Iribarren Anacona, P., and Bodin, X. (2010). *Geomorphic consequences of two large glacier and rock glacier destabilizations in the Central and Northern Chilean Andes* EGU General Assembly Conference Abstracts,
- Jaesche, P., Huwe, B., Stingl, H., and Veit, H. (2002). Temporal variability of alpine solifluction : a modelling approach. *Geogr. Helv.*, 57(3), 157-169. <https://doi.org/10.5194/gh-57-157-2002>
- Jakob, M. (1992). Active rock glaciers and the lower limit of discontinuous alpine permafrost, Khumbu-Himalaya, Nepal. *Permafrost and Periglacial Processes*, 3(3), 253-256.
- Janke, J. R. (2005). Photogrammetric Analysis of Front Range Rock Glacier Flow Rates. *Geografiska Annaler: Series A, Physical Geography*, 87(4), 515-526. <https://doi.org/https://doi.org/10.1111/j.0435-3676.2005.00275.x>
- Janke, J. R. (2007). Colorado Front Range Rock Glaciers: Distribution and Topographic Characteristics. *Arctic, Antarctic, and Alpine Research*, 39(1), 74-83, 10. [https://doi.org/10.1657/1523-0430\(2007\)39\[74:CFRRGD\]2.0.CO;2](https://doi.org/10.1657/1523-0430(2007)39[74:CFRRGD]2.0.CO;2)
- Jansen, F., and Hergarten, S. (2006). Rock glacier dynamics: Stick-slip motion coupled to hydrology. *Geophysical Research Letters*, 33(10). <https://doi.org/10.1029/2006GL026134>
- Jones, D. B., Harrison, S., and Anderson, K. (2019a). Mountain glacier-to-rock glacier transition. *Global and Planetary Change*, 181. <https://doi.org/https://doi.org/10.1016/j.gloplacha.2019.102999>
- Jones, D. B., Harrison, S., Anderson, K., and Betts, R. A. (2018a). Mountain rock glaciers contain globally significant water stores. *Scientific Reports*, 8. <https://doi.org/https://doi.org/10.1038/s41598-018-21244-w>
- Jones, D. B., Harrison, S., Anderson, K., Selley, H. L., Wood, J. L., and Betts, R. A. (2018b). The distribution and hydrological significance of rock glaciers in the Nepalese Himalaya. *Global and Planetary Change*, 160, 123-142. <https://doi.org/https://doi.org/10.1016/j.gloplacha.2017.11.005>

BIBLIOGRAPHY

- Jones, D. B., Harrison, S., Anderson, K., Shannon, S., and Betts, R. A. (2021). Rock glaciers represent hidden water stores in the Himalaya. *Science of The Total Environment*, 145368. <https://doi.org/https://doi.org/10.1016/j.scitotenv.2021.145368>
- Jones, D. B., Harrison, S., Anderson, K., and Whalley, W. B. (2019b). Rock glaciers and mountain hydrology: A review. *Earth-Science Reviews*, 193, 66-90. <https://doi.org/https://doi.org/10.1016/j.earscirev.2019.04.001>
- Kääb, A., Frauenfelder, R., and Roer, I. (2007). On the response of rockglacier creep to surface temperature increase. *Global and Planetary Change*, 56(1-2), 172-187. <https://doi.org/https://doi.org/10.1016/j.gloplacha.2006.07.005>
- Kääb, A., Haeberli, W., and Gudmundsson, G. H. (1997). Analysing the creep of mountain permafrost using high precision aerial photogrammetry: 25 years of monitoring Gruben Rock Glacier, Swiss Alps. *Permafrost and Periglacial Processes*, 8(4), 409-426. [https://doi.org/10.1002/\(SICI\)1099-1530\(199710/12\)8:4<409::AID-PPP267>3.0.CO;2-C](https://doi.org/10.1002/(SICI)1099-1530(199710/12)8:4<409::AID-PPP267>3.0.CO;2-C)
- Kääb, A., and Reichmuth, T. (2005). Advance mechanisms of rock glaciers. *Permafrost and Periglacial Processes*, 16(2), 187-193. <https://doi.org/https://doi.org/10.1002/ppp.507>
- Kääb, A., Strozzi, T., Bolch, T., Caduff, R., Trefall, H., Stoffel, M., and Kokarev, A. (2021). Inventory and changes of rock glacier creep speeds in Ile Alatau and Kung öy Ala-Too, northern Tien Shan, since the 1950s. *The Cryosphere*, 15(2), 927-949. <https://doi.org/10.5194/tc-15-927-2021>
- Kääb, A., Treichler, D., Nuth, C., and Berthier, E. (2015). Brief Communication: Contending estimates of 2003–2008 glacier mass balance over the Pamir–Karakoram–Himalaya. *The Cryosphere*, 9(2), 557-564. <https://doi.org/10.5194/tc-9-557-2015>
- Kaufmann, V., and Ladstädter, R. (2006a). 10 Years of monitoring of the Doesen rock glacier. ICA Mountain Cartography Workshop, Bohinj, Slovenia.
- Kaufmann, V., and Ladstädter, R. (2006b). *Mapping of the 3D surface motion field of Doesen rock glacier (Ankogel group, Austria) and its spatio-temporal change (1954-1998) by means of digital photogrammetry*. na.
- Kellerer-Pirklbauer, A., and Kaufmann, V. (2012). About the relationship between rock glacier velocity and climate parameters in central Austria. *Austrian Journal of Earth Sciences*, 105(2), 94-112.
- Kellerer-Pirklbauer, A., Lieb, G. K., and Kaufmann, V. (2018). The Dösen Rock Glacier in Central Austria: A key site for multidisciplinary long-term rock glacier monitoring in the Eastern Alps. *Austrian Journal of Earth Sciences*, 110(2). <https://doi.org/10.17738/ajes.2017.0013>
- Kenner, R., Bühl, Y., Delaloye, R., Ginzler, C., and Phillips, M. (2014). Monitoring of high alpine mass movements combining laser scanning with digital airborne photogrammetry. *Geomorphology*, 206, 492-504. <https://doi.org/https://doi.org/10.1016/j.geomorph.2013.10.020>
- Kenner, R., Phillips, M., Beutel, J., Hiller, M., Limpach, P., Pointner, E., and Volken, M. (2017). Factors Controlling Velocity Variations at Short-Term, Seasonal and Multiyear Time Scales, Ritigraben Rock Glacier, Western Swiss Alps. *Permafrost and Periglacial Processes*, 28(4), 675-684. <https://doi.org/https://doi.org/10.1002/ppp.1953>
- Kenner, R., Pruessner, L., Beutel, J., Limpach, P., and Phillips, M. (2019). How rock glacier hydrology, deformation velocities and ground temperatures interact: Examples from the Swiss Alps. *Permafrost and Periglacial Processes*, 31(1), 3-14. <https://doi.org/https://doi.org/10.1002/ppp.2023>

BIBLIOGRAPHY

- Kenyi, L. W., and Kaufmann, V. (2003). Estimation of rock glacier surface deformation using SAR interferometry data. *IEEE Transactions on Geoscience and Remote Sensing*, 41(6), 1512-1515. <https://doi.org/10.1109/TGRS.2003.811996>
- Kinnard, C., and Lewkowicz, A. G. (2005). Movement, moisture and thermal conditions at a turf-banked solifluction lobe, Kluane Range, Yukon Territory, Canada. *Permafrost and Periglacial Processes*, 16(3), 261-275. <https://doi.org/10.1002/ppp.530>
- Kneisel, C., Hauck, C., Fortier, R., and Moorman, B. (2008). Advances in geophysical methods for permafrost investigations. *Permafrost and Periglacial Processes*, 19(2), 157-178. <https://doi.org/https://doi.org/10.1002/ppp.616>
- Knight, J., Harrison, S., and Jones, D. B. (2019). Rock glaciers and the geomorphological evolution of deglacierizing mountains. *Geomorphology*, 324, 14-24. <https://doi.org/https://doi.org/10.1016/j.geomorph.2018.09.020>
- Krainer, K., Bressan, D., Dietre, B., Haas, J. N., Hajdas, I., Lang, K., Mair, V., Nickus, U., Reidl, D., Thies, H., and Tonidandel, D. (2015). A 10,300-year-old permafrost core from the active rock glacier Lazaun, southern Ötztal Alps (South Tyrol, northern Italy). *Quaternary Research*, 83(2), 324-335. <https://doi.org/https://doi.org/10.1016/j.yqres.2014.12.005>
- Krainer, K., and Mostler, W. (2006). Flow velocities of active rock glaciers in the Austrian Alps. *Geografiska Annaler Series a-Physical Geography*, 88A(4), 267-280. <https://doi.org/10.1111/j.0435-3676.2006.00300.x>
- Ladanyi, B. (2003). Rheology of ice/rock systems and interfaces. The Eighth International Conference on Permafrost, Zurich, Switzerland.
- Ladanyi, B. (2006). Creep of frozen slopes and ice-filled rock joints under temperature variation. *Canadian Journal of Civil Engineering*, 33(6), 719-725. <https://doi.org/10.1139/L05-112>
- Lambiel, C., and Delaloye, R. (2004). Contribution of real-time kinematic GPS in the study of creeping mountain permafrost: Examples from the Western Swiss Alps. *Permafrost and Periglacial Processes*, 15(3), 229-241. <https://doi.org/10.1002/ppp.496>
- LeCun, Y., Bengio, Y., and Hinton, G. (2015). Deep learning. *Nature*, 521(7553), 436-444. <https://doi.org/10.1038/nature14539>
- Leopold, M., Williams, M. W., Caine, N., Vökel, J., and Dethier, D. (2011). Internal structure of the Green Lake 5 rock glacier, Colorado Front Range, USA. *Permafrost and Periglacial Processes*, 22(2), 107-119. <https://doi.org/https://doi.org/10.1002/ppp.706>
- Li, J. (1986). *Tibetan glaciers*. Science Press.
- Li, K., Chen, J., Zhao, L., Zhang, X., Pang, Q., Fang, H., and Liu, G. (2012). Permafrost distribution in typical area of West Kunlun Mountains derived from a comprehensive survey. *Journal of Glaciology and Geocryology*, 34(2), 447-454.
- Li, S., and Shi, Y. (1992). Glacial and lake fluctuations in the area of the west Kunlun mountains during the last 45 000 years. *Annals of Glaciology*, 16, 79-84.
- Li, S., and Yao, H. (1987). Preliminary study of rock glaciers in the Gongga Mt. area. *Journal of Glaciology and Geocryology*, 1, 55-60.
- Lilleøren, K. S., Etzelmüller, B., Gätner-Roer, I., Käb, A., Westermann, S., and Guðmundsson, Á. (2013). The Distribution, Thermal Characteristics and Dynamics of Permafrost in Tröllaskagi, Northern Iceland, as Inferred from the Distribution of Rock Glaciers and Ice-Cored Moraines. *Permafrost and Periglacial Processes*, 24(4), 322-335. <https://doi.org/https://doi.org/10.1002/ppp.1792>

BIBLIOGRAPHY

- Liu, G., Xiong, H., Cui, Z., and Song, C. (1995). The morphological features and environmental condition of rockglaciers in Tianshan Mountains. *Scientia Geographica Sinica*, 15(3), 226-233.
- Liu, L., Millar, C. I., Westfall, R. D., and Zebker, H. A. (2013). Surface motion of active rock glaciers in the Sierra Nevada, California, USA: inventory and a case study using InSAR. *The Cryosphere*, 7(4), 1109-1119. <https://doi.org/10.5194/tc-7-1109-2013>
- Lliboutry, L. (1953). Internal moraines and rock glaciers. *Journal of Glaciology*, 2(14), 296-296. <https://doi.org/10.3189/S0022143000025521>
- Lugon, R., and Stoffel, M. (2010). Rock-glacier dynamics and magnitude–frequency relations of debris flows in a high-elevation watershed: Ritigraben, Swiss Alps. *Global and Planetary Change*, 73(3), 202-210. <https://doi.org/https://doi.org/10.1016/j.gloplacha.2010.06.004>
- Lv, Y., and Li, B. (2006). *Edaphology*. China Agriculture Press.
- Mahaney, W. C., Miyamoto, H., Dohm, J. M., Baker, V. R., Cabrol, N. A., Grin, E. A., and Berman, D. C. (2007). Rock glaciers on Mars: Earth-based clues to Mars' recent paleoclimatic history. *Planetary and Space Science*, 55(1-2), 181-192.
- Marcer, M., Ciciora, A., Cusicanqui, D., Bodin, X., Echelard, T., Obregon, R., and Schoeneich, P. (2021). Rock glaciers throughout the French Alps accelerated and destabilised since 1990 as air temperatures increased. *Communications Earth & Environment*, 2(1). <https://doi.org/10.1038/s43247-021-00150-6>
- Marcer, M., Serrano, C., Brenning, A., Bodin, X., Goetz, J., and Schoeneich, P. (2019). Evaluating the destabilization susceptibility of active rock glaciers in the French Alps. *The Cryosphere*, 13(1), 141-155. <https://doi.org/10.5194/tc-13-141-2019>
- Massonnet, D., and Feigl, K. L. (1998). Radar interferometry and its application to changes in the Earth's surface. *Reviews of Geophysics*, 36(4), 441-500. <https://doi.org/https://doi.org/10.1029/97RG03139>
- Matsumoto, H., Yamada, S., and Hirakawa, K. (2010). Relationship Between Ground Ice and Solifluction: Field Measurements in the Daisetsu Mountains, Northern Japan. *Permafrost and Periglacial Processes*, 21(1), 78-89. <https://doi.org/10.1002/ppp.675>
- Matsuoka, N. (1998a). Modelling frost creep rates in an Alpine environment. *Permafrost and Periglacial Processes*, 9(4), 397-409. [https://doi.org/10.1002/\(SICI\)1099-1530\(199810/12\)9:4<397::AID-PPP302>3.0.CO;2-Q](https://doi.org/10.1002/(SICI)1099-1530(199810/12)9:4<397::AID-PPP302>3.0.CO;2-Q)
- Matsuoka, N. (1998b). The relationship between frost heave and downslope soil movement: Field measurements in the Japanese Alps. *Permafrost and Periglacial Processes*, 9(2), 121-133. [https://doi.org/10.1002/\(SICI\)1099-1530\(199804/06\)9:2<121::AID-PPP281>3.3.CO;2-3](https://doi.org/10.1002/(SICI)1099-1530(199804/06)9:2<121::AID-PPP281>3.3.CO;2-3)
- Matsuoka, N. (2001). Solifluction rates, processes and landforms: a global review. *Earth-Science Reviews*, 55(1-2), 107-134. [https://doi.org/10.1016/S0012-8252\(01\)00057-5](https://doi.org/10.1016/S0012-8252(01)00057-5)
- Matsuoka, N., Ikeda, A., and Date, T. (2005). Morphometric analysis of solifluction lobes and rock glaciers in the Swiss Alps. *Permafrost and Periglacial Processes*, 16(1), 99-113. <https://doi.org/10.1002/ppp.517>
- Mellon, M. T., Arvidson, R. E., Marlow, J. J., Phillips, R. J., and Asphaug, E. (2008). Periglacial landforms at the Phoenix landing site and the northern plains of Mars. *Journal of Geophysical Research*, 113. <https://doi.org/10.1029/2007je003039>
- Mellor, M., and Testa, R. (1969). Effect of temperature on the creep of ice. *Journal of Glaciology*, 8(52), 131-145.

BIBLIOGRAPHY

- Messerli, B., and Zurbuchen, M. (1968). *Blockgletscher im Weissmies und Aletsch und ihre photogrammetrische Kartierung, Die Alpen*
- Millar, C. I., and Westfall, R. D. (2008). Rock glaciers and related periglacial landforms in the Sierra Nevada, CA, USA; inventory, distribution and climatic relationships. *Quaternary International*, 188(1), 90-104. <https://doi.org/https://doi.org/10.1016/j.quaint.2007.06.004>
- Millar, C. I., Westfall, R. D., and Delany, D. L. (2013). Thermal and hydrologic attributes of rock glaciers and periglacial talus landforms: Sierra Nevada, California, USA. *Quaternary International*, 310, 169-180. <https://doi.org/10.1016/j.quaint.2012.07.019>
- Monnier, S., and Kinnard, C. (2013). Internal structure and composition of a rock glacier in the Andes (upper Choapa valley, Chile) using borehole information and ground-penetrating radar. *Annals of Glaciology*, 54(64), 61-72. <https://doi.org/https://doi.org/10.3189/2013AoG64A107>
- Monnier, S., and Kinnard, C. (2015a). Internal structure and composition of a rock glacier in the Dry Andes, Inferred from ground-penetrating radar data and its artefacts. *Permafrost and Periglacial Processes*, 26(4), 335-346. <https://doi.org/https://doi.org/10.1002/ppp.1846>
- Monnier, S., and Kinnard, C. (2015b). Reconsidering the glacier to rock glacier transformation problem: New insights from the central Andes of Chile. *Geomorphology*, 238, 47-55. <https://doi.org/https://doi.org/10.1016/j.geomorph.2015.02.025>
- Monnier, S., and Kinnard, C. (2016). Interrogating the time and processes of development of the Las Liebres rock glacier, central Chilean Andes, using a numerical flow model. *Earth Surface Processes and Landforms*, 41(13), 1884-1893. <https://doi.org/10.1002/esp.3956>
- Monnier, S., and Kinnard, C. (2017). Pluri-decadal (1955–2014) evolution of glacier–rock glacier transitional landforms in the central Andes of Chile (30–33 °S). *Earth Surf. Dynam.*, 5(3), 493-509. <https://doi.org/10.5194/esurf-5-493-2017>
- Moore, P. L. (2014). Deformation of debris-ice mixtures. *Reviews of Geophysics*, 52(3), 435-467. <https://doi.org/https://doi.org/10.1002/2014rg000453>
- Müller, J., Vieli, A., and Görtner-Roer, I. (2016). Rock glaciers on the run – understanding rock glacier landform evolution and recent changes from numerical flow modeling. *The Cryosphere*, 10(6), 2865-2886. <https://doi.org/10.5194/tc-10-2865-2016>
- Munroe, J. S. (2018). Distribution, evidence for internal ice, and possible hydrologic significance of rock glaciers in the Uinta Mountains, Utah, USA. *Quaternary Research*, 90(1), 50-65. <https://doi.org/https://doi.org/10.1017/qua.2018.24>
- Nagler, T., Mayer, C., and Rott, H. (2002). Feasibility of DINSAR for mapping complex motion fields of alpine ice- and rock-glaciers. In A. Wilson and S. Quegan (Eds.), *ESA Special Publication* (Vol. 475, pp. 377–382).
- Nan, Z., Li, S., and Liu, Y. (2002). Mean annual ground temperature distribution on the Tibetan plateau: Permafrost distribution mapping and further application. *Journal of Glaciology and Geocryology*, 24(2), 142-148.
- Necsoiu, M., Onaca, A., Wigginton, S., and Urdea, P. (2016). Rock glacier dynamics in Southern Carpathian Mountains from high-resolution optical and multi-temporal SAR satellite imagery. *Remote Sensing of Environment*, 177, 21-36. <https://doi.org/https://doi.org/10.1016/j.rse.2016.02.025>
- Ni, J., Wu, T., Zhu, X., Hu, G., Zou, D., Wu, X., Li, R., Xie, C., Qiao, Y., Pang, Q., Hao, J., and Yang, C. (2020). Simulation of the present and future projection of permafrost on the Qinghai-Tibet Plateau with statistical and machine learning models. *Journal of Geophysical Research: Atmospheres*, n/a(n/a), e2020JD033402. <https://doi.org/https://doi.org/10.1029/2020JD033402>

BIBLIOGRAPHY

- Obu, J., Westermann, S., Barboux, C., Bartsch, A., Delaloye, R., Grosse, G., Heim, B., Hugelius, G., Irrgang, A., Käib, A. M., Kroisleitner, C., Matthes, H., Nitze, I., Pellet, C., Seifert, F. M., Strozzi, T., Wegmüller, U., Wieczorek, M., and Wiesmann, A. (2020). *ESA Permafrost Climate Change Initiative (Permafrost_cci): Permafrost Climate Research Data Package v1*.
- Obu, J., Westermann, S., Bartsch, A., Berdnikov, N., Christiansen, H. H., Dashtseren, A., Delaloye, R., Elberling, B., Etzelmüller, B., Kholodov, A., Khomutov, A., Käib, A., Leibman, M. O., Lewkowicz, A. G., Panda, S. K., Romanovsky, V., Way, R. G., Westergaard-Nielsen, A., Wu, T., Yamkhin, J., and Zou, D. (2019). Northern Hemisphere permafrost map based on TTOP modelling for 2000–2016 at 1 km² scale. *Earth-Science Reviews*, 193, 299–316. <https://doi.org/10.1016/j.earscirev.2019.04.023>
- Oerlemans, J. (2001). *Glaciers and climate change*. A.A. Balkema Publishers.
- Onaca, A., Ardelean, F., Urdea, P., and Magori, B. (2017). Southern Carpathian rock glaciers: Inventory, distribution and environmental controlling factors. *Geomorphology*, 293, 391–404. <https://doi.org/10.1016/j.geomorph.2016.03.032>
- Outcalt, S. I., and Benedict, J. B. (1965). Photo-Interpretation of two Types of Rock Glacier in the Colorado Front Range, U.S.A. *Journal of Glaciology*, 5(42), 849–856. <https://doi.org/10.3189/s0022143000018918>
- Pandey, P. (2019). Inventory of rock glaciers in Himachal Himalaya, India using high-resolution Google Earth imagery. *Geomorphology*, 340, 103–115. <https://doi.org/https://doi.org/10.1016/j.geomorph.2019.05.001>
- Peel, M. C., Finlayson, B. L., and McMahon, T. A. (2007). Updated world map of the Köppen-Geiger climate classification. *Hydrol. Earth Syst. Sci.*, 11(5), 1633–1644. <https://doi.org/10.5194/hess-11-1633-2007>
- Pepin, N. (2000). Twentieth-century change in the climate record for the Front Range, Colorado, USA. *Arctic, Antarctic, and Alpine Research*, 32(2), 135–146.
- PERMOS. (2019). *Permafrost in Switzerland 2014/2015 to 2017/2018* (Glaciological Report (Permafrost) Issue).
- PERMOS. (2021). *Swiss Permafrost Bulletin 2019/2020*.
- Perruchoud, E., and Delaloye, R. (2007). Short-term changes in surface velocities on the Becs-de-Bosson rock glacier (western Swiss Alps). Proceedings of the 9th International Symposium on High Mountain Remote Sensing Cartography, Graz.
- Pillewizer, W. (1938). Photogrammetrische Gletscheruntersuchungen im Sommer 1938. *Zeitschrift der Gesellschaft für Erdkunde*, 9, 367–372.
- Potter, J. N., Steig, E., Clark, D., Speece, M., Clark, G. t., and Updike, A. B. (1998). Galena Creek rock glacier revisited—New observations on an old controversy. *Geografiska Annaler: Series A, Physical Geography*, 80(3–4), 251–265.
- Potter, J. N. (1972). Ice-Cored Rock Glacier, Galena Creek, Northern Absaroka Mountains, Wyoming. *GSA Bulletin*, 83(10), 3025–3058. [https://doi.org/10.1130/0016-7606\(1972\)83\[3025:IROGGA\]2.0.CO;2](https://doi.org/10.1130/0016-7606(1972)83[3025:IROGGA]2.0.CO;2)
- Quincey, D. J., Glasser, N. F., Cook, S. J., and Luckman, A. (2015). Heterogeneity in Karakoram glacier surges. *Journal of Geophysical Research: Earth Surface*, 120(7), 1288–1300. <https://doi.org/https://doi.org/10.1002/2015JF003515>

BIBLIOGRAPHY

- Rabatel, A., Castebrunet, H., Favier, V., Nicholson, L., and Kinnard, C. (2011). Glacier changes in the Pascua-Lama region, Chilean Andes (29° S): recent mass balance and 50 yr surface area variations. *The Cryosphere*, 5(4), 1029-1041. <https://doi.org/10.5194/tc-5-1029-2011>
- Ran, Z. Z., and Liu, G. N. (2018). Rock glaciers in Daxue Shan, south-eastern Tibetan Plateau: an inventory, their distribution, and their environmental controls. *The Cryosphere*, 12(7), 2327-2340. <https://doi.org/10.5194/tc-12-2327-2018>
- Rangecroft, S., Harrison, S., Anderson, K., Magrath, J., Castel, A. P., and Pacheco, P. (2014). A first rock glacier inventory for the Bolivian Andes. *Permafrost and Periglacial Processes*, 25(4), 333-343. <https://doi.org/https://doi.org/10.1002/ppp.1816>
- Reinosch, E., Gerke, M., Riedel, B., Schwalb, A., Ye, Q., and Buckel, J. (2021). Rock glacier inventory of the western Nyainq êntanglha Range, Tibetan Plateau, supported by InSAR time series and automated classification. *Permafrost and Periglacial Processes*. <https://doi.org/10.1002/ppp.2117>
- Reznichenko, N., Davies, T., Shulmeister, J., and McSaveney, M. (2010). Effects of debris on ice-surface melting rates: an experimental study. *Journal of Glaciology*, 56(197), 384-394. <https://doi.org/https://doi.org/10.3189/002214310792447725>
- Rignot, E., Hallet, B., and Fountain, A. (2002). Rock glacier surface motion in Beacon Valley, Antarctica, from synthetic-aperture radar interferometry. *Geophysical Research Letters*, 29(12), 48-41-48-44. <https://doi.org/https://doi.org/10.1029/2001GL013494>
- Robson, B. A., Bolch, T., MacDonell, S., Höbling, D., Rastner, P., and Schaffer, N. (2020). Automated detection of rock glaciers using deep learning and object-based image analysis. *Remote Sensing of Environment*, 250. <https://doi.org/10.1016/j.rse.2020.112033>
- Rodriguez, E., and Martin, J. M. (1992). Theory and design of Interferometric Synthetic Aperture Radars. *Iee Proceedings-F Radar and Signal Processing*, 139(2), 147-159. <https://doi.org/https://doi.org/10.1049/ip-f.2.1992.0018>
- Roer, I., Haeberli, W., Avian, M., Kaufmann, V., Delaloye, R., Lambiel, C., and Kaab, A. (2008). *Observations and considerations on destabilizing active rockglaciers in the European Alps* Proceedings of the 9th International Conference on Permafrost, Fairbanks, Alaska.
- Roer, I., Käb, A., and Dikau, R. (2005). Rockglacier acceleration in the Turtmann valley (Swiss Alps): Probable controls. *Norsk Geografisk Tidsskrift - Norwegian Journal of Geography*, 59(2), 157-163. <https://doi.org/10.1080/00291950510020655>
- Roer, I., and Nyenhuys, M. (2007). Rockglacier activity studies on a regional scale: comparison of geomorphological mapping and photogrammetric monitoring. *Earth Surface Processes and Landforms*, 32(12), 1747-1758. <https://doi.org/https://doi.org/10.1002/esp.1496>
- Rott, H., and Siegel, A. (1999, 28 June-2 July 1999). Analysis of mass movements in alpine terrain by means of SAR interferometry. IEEE 1999 International Geoscience and Remote Sensing Symposium. IGARSS'99 (Cat. No.99CH36293),
- Rouyet, L., Lauknes, T. R., Christiansen, H. H., Strand, S. M., and Larsen, Y. (2019). Seasonal dynamics of a permafrost landscape, Adventdalen, Svalbard, investigated by InSAR. *Remote Sensing of Environment*, 231. <https://doi.org/10.1016/j.rse.2019.111236>
- Salerno, F., Guyennon, N., Thakuri, S., Viviano, G., Romano, E., Vuillermoz, E., Cristofanelli, P., Stocchi, P., Agrillo, G., Ma, Y., and Tartari, G. (2015). Weak precipitation, warm winters and springs impact glaciers of south slopes of Mt. Everest (central Himalaya) in the last 2 decades (1994–2013). *The Cryosphere*, 9(3), 1229-1247. <https://doi.org/https://doi.org/10.5194/tc-9-1229-2015>

BIBLIOGRAPHY

- Scapozza, C., Lambiel, C., Bozzini, C., Mari, S., and Conedera, M. (2014). Assessing the rock glacier kinematics on three different timescales: a case study from the southern Swiss Alps. *Earth Surface Processes and Landforms*, 39(15), 2056-2069. <https://doi.org/https://doi.org/10.1002/esp.3599>
- Schaffer, N., MacDonell, S., Reveillet, M., Yanez, E., and Valois, R. (2019). Rock glaciers as a water resource in a changing climate in the semiarid Chilean Andes. *Regional Environmental Change*, 19(5), 1263-1279. <https://doi.org/10.1007/s10113-018-01459-3>
- Schmid, M. O., Baral, P., Gruber, S., Shahi, S., Shrestha, T., Stumm, D., and Wester, P. (2015). Assessment of permafrost distribution maps in the Hindu Kush Himalayan region using rock glaciers mapped in Google Earth. *The Cryosphere*, 9(6), 2089-2099. <https://doi.org/10.5194/tc-9-2089-2015>
- Scott, W. J., Sellmann, P. V., and Hunter, J. A. (1990). Geophysics in the study of permafrost. In *Geotechnical and Environmental Geophysics: Volume I, Review and Tutorial* (pp. 355-384). <https://doi.org/https://doi.org/10.1190/1.9781560802785.ch13>
- Scotti, R., Brardinoni, F., Alberti, S., Frattini, P., and Crosta, G. B. (2013). A regional inventory of rock glaciers and protalus ramparts in the central Italian Alps. *Geomorphology*, 186, 136-149. <https://doi.org/https://doi.org/10.1016/j.geomorph.2012.12.028>
- Scotti, R., Crosta, G. B., and Villa, A. (2017). Destabilisation of Creeping Permafrost: The Plator Rock Glacier Case Study (Central Italian Alps). *Permafrost and Periglacial Processes*, 28(1), 224-236. <https://doi.org/https://doi.org/10.1002/ppp.1917>
- Shi, Y. (2006). *The quaternary glaciations and environmental variations in China* (1 ed.). Hebei Science & Technology Press.
- Shroder, J. F. (1978). Dendrogeomorphological Analysis of Mass Movement on Table Cliffs Plateau, Utah. *Quaternary Research*, 9(2), 168-185. [https://doi.org/10.1016/0033-5894\(78\)90065-0](https://doi.org/10.1016/0033-5894(78)90065-0)
- Sorg, A., Kaab, A., Roesch, A., Bigler, C., and Stoffel, M. (2015). Contrasting responses of Central Asian rock glaciers to global warming. *Scientific Reports*, 5, 8228. <https://doi.org/10.1038/srep08228>
- Spencer, A. (1900). A peculiar form of talus. *Science*, 11(266), 188.
- Steig, E. J., Fitzpatrick, J. J., Potter, J. N., and Clark, D. H. (1998). The geochemical record in rock glaciers. *Geografiska Annaler: Series A, Physical Geography*, 80(3-4), 277-286. <https://doi.org/https://doi.org/10.1111/j.0435-3676.1998.00043.x>
- Strozzi, T., Caduff, R., Jones, N., Barboux, C., Delaloye, R., Bodin, X., Käb, A., Mätzler, E., and Schrott, L. (2020). Monitoring Rock Glacier Kinematics with Satellite Synthetic Aperture Radar. *Remote Sensing*, 12(3), 559. <https://www.mdpi.com/2072-4292/12/3/559>
- Strozzi, T., Raetzo, H., Wegmüller, U., Papke, J., Caduff, R., Werner, C., and Wiesmann, A. (2015). Satellite and Terrestrial Radar Interferometry for the Measurement of Slope Deformation. In G. Lollino, A. Manconi, F. Guzzetti, M. Culshaw, P. Bobrowsky, and F. Luino, *Engineering Geology for Society and Territory - Volume 5* Cham.
- Tian, L., Zhao, L., Wu, X., Fang, H., Zhao, Y., Yue, G., Liu, G., and Chen, H. (2017). Vertical patterns and controls of soil nutrients in alpine grassland: Implications for nutrient uptake. *Sci Total Environ*, 607-608, 855-864. <https://doi.org/10.1016/j.scitotenv.2017.07.080>
- Ting, J. M., Torrence Martin, R., and Ladd, C. C. (1983). Mechanisms of strength for frozen sand. *Journal of Geotechnical Engineering*, 109(10), 1286-1302.
- Villarroel, C. D., Tamburini Beliveau, G., Forte, A. P., Monserrat, O., and Morville, M. (2018). DInSAR for a Regional Inventory of Active Rock Glaciers in the Dry Andes Mountains of

BIBLIOGRAPHY

- Argentina and Chile with Sentinel-1 Data. *Remote Sensing*, 10(10). <https://doi.org/10.3390/rs10101588>
- Vivero, S., and Lambiel, C. (2019). Monitoring the crisis of a rock glacier with repeated UAV surveys. *Geogr. Helv.*, 74(1), 59-69. <https://doi.org/10.5194/gh-74-59-2019>
- Vivian, R., and Bocquet, G. (1973). Subglacial cavitation phenomena under the glacier D'Argentière, Mont Blanc, France. *Journal of Glaciology*, 12(66), 439-451. <https://doi.org/https://doi.org/10.3189/S0022143000031853>
- Wagner, S. (1992). Creep of Alpine Permafrost, Investigated on the Murtel Rock Glacier. In *Permafrost and Periglacial Processes, Vol 3, No 2, Apr-Jun 1992: Permafrost and Periglacial Environments in Mountain Areas* (pp. 157-162).
- Wahrhaftig, C., and Cox, A. (1959). Rock glaciers in the Alaska Range. *GSA Bulletin*, 70(4), 383-436. [https://doi.org/10.1130/0016-7606\(1959\)70\[383:Rgitar\]2.0.Co;2](https://doi.org/10.1130/0016-7606(1959)70[383:Rgitar]2.0.Co;2)
- Wang, X. W., Liu, L., Zhao, L., Wu, T. H., Li, Z. Q., and Liu, G. X. (2017). Mapping and inventorying active rock glaciers in the northern Tien Shan of China using satellite SAR interferometry. *Cryosphere*, 11(2), 997-1014. <https://doi.org/10.5194/tc-11-997-2017>
- Wang, Y., Hou, S., Huai, B., An, W., Pang, H., and Liu, Y. (2018). Glacier anomaly over the western Kunlun Mountains, Northwestern Tibetan Plateau, since the 1970s. *Journal of Glaciology*, 64(246), 624-636.
- Whalley, W. B., and Azizi, F. (1994). Rheological models of active rock glaciers - evaluation, critique and a possible test. *Permafrost and Periglacial Processes*, 5(1), 37-51. <https://doi.org/https://doi.org/10.1002/ppp.3430050105>
- Whalley, W. B., and Azizi, F. (2003). Rock glaciers and protalus landforms: Analogous forms and ice sources on Earth and Mars. *Journal of Geophysical Research: Planets*, 108(E4). <https://doi.org/https://doi.org/10.1029/2002JE001864>
- White, S. E. (1971). Rock Glacier Studies in the Colorado Front Range, 1961 to 1968. *Arctic and Alpine Research*, 3(1), 43-64. <https://doi.org/10.2307/1550382>
- White, S. E. (1976). Rock Glaciers and Block fields, Review and new data. *Quaternary Research*, 6(1), 77-97. [https://doi.org/10.1016/0033-5894\(76\)90041-7](https://doi.org/10.1016/0033-5894(76)90041-7)
- Williams, P. J. (1991). *The frozen earth : fundamentals of geocryology* (1st paperback ed ed.). Cambridge University Press.
- Wirz, V., Beutel, J., Gruber, S., Gubler, S., and Purves, R. S. (2014). Estimating velocity from noisy GPS data for investigating the temporal variability of slope movements. *Natural Hazards and Earth System Sciences*, 14(9), 2503-2520. <https://doi.org/10.5194/nhess-14-2503-2014>
- Wirz, V., Geertsema, M., Gruber, S., and Purves, R. S. (2016a). Temporal variability of diverse mountain permafrost slope movements derived from multi-year daily GPS data, Matteringal, Switzerland. *Landslides*, 13(1), 67-83. <https://doi.org/10.1007/s10346-014-0544-3>
- Wirz, V., Gruber, S., Purves, R. S., Beutel, J., Gartner-Roer, I., Gubler, S., and Vieli, A. (2016b). Short-term velocity variations at three rock glaciers and their relationship with meteorological conditions. *Earth Surface Dynamics*, 4(1), 103-123. <https://doi.org/10.5194/esurf-4-103-2016>
- Woodhouse, I. H. (2006). *Introduction to microwave remote sensing*. CRC/Taylor&Francis.
- Wu, Y. Q., Cui, Z. J., Liu, G. N., Ge, D. K., Yin, J. R., Xu, Q. H., and Pang, Q. Q. (2001). Quaternary geomorphological evolution of the Kunlun Pass area and uplift of the Qinghai-Xizang (Tibet) Plateau. *Geomorphology*, 36(3-4), 203-216. [https://doi.org/10.1016/S0169-555X\(00\)00057-X](https://doi.org/10.1016/S0169-555X(00)00057-X)

BIBLIOGRAPHY

- Yang, M., Nelson, F. E., Shiklomanov, N. I., Guo, D., and Wan, G. (2010). Permafrost degradation and its environmental effects on the Tibetan Plateau: A review of recent research. *Earth-Science Reviews*, 103(1-2), 31-44. <https://doi.org/10.1016/j.earscirev.2010.07.002>
- Yang, M., Wang, X., Pang, G., Wan, G., and Liu, Z. (2019). The Tibetan Plateau cryosphere: Observations and model simulations for current status and recent changes. *Earth-Science Reviews*, 190, 353-369. <https://doi.org/10.1016/j.earscirev.2018.12.018>
- Yang, M., Yao, T., Gou, X., Hirose, N., and Fujii, H. (2007). Diurnal freeze/thaw cycles of the ground surface on the Tibetan Plateau. *Chinese Science Bulletin*, 52, 136-139. <https://doi.org/https://doi.org/10.1007/s11434-007-0004-8>
- Yao, T., Xue, Y., Chen, D., Chen, F., Thompson, L., Cui, P., Koike, T., Lau, W. K. M., Lettenmaier, D., Mosbrugger, V., Zhang, R., Xu, B., Dozier, J., Gillespie, T., Gu, Y., Kang, S., Piao, S., Sugimoto, S., Ueno, K., Wang, L., Wang, W., Zhang, F., Sheng, Y., Guo, W., Ailikun, Yang, X., Ma, Y., Shen, S. S. P., Su, Z., Chen, F., Liang, S., Liu, Y., Singh, V. P., Yang, K., Yang, D., Zhao, X., Qian, Y., Zhang, Y., and Li, Q. (2019). Recent Third Pole's Rapid Warming Accompanies Cryospheric Melt and Water Cycle Intensification and Interactions between Monsoon and Environment: Multidisciplinary Approach with Observations, Modeling, and Analysis. *Bulletin of the American Meteorological Society*, 100(3), 423-444. <https://doi.org/10.1175/bams-d-17-0057.1>
- Yasuda, T., and Furuya, M. (2015). Dynamics of surge-type glaciers in West Kunlun Shan, Northwestern Tibet. *Journal of Geophysical Research: Earth Surface*, 120(11), 2393-2405. <https://doi.org/https://doi.org/10.1002/2015JF003511>
- Yu, C., Li, Z. H., and Penna, N. T. (2018a). Interferometric synthetic aperture radar atmospheric correction using a GPS-based iterative tropospheric decomposition model. *Remote Sensing of Environment*, 204, 109-121. <https://doi.org/10.1016/j.rse.2017.10.038>
- Yu, C., Li, Z. H., Penna, N. T., and Crippa, P. (2018b). Generic Atmospheric Correction Model for Interferometric Synthetic Aperture Radar Observations. *Journal of Geophysical Research-Solid Earth*, 123(10), 9202-9222. <https://doi.org/10.1029/2017JB015305>
- Yu, C., Penna, N. T., and Li, Z. H. (2017). Generation of real-time mode high-resolution water vapor fields from GPS observations. *Journal of Geophysical Research-Atmospheres*, 122(3), 2008-2025. <https://doi.org/10.1002/2016JD025753>
- Zhang, E., Liu, L., Huang, L., and Ng, K. S. (2021). An automated, generalized, deep-learning-based method for delineating the calving fronts of Greenland glaciers from multi-sensor remote sensing imagery. *Remote Sensing of Environment*, 254, 112265. <https://doi.org/https://doi.org/10.1016/j.rse.2020.112265>
- Zhang, G., Yao, T., Xie, H., Yang, K., Zhu, L., Shum, C. K., Bolch, T., Yi, S., Allen, S., Jiang, L., Chen, W., and Ke, C. (2020). Response of Tibetan Plateau lakes to climate change: Trends, patterns, and mechanisms. *Earth-Science Reviews*, 208. <https://doi.org/10.1016/j.earscirev.2020.103269>
- Zhao, L., Hu, G., Zou, D., Wu, X., Ma, L., Sun, Z., Yuan, L., Zhou, H., and Liu, S. (2019). Permafrost changes and its effects on hydrological processes on Qinghai-Tibet Plateau. *Bulletin of Chinese Academy of Sciences*, 34(11), 1233-1246. <https://doi.org/10.16418/j.issn.1000-3045.2019.11.006>
- Zhao, L., and Sheng, Y. (2015). *Permafrost survey manual*. Science Press.
- Zhao, L., and Sheng, Y. (2019). *Permafrost in the Qinghai-Tibet plateau and its changes*. Science Press.
- Zhou, Y., Li, Z., Li, J., Zhao, R., and Ding, X. (2018). Glacier mass balance in the Qinghai-Tibet Plateau and its surroundings from the mid-1970s to 2000 based on Hexagon KH-9 and SRTM DEMs. *Remote Sensing of Environment*, 210, 96-112.

BIBLIOGRAPHY

- Zhu, C. (1989). The characteristics of the surface movement of the lobate-shape rock glacier from the debris fabric, Tianshan, China. *Journal of Glaciology and Geocryology*, 1, 82-88.
- Zhu, C., Cui, Z., and Yao, Z. (1992). Research on the features of rock glaciers on the central Tianshan Mountains. *Acta Geographica Sinica*, 47(3), 233-241.
- Zou, D., Zhao, L., Sheng, Y., Chen, J., Hu, G., Wu, T., Wu, J., Xie, C., Wu, X., Pang, Q., Wang, W., Du, E., Li, W., Liu, G., Li, J., Qin, Y., Qiao, Y., Wang, Z., Shi, J., and Cheng, G. (2017). A new map of permafrost distribution on the Tibetan Plateau. *The Cryosphere*, 11(6), 2527-2542.
<https://doi.org/10.5194/tc-11-2527-2017>